# Couette Flows of Granular Materials: Mixing, Rheology, and Energy Dissipation

Thesis by
Anna Karion

In Partial Fulfillment of the Requirements
for the Degree of
Doctor of Philosophy


California Institute of Technology
Pasadena, California

2000

(Submitted July 16, 1999)

# Acknowledgements

I am grateful to the Hitachi Research Laboratories and the National Science Foundation for funding this research. I would like to thank my advisor, Professor Melany Hunt, for her guidance throughout this project. Professor Christopher Brennen also provided invaluable advice during my graduate career. I am also grateful for the advice and support of the other members of my committee: Charlie Campbell, Ron Scott, and Tom Heaton.

Rodney Rojas deserves special thanks for building the experimental apparatus, as does John Van Deusen for his help in the M.E. shop. I also owe thanks to the undergraduates that helped me with my research, Benson Muite and Susan Sher. I would also like to thank the members of my research group, Carl Wassgren, Douglas Varela, Roberto Zenit, and Gustavo Joseph for their friendship, ideas, and many discussions. My friends in the department, Tricia and Sudipto Sur, Bob Uy, Clancy Rowley, Jeff Eldredge, and Martha Gallivan, also helped me with their technical assistance and made life in the Thomas basement enjoyable. I would also like to thank the members of Bananafish: Mark Stopfer, Kate Macleod, and Greg Carbone, for their friendship and for making my graduate career fun as well as educational.

Finally, I would like to thank my family. My parents, my sister Katherine, and my brother-in-law David have given me their love and support. Lastly, I want to thank Paul Ohm, who has given me love, support, advice, and a lot of encouragement during my entire graduate career, from orientation day through to my thesis defense.

# Abstract

This thesis examines the behavior of a granular material sheared in a gap between two moving boundaries. In fluid mechanics, this type of flow is known as a Couette flow. Two different kinds of granular Couette flows were studied. First, gravity-free flow between two infinite plates moving in opposite directions was investigated using computer simulations. Second, flow between a stationary outer cylinder and an inner rotating cylinder was studied using both experiments and computer simulations.

Two-dimensional discrete element computer simulations of infinite planar Couette flows were used to study the rheology, energy dissipation, and other flow properties in flows of particles of uniform size for three different gap widths. The energy dissipation rate was measured and a thermal analysis was conducted to determine the thermodynamic temperature rise and heat flux of such flows. Given a constant wall velocity, all of the properties in flows of identical particles were found to depend on the value of the solid fraction at the walls, which in turn depended on both the average solid fraction and the gap width. When the average solid fraction reached a critical threshold, the amount of work done on the flow drastically increased, increasing the average strain rate, granular temperature, wall stresses, and energy dissipation in the flow. This solid fraction threshold occurred after the center region of the flow had reached a dense limit and any further increase in solid fraction necessarily occurred in the wall regions. Various results from computer simulations were found to compare reasonably well with past results derived using kinetic theory.

Mixing and other flow properties were also investigated in planar Couette flows of two different particle sizes, as functions of the size ratio and solid fraction ratio of the two species. Larger particles were found to migrate away from the regions of high fluctuation energy near the two moving boundaries in all cases. Mixture flows were found to behave very similarly to flows of mono-sized particles at high ratios of the solid fraction of small to large particles. As the solid fraction ratio decreased and the number of large particles increased, results deviated from the corresponding flow of

identical particles. Flows with large size ratios of large to small particles deviated the most from the result of mono-sized particles, because stresses and energy dissipation rates are both mass-dependent.

The second type of Couette flow, between two concentric cylinders, was investigated in a horizontal orientation (with the axis of rotation perpendicular to the direction of gravity) and in a vertical orientation (with the axis parallel to the direction of gravity), using both experiments and computer simulations. In the horizontal geometry, high-speed imaging was used to calculate experimental mean and fluctuation velocity profiles that were compared to results from three-dimensional discrete element simulations. Segregation of binary particle mixtures was also investigated in this geometry. Segregation in this flow was driven by a percolation mechanism acting at the free surface, causing large particles to migrate to the top. Computer simulations compared well qualitatively with experiments, successfully predicting the velocity profiles and the segregation pattern at the surface. When compared quantitatively, however, fluctuation velocities in the simulations were considerably greater than those found in the experiment, and the radial segregation observed in experiments did not occur to the same extent in simulations.

The vertically-oriented cylindrical Couette flow experiment was used to measure the shear stress on the outer cylinder wall as a function of different variables. The shear stress was found to be independent of the inner cylinder rotation rate, because the material was unconfined and allowed to dilate. The measured stress showed a linear dependence on the height of material in the apparatus, indicating a hydrostatic variation of the normal stress. The shear stress also varied significantly with the ratio of the gap width to the particle diameter.

# Contents

# List of Figures

# List of Tables

# Nomenclature

| Symbol | Description |
|---|---|
| $Ba$ | Bagnold number |
| $\beta$ | Particle roughness coefficient |
| $d$ | Particle diameter |
| $\Delta$ | Amount two surfaces overlap during a collision |
| $\Delta E$ | Loss of energy during a collision |
| $\Delta t$ | Timestep of simulation |
| $e_p$ | Coefficient of restitution in particle-particle collisions |
| $e_w$ | Coefficient of restitution in particle-wall collisions |
| $\gamma$ | Energy dissipated per unit area per unit time in a two-dimensional flow, or per unit volume per unit time in a three-dimensional flow |
| $\Gamma_w$ | Energy dissipated per unit time at the solid boundaries of the flow |
| $h$ | Distance between bounding walls |
| $I$ | Moment of inertia of a particle |
| $K$ | Normal stress ratio $\tau_{rr}/\tau_{zz}$ |
| $k_g$ | Thermal conductivity of gas phase |
| $k_{kt}$ | Streaming, or kinetic thermal conductivity |
| $k_{mc}$ | Molecular effective thermal conductivity |
| $k_n$ | Spring constant used in normal contact model of simulations |

| | |
|---|---|
| $k_p$ | Particle thermal conductivity |
| $k_s$ | Spring constant used in tangential contact model of simulations |
| $k_{tot}$ | Total effective thermal conductivity |
| $L$ | Height of beads in experimental apparatus |
| $m$ | Particle mass |
| $\mu_p$ | Coefficient of friction between particles |
| $\mu_w$ | Coefficient of friction for particle-wall collisions |
| $N$ | A normalized factor relating to the number density of particles |
| $n(\theta)$ | Collision angle distribution function |
| $\nu$ | Solid fraction of particles: ratio of particle volume (or area) to total volume (or area) |
| $\nu_n$ | Damping coefficient used in normal contact model of simulations |
| $\Omega$ | Angular velocity of inner cylinder in cylindrical Couette flows |
| $\omega$ | Particle angular velocity |
| $Pe$ | Peclet number |
| $\phi$ | Diameter ratio of large to small particles in binary mixtures |
| $q_i$ | Net electrostatic charge on particle $i$ |
| $q_h$ | Heat flux |
| $r$ | Particle radius |
| $R$ | Solid fraction ratio of small to large particles in binary mixtures, $\nu_{small}/\nu_{large}$ |
| $R$ | Radial coordinate in cylindrical Couette flows |
| $\rho_p$ | Particle density |
| $R_{inner}$ | Radius of inner cylinder in cylindrical Couette flows |
| $R_{outer}$ | Radius of outer cylinder in cylindrical Couette flows |
| $t$ | Time |
| $\mathcal{T}$ | Dimensional thermodynamic temperature (K) |

| | |
|---|---|
| $\tau$ | Duration of a collision |
| $\tau_{rr}$ | Normal stress on bounding wall, in cylindrical flows |
| $\tau_{r\theta}$ | Shear stress on bounding wall, in cylindrical flows |
| $\tau_{xy}$ | Shear stress on bounding wall, in planar flows |
| $\tau_{yy}$ | Normal stress on bounding wall, in planar flows |
| $\tau_{zz}$ | Normal stress in cylindrical flows |
| $\theta$ | Collision angle |
| $\Theta$ | Non-dimensional thermodynamic temperature |
| $\theta$ | The angular coordinate, in cylindrical Couette flows |
| $T_r$ | Rotational component of granular temperature |
| $T_t$ | Translational component of granular temperature |
| $U$ | Relative velocity of boundaries |
| $u$ | Particle velocity in direction of flow, in planar flows |
| $u_w$ | Average velocity of particles one small particle radius away from the boundary |
| $v$ | Particle velocity in direction perpendicular to main flow, in planar flows |
| $v_r$ | Particle velocity in the $R$, or transverse direction, in cylindrical Couette flows |
| $v_\theta$ | Particle velocity in the $\theta$, or flow direction, in cylindrical Couette flows |
| $v_{wall}$ | Velocity of inner cylinder surface in cylindrical Couette flows |
| $w$ | Width of simulation domain |
| $W$ | Work done per unit time by the boundaries in a shear flow |

# Chapter 1

# Introduction

## 1.1 Motivation

A granular material is a collection of many discrete solid particles. Granular materials interest researchers because of their dual nature. Depending on the situation, a granular material may behave as a fluid (taking the shape of its container) or a solid (resisting shearing stresses as in a sandpile). In a granular flow, momentum and energy transfer occur primarily through inter-particle collisions, and the effect of any interstitial fluid is secondary in influence.

Examples of granular flows are commonly found in both nature and industry. In nature, landslides, soil liquefaction, formation of planetary rings, erosion, river sedimentation, ice flow, and sand dune formation are such examples. In industry, granular flows can be found in the mixing and transport of pharmaceutical powders and pellets, foodstuffs, detergents, coal, and other mining products. It has been estimated that in the chemical industry, one half of the products and at least three quarters of the raw materials are in granular form [Nedderman, 1992]. Because granular materials are used so often in industrial processes, there is great incentive to improve their handling to increase efficiency and decrease cost by an understanding of the mechanics of granular media. However, most industries use empiricism and past experience to guide their use of granular materials.

Most applications of granular material flows involve shearing the material. The granular materials in landslides, conveyors, chutes, hoppers, and mixers are all shearing in some manner. Thus, from a practical point of view, the investigation of shear flows is desirable.

All granular flows are naturally highly dissipative. Frictional and inelastic collisions between grains dissipate energy at a high rate that can lead to undesirably high temperatures in temperature-sensitive materials such as foodstuffs, medicines, or toner used in laser printers. The energy supplied to a granular flow, through vibration, gravity, or shearing is rapidly dissipated into heat. Thus, work must constantly be done on the system to maintain a granular flow. Measuring the shear stress at the moving boundary of a shear flow yields information about the energy requirements of the flow. The investigation of both energy dissipation and shear stresses helps the understanding of many industrial applications and processes.

In addition to the investigation of energy dissipation and shear stresses, mixing in flows of particles of two different sizes is also studied in this work. Industrial processes rarely utilize particles that are perfectly uniform in size. Often they may involve mixtures of particles of different sizes, shapes and densities. Segregation of the different components of a particle mixture is commonly observed in such applications. For this reason, segregation is an important and popular area of research within the field of granular flow.

The present research investigates two kinds of shear flows: planar Couette flows with no gravity, and cylindrical Couette flows with gravity. The first, a Couette flow between two infinite plates, is the most simple bounded shear flow, making it a popular area of study [Campbell, 1993; Campbell and Brennen, 1985; Kim, 1995; Rosato and Kim, 1994; Savage and Dai, 1993]. The second flow investigated, a cylindrical Couette flow under gravity, is industrially more relevant and realistic, although significantly more complex.

## 1.2 Background

Granular materials have been the subject of scientific research for over a century. Reynolds studied granular shear flows in 1885, discovering that a packed bed of particles must dilate to undergo shear because the individual layers of particles must have the room to pass over each other [Reynolds, 1885]. This phenomenon is now known as Reynolds's Principle of Dilatancy. Bagnold [1954] conducted one of the first modern studies in granular flow, an experiment on a suspension of neutrally buoyant solid spheres in a Newtonian fluid (water and a glycerine-water-alcohol mixture) in a Couette device. The suspension was placed between an outer rotating vertical cylinder and an inner stationary cylinder, and the normal and shear stresses were measured at the walls. Bagnold first characterized three regimes of suspension flows, quantified by what is now known as the Bagnold number:

$$Ba = \frac{\rho_p d^2 \lambda^{1/2} (du/dy)}{\mu}. \tag{1.1}$$

In this expression, $\rho_p$ is the granular material density, $d$ is the particle diameter, $\mu$ is the interstitial fluid viscosity, $\lambda$ is the linear concentration, and $(du/dy)$ is the velocity gradient. The linear concentration, $\lambda$, is defined as the ratio of the particle diameter to the mean free dispersion distance. The velocity gradient, or strain rate, is proportional to the rotation rate of the outer cylinder. At low Bagnold numbers ($Ba < 40$), the suspension was in the slow-shearing, macro-viscous regime in which the interstitial fluid played a large role in the dynamics. At very high Bagnold numbers ($Ba > 450$) the suspension was in a grain-inertia, or rapid flow regime, where the stress $\tau$ on the walls had no dependence on fluid properties:

$$\tau \propto \rho_p (\lambda d)^2 \left(\frac{du}{dy}\right)^2. \tag{1.2}$$

This quadratic dependence on the rate of strain is different from the behavior of a Newtonian fluid, in which the shear stress is linearly proportional to the strain rate. Furthermore, Bagnold found that in the rapid regime, the shear stresses were proportional to the normal stresses. At intermediate Bagnold numbers, the suspension was in a transitional regime between the two extremes.

Dry granular flows can also be classified into three basic regimes [Campbell, 1990; Savage, 1984]. A quasi-static regime describes granular flow with low rates of deformation, characterized by long-lasting frictional contacts between particles. Soil mechanics theories based on plasticity models have been used to describe granular behavior in this regime. At the other extreme, a rapid granular flow is analogous to Bagnold's grain-inertia regime, in which particle collisions are instantaneous and the mean free path between collisions is large. Most industrial and natural granular flows exist in a third, transitional regime between these two extremes, however.

Theory intended to describe granular flows in the rapid regime has been developed using ideas from the kinetic theory of dense gases. Ogawa [1978] first introduced the analogy between particles in a granular material flow and individual molecules making up a dense gas. Along with this analogy came the concept of a granular temperature. Just as the thermodynamic temperature plays an important role in dense gas kinetic theory, the granular temperature is a crucial variable in theories of granular materials derived from kinetic theory. The granular temperature is the specific fluctuation kinetic energy of the flow, usually defined as the average of the fluctuation velocities:

$$T = \frac{1}{3} \left\langle u'u' + v'v' + w'w' \right\rangle , \tag{1.3}$$

where $u' = u - \langle u \rangle$, and $u$, $v$, and $w$ are the particle velocities in the three principal directions. Brackets denote an ensemble average.

Jenkins and Savage [1983] first introduced constitutive relations for granular materials based on dense gas kinetic theory. Much of the theory for rapid granular flows has since been developed on the basis of that work. Lun et al. [1984] derived consti-

tutive laws for smooth spherical particles. Jenkins and Richman [1985] proposed a theory for rough, inelastic disks and spheres. Rough spherical particles have also been treated by Lun and Savage [1987] and Lun [1991]. Flows of binary mixtures have been studied through kinetic theory approaches as well. Jenkins and Mancini developed balance laws and constitutive relations for binary mixtures of slightly inelastic smooth disks [1987] and spheres [1989], while Farrell et al. [1986] developed kinetic theory for binary mixtures of smooth, inelastic spheres. The boundaries of rapid granular flows have also been investigated utilizing kinetic theory. Jenkins and Richman [1986], Richman and Chou [1988], and Richman [1988] have considered boundary conditions for smooth disks against a "bumpy" boundary formed by attaching halves of disks along a wall. Jenkins [1992] and Jenkins and Louge [1997] developed boundary conditions for a flat, frictional wall in three dimensions. Hanes et al. [1988] apply previous theories to the flow of identical disks driven by bumpy boundaries in the dense limit.

Because these granular flow theories are derived from the kinetic theory of gases, several limiting assumptions are made: particles are round, collisions between them are instantaneous and binary, the coefficient of restitution is constant, and the random motion of particles is independently distributed [Campbell, 1990]. Computer simulations provide a valuable tool because one can match these ideal assumptions for theory validation as well as attempt to model more realistic flows to which the theory cannot be applied. Although several types of computer simulations have been used to study granular materials in the past (such as Monte Carlo methods), the most popular types of simulations are discrete element simulations. These simulations are derived from molecular dynamics simulations, and are deterministic, rather than statistical. Discrete element simulations model each individual particle in a flow and track its trajectory over time. Different forces on the particles can be modeled (such as fluid drag, electrostatic forces, and gravity) as well as different particle sizes and shapes. Cundall and Strack [1979] first developed this method for studying geophysical applications.

Discrete element simulations have been used in the past to investigate many types and geometries of granular flows [Campbell, 1982; Drake and Walton, 1995; Wassgren, 1997]. In the area of shear flows, both simple shear flows and bounded flows between infinite plates have been investigated using simulations. A simple shear flow is an infinite shear flow simulated through the use of periodic boundaries in all three directions and the imposition of a constant velocity gradient in one direction. A periodic boundary allows a particle to cross the boundary and reappear at the opposite boundary with the same velocity and position. Many researchers have used discrete element methods to study two- and three-dimensional simple shear flows of particles, including Campbell [1986; 1989], Campbell and Gong [1986], Lun and Bent [1994], and Walton and Braun [1986a; 1986b]. Couette flows of particles sheared between two infinite plates with various boundary conditions have been studied using the discrete element method as well [Campbell, 1993; Campbell and Brennen, 1985; Kim, 1995; Lun, 1996; Rosato and Kim, 1994; Savage and Dai, 1993]. The Couette flow simulations in this research have also been used to study segregation of particles of two different sizes. Previous simulation work on segregation has been conducted for various geometries, including rotary kilns [Cleary *et al.*, 1998], vibrating beds [Gallas *et al.*, 1996], and chute flows [Hirshfeld and Rapaport, 1997].

Previous experiments in shearing of granular materials have focused largely on annular shear cells, in which the granular material is placed between two stationary concentric cylinders and rotating upper and lower plates [Savage and Sayed, 1984; Hanes and Inman, 1985; Craig *et al.*, 1986; Miller *et al.*, 1996]. There have also been several experimental studies on cylindrical Couette flows of dry granular materials, however. Buggisch and Löffelmann [1989] studied the self-diffusion of axially-oriented rods in a concentric cylinder Couette flow experiment. More recently, both Elliot et al. [1998] and Veje et al. [1999] have performed experiments on two-dimensional Couette flows of beads and disks, respectively. Vertically-oriented three-dimensional Couette flow experiments similar to those described in Chapters 4–6 have been per-

formed by Tardos et al. [1998], who investigated stresses in a fluidized powder in a vertical Couette device, and Khosropour et al. [1997], who studied the size segregation of glass beads in a vertical Couette device. Segregation in other geometries has been a popular subject of experimental research as well. Segregation of particle mixtures has been studied experimentally in hoppers [Arteaga and Tüzün, 1990], horizontally rotating cylinders [Nakagawa, 1994], and inclined chutes [Savage and Lun, 1988].

Additional background information on granular material flows can be found in comprehensive review articles of the subject by Campbell [1990] and Savage [1984].

## 1.3 Overview of thesis

The goal of the research in this thesis is to investigate the mechanics of granular material sheared between two solid boundaries. Part of the motivation for this work is the system of toner and carrier particles used in electrophotography. Thus, the research has focused largely on flows of two different sizes of particles and on studying the rheology, energy dissipation, and mixing in these flows. Both experiments and simulations have been used to conduct this research.

Chapter 2 describes the discrete element simulations used to study various Couette flows. Chapter 3 presents results and discussion of computer simulations of Couette flows between two solid infinite plates moving in opposite directions. Results for the wall stresses and energy dissipation are presented, along with a heat transfer analysis of the temperature rise that may result from the energy dissipation into heat. Both flows of same-sized particles and mixtures of two different sizes of particles are analyzed for various solid fractions, solid fraction ratios, and size ratios. The results have also been compared with theoretical predictions derived by previous researchers.

Chapter 4 describes the experimental apparatus and measurement methods used to study cylindrical Couette flows. Chapter 5 presents experimental measurements of mean and fluctuation velocities performed using high-speed imaging techniques.

Results from three-dimensional computer simulations are compared with experimental results for both same-size particle flows and mixtures of two particle sizes. In mixture flows, the segregation of the two sizes is also observed and discussed.

Chapter 6 presents experimental results of wall shear stresses on the outer, stationary wall of the Couette cell. The dependence of the shear stress on the strain rate, height of material, and gap width is investigated. Chapter 7 summarizes the results of the research performed.

# Chapter 2

# Computer Simulations

Computer simulations have been shown to be a valuable tool for studying granular flows in the past [Campbell, 1993; Campbell and Brennen, 1985; Drake and Walton, 1995; Hunt, 1997; Savage and Dai, 1993; Walton and Braun, 1986a; Wassgren, 1997]. Because of the difficulty in making non-intrusive measurements in granular flow experiments, computer simulations are often the only means to provide some types of flow information. Discrete element computer simulations track each individual particle in a flow, providing information on its position and velocity at every timestep. Furthermore, every particle collision is modeled individually so that the energy dissipated during a contact can be determined directly.

The computer simulations used in this work are two-dimensional and three-dimensional soft particle discrete element simulations. The forces on each particle are calculated and Newton's second law is integrated to find the acceleration, velocity, and position of each particle at each timestep. The forces on each particle consist of normal and tangential contact forces, gravity forces, and/or electrostatic forces, depending on the application. A summary of the current simulation is provided in this chapter, and additional details can be found in the thesis by Wassgren [1997].

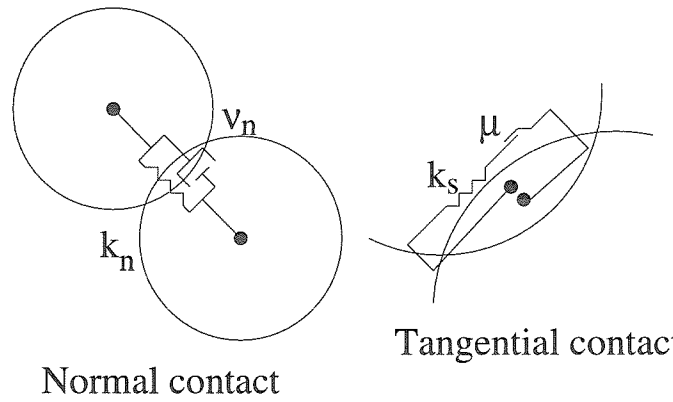


**Figure 2.1** Spring-dashpot contact model.

## 2.1 Particle forces

Discrete element simulations can be used to model many different forces acting on the particles. In the current work, the simulations model contact forces, gravity forces, and inter-particle electrostatic forces. It is assumed that interstitial fluid forces and cohesive forces, both significant in the flows of fine particles, are negligible.

### 2.1.1 Contact forces

When two particles (or a particle and a solid boundary) come into contact, they are allowed to overlap slightly (see figure 2.1). The timestep of the simulation is chosen so that this overlap does not exceed one percent of a particle diameter. In the current simulations, all the particles are round. Collisions between perfectly round particles are simple to detect and allow for an efficient simulation. Solid boundaries in the simulations are flat (not with particles glued to them) and rigid; they have a coefficient of friction associated with them as well. In the current shear flow simulations, either one or both boundaries move in order to drive the flow.

Two different normal contact models were used during the course of this work, and are described in this section. The first model, used for all of the simulations of Chapter 3 and most of the simulations in Chapter 5, is the linear spring and

dashpot normal contact model, adapted from Cundall and Strack [1979], and also used by Wassgren [1997]. The second is the partially-latching spring model from Walton [1986a; 1995]. Only one tangential model (a linear spring and frictional slider) has been used. These models are described in detail later in this section.

A contact between two round particles is detected when the distance between two particle centers is less than the sum of their radii. That is, the overlap between the two circular or spherical particles $i$ and $j$ is determined as follows:

$$\Delta = (r_i + r_j) - |\vec{x}_j - \vec{x}_i| \geq 0, \tag{2.1}$$

where $\vec{x}_i$ and $\vec{x}_j$ are the positions of the two particles in space. The overlap between a particle and a solid boundary is similarly detected when the distance between them is less than the particle radius. If the overlap $\Delta$ is positive, then the two bodies are in contact. In this case of $\Delta > 0$, normal and tangential contact forces are calculated.

### First contact model: linear spring and dashpot

The normal contacts are modeled by a linear spring and dashpot so that

$$F_n = -k_n \Delta + \nu_n \delta \dot{x}_n, \tag{2.2}$$

where $F_n$ represents the normal force on the contact, and $k_n$ and $\nu_n$ are the normal spring constant and damping coefficient respectively. $\Delta$ is the overlap between the two contacting surfaces. The damping coefficient is calculated based on a chosen coefficient of restitution and multiplies the relative normal velocity of the two contacting surfaces, $\delta \dot{x}_n$. Tangential contacts are modeled by a linear spring and frictional slider. The tangential force is first calculated from the spring-displacement law,

$$F_{s,spring} = -k_s \delta s, \tag{2.3}$$

where $k_s$ is the tangential spring constant and $\delta s$ is the tangential displacement between the initial contact points. Then the friction force is calculated using a friction coefficient $\mu$:

$$F_{s,friction} = \mu F_n. \tag{2.4}$$

The force used in the simulation is the lesser of these two forces. If the friction force is lower, then it is assumed that the surfaces are slipping against each other. If the spring force is lower, then it is assumed that the two surfaces are "sticking" and there is no energy dissipation. This calculation occurs at each time step of the contact, and each contact usually lasts 40 to 50 time steps. Thus, during a single collision, both sticking and slipping may occur at the contact point.

### Second contact model: partially latching spring

In this model, which is used for comparison with the spring/dashpot model in certain three-dimensional simulations in Chapter 5, the normal contact force is calculated slightly differently. The normal force between two overlapping surfaces is

$$F_n = -k_{n1}\Delta \tag{2.5}$$

while the spring is loading, and

$$F_n = -k_{n2}(\Delta - \Delta_0) \tag{2.6}$$

for unloading. Thus, there are two different normal spring constants in this model, and they are related by the coefficient of restitution as follows:

$$e = (k_{n1}/k_{n2})^{1/2} \tag{2.7}$$

$\Delta$ is the overlap of the two surfaces, and $\Delta_0$ is the value of $\Delta$ at which the unloading curve goes to zero. If the expression $(\Delta - \Delta_0)$ is negative, the force is equal to zero; that is, no tensile forces are allowed. The tangential model is the same as described above for the first model.

### 2.1.2 Gravitational forces

Some simulations in this research include the effect of gravity. In these cases, the gravitational force on each particle is given by:

$$F_{gravity} = mg \tag{2.8}$$

where $m$ is the particle mass and $g$ is the acceleration due to gravity. This force acts in the direction of gravity for the given simulation.

### 2.1.3 Electrostatic charge forces

Some simulations of binary mixtures include the effect of electrostatic charging between particles. These simulations are intended to model carrier/toner flows in electrophotographic devices, such as photocopiers and high-speed laser printers. It is necessary to make several approximations to simulate this flow, however. The first assumption made is that the charge on each particle is constant. Thus, the actual charging process is not modeled, and neither is the transfer of charge from one particle to another during contact. The second assumption is that the electrostatic charge is uniformly distributed on the surface of the circular particles. A third assumption is that the particles are perfectly spherical.

The last two assumptions allow for the treatment of the particles as spherical shells of uniform charge. Two shells with a uniform charge densities $\sigma_i$ and $\sigma_j$ and radii $r_i$ and $r_j$ exert the same force on each other as two point charges with strength $q_i$ and $q_j$ placed at their centers, where $q_i = 4\pi r_i^2 \sigma_i$. The above assumption allows

for a relatively simple implementation of the rather complex problem of electrostatic charging in granular flows. In the carrier/toner system, although the carrier particles are usually spherical, toner particles are certainly not; that is, the center of charge does not coincide with the center of mass. In the real flow, surface charges migrate and dipoles may be created. All of these effects are ignored in the present context. Nevertheless, despite the simplistic nature of the implementation of charge, the simulations are able to capture some qualitative behavior of the real system.

Following from the assumption of each particle behaving as a spherical shell of uniform charge, a single point charge is placed in the center of each particle. The force on a particle due to the charge on every other particle within a specified distance is calculated in the simulation. The force interaction between each pair of point charges is calculated based on Coulomb's law:

$$F_{charge} = \frac{\alpha q_i q_j}{4\pi\epsilon_0 |\vec{x}_j - \vec{x}_i|^2}, \tag{2.9}$$

where $q_i$ and $q_j$ are the magnitudes of the charges on particles $i$ and $j$ respectively, $|\vec{x}_j - \vec{x}_i|$ is the distance between the particle centers, and $\epsilon_0$ is the permittivity of free space. $\alpha$ is a polarization correction and depends on the dielectric constant, $\frac{\epsilon}{\epsilon_0}$. The value for $\alpha$ used in the simulations is 1.9, obtained from xerography literature [Eklund *et al.*, 1994].

Coulomb's law does not hold as stated above if both point charges are moving. Although the particles are moving, they move an insignificant amount during one timestep. The electrostatic forces between particles are calculated every time the fastest particle in the flow has moved one-tenth of a small particle diameter; it is assumed that this motion is small enough so that Coulomb's law still applies. Thus, the simulation makes the fourth assumption that the system is quasi-static, so that Coulomb's law can be utilized.

## 2.2 Equations of motion

The vector sum of the forces discussed above is determined for each particle in the simulation. Using this total force, Newton's second law is used to find the particle acceleration, $\ddot{\vec{x}}$:

$$m\ddot{\vec{x}} = \vec{F}_{total} = \vec{F}_{contacts} + \vec{F}_{charge} + \vec{F}_{gravity} \tag{2.10}$$

$$I\ddot{\vec{\theta}} = \vec{r} \times \vec{F}_{contacts}, \tag{2.11}$$

where $\vec{F}_{contacts}$ is the sum of all the contact forces on the particle. If no other particles or boundaries are in contact with the particle, the contact force is zero. Similarly, if there is no electrostatic charging or gravity in the simulation, those terms are zero as well. Both gravitational and electrostatic forces act on the center of the particle, but tangential contact forces act on the particle surface. Therefore, the angular acceleration $\ddot{\vec{\theta}}$ is related to the torque exerted on the particle by contact forces. $I$ is the particle moment of inertia, and $\vec{r}$ is the vector connecting the particle center to the point of contact. The moment of inertia is given by $I = \frac{2}{5}mr^2$ in all the current simulations, so that even in two-dimensional simulations, the particles act as spheres constricted to move in two dimensions. The particle mass is similarly given by $m = \frac{4}{3}\pi r^3$.

The velocities and positions of the particles are determined by integrating the equations of motion in time numerically:

$$\dot{\vec{x}}_n = \dot{\vec{x}}_{n-1} + \ddot{\vec{x}}_n \Delta t \tag{2.12}$$

$$\vec{x}_n = \vec{x}_{n-1} + \dot{\vec{x}}_n \Delta t \tag{2.13}$$

$$\dot{\vec{\theta}}_n = \dot{\vec{\theta}}_{n-1} + \ddot{\vec{\theta}}_n \Delta t \tag{2.14}$$

$$\vec{\theta}_n = \vec{\theta}_{n-1} + \dot{\vec{\theta}}_n \Delta t \tag{2.15}$$

where $n$ is the present timestep. The first order integration allows for the conservation of energy at every timestep, which is necessary to calculate the amount dissipated.

## 2.3 Determination of contact parameters

The parameters used in the contact model are the spring constants $k_n$, $k_{n1}$, $k_{n2}$, and $k_s$, the dashpot coefficient, $\nu_n$, and the timestep, $\Delta t$. The method used for the calculation of $k_n$, $k_s$, and $\nu_n$ is identical to that of Wassgren [1997] and is explained in further detail in that work. The calculation of $\Delta t$ is slightly different and is explained later in this section.

The normal spring constant for the spring/dashpot contact model, $k_n$, and the loading spring constant in the latching-spring model, $k_{n1}$, are equal and determined in the same manner. They are calculated based on the maximum allowable overlap between surfaces during a collision, $\Delta_{\max}$, which is set by the user. The spring constants also depend on the maximum relative velocity of the two bodies (either two particles or a particle and a boundary), $\delta\dot{x}_{n,\max}$, their masses, $m_i$ and $m_j$, and the coefficient of restitution, $e$.

From the damped linear spring model (see Wassgren [1997]), one can determine the necessary spring constant for a given maximum allowable overlap:

$$\frac{k_{n1}}{m^*} = \frac{k_n}{m^*} = \left(\frac{(\delta\dot{x}_{n,\max})}{\Delta_{\max}}\right)^2 \left(\exp\left(\frac{\arctan(-\pi/\ln e)}{\pi/\ln e}\right)\right)^2 \tag{2.16}$$

where $m^* = m_i m_j/(m_i + m_j)$ is the equivalent mass of the two bodies. All boundaries in the given simulations are rigid, so that their masses tend to infinity; thus, the equivalent mass $m^*$ of a particle/boundary collision is equal to the mass of the particle. Maintaining a constant value of $k_n/m^*$ in a simulation of particle mixtures results in the following result: when a small particle collides with another small particle, a different spring constant is used than when a small particle collides with a large particle; similarly for large particles. Thus, the spring constant is not a property of a

particular particle, but of the collision it is undergoing.

In the partially-latching spring model, the second normal spring constant, $k_{n2}$, is calculated using the coefficient of restitution, $e$, for the particular collision:

$$\frac{k_{n2}}{m^*} = \frac{k_{n1}}{m^*}\frac{1}{e^2}. \tag{2.17}$$

For the spring-dashpot model, the dashpot coefficient, $\nu_n$, is determined from the above variables as well as the coefficient of restitution, $e$, as follows:

$$\frac{\nu_n}{m^*} = \sqrt{\frac{4\frac{k_n}{m^*}}{1+(\pi/\ln e)^2}} \tag{2.18}$$

Cundall and Strack [1979] suggest the use of a tangential spring constant such that

$$\frac{2}{3} \leq \frac{k_s}{k_n} \leq 1 \tag{2.19}$$

based on previous analytical models of tangential contacts. The current simulations utilize $k_s = k_n$ and $\Delta_{\max} = 0.01$.

Finally, the timestep of the simulation is set to be a small fraction (in the current work, either 1/40 or 1/50) of the duration of a typical collision. The collision time, $\tau$, depends on $k_n/m^*$ as follows:

$$\tau = \frac{\pi\sqrt{1+\left(\frac{\ln e}{\pi}\right)^2}}{\sqrt{\left(\frac{k_n}{m^*}\right)}} \tag{2.20}$$

## 2.4 Calculation of energy dissipation

Using the spring-dashpot contact model described above, the amount of energy dissipated in each collision is calculated directly. The energy dissipated in the inelasticity

of the contact is equal to the dissipation in the dashpot of the normal contact model:

$$\Delta E_i = \nu_n (\delta \dot{x}_n)^2 \Delta t, \tag{2.21}$$

where $\Delta E_i$ is the energy dissipated in the dashpot in one time step, and $\Delta t$ is the timestep. The energy dissipated in the tangential portion of the contact is equal to the tangential force multiplied by the distance the contact slips:

$$\Delta E_f = F_s \delta s. \tag{2.22}$$

This quantity is only valid when the contact is slipping, so that $F_s = F_{s,friction}$, as described in section 2.1.1. The total energy dissipated in a contact in one timestep is $\Delta E = \Delta E_i + \Delta E_f$.

## 2.5 Implementation

The simulation code is written in *C* and a version of it is included in the Appendix of Wassgren's thesis [1997]. The most computationally intensive part of running a discrete element simulation is checking particles for contacts. Two methods have been used to make this process as efficient as possible. The first is the use of a grid of cells in the domain of the simulation. The second is the use of nearest neighbor lists for each particle.

The use of cells in the simulation is explained in detail by Wassgren [1997]. A cell is a data structure associated with a certain integer location in the domain $x$, $y$, and $z$ ($z$ is only necessary if the simulation is three-dimensional). Each cell is the first element of a double-linked list of the particles that exist within that cell. Similarly, each particle also keeps an account of what cell it is in, based on the location of its center in the grid. Thus, knowing the cell of a given particle, the cells surrounding that cell can be checked for particles that are close to the given particle. Each cell is

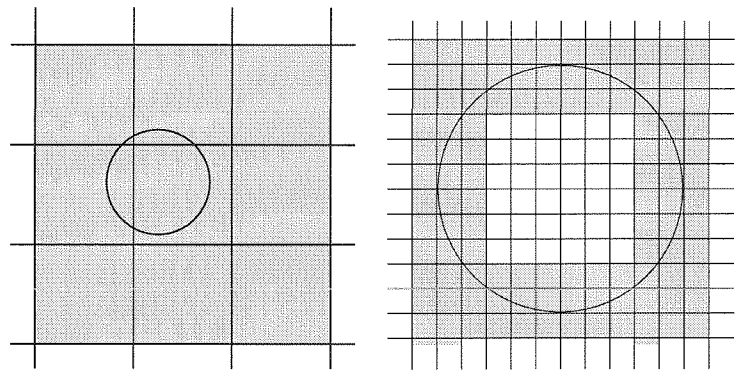

(a) (b)

**Figure 2.2** Particle with surrounding cells, for a small particle (a) and a large particle with large to small particle diameter ratio of ten (b). The shaded cells are those being checked for small particle neighbors. For simplicity in the algorithm, some cells, located inside the large particle, are checked unecessarily.

a cube (or a square, in two dimensions) that is slightly larger than one small particle diameter on each side. The cell lists are updated every timestep. When it is necessary for a large particle to check its neighboring cells, all the cells surrounding it in a frame are checked for small particles close to it, as shown in figure 2.2(b). The large particles check for small particles in this manner; usually there are relatively few large particles so that each large particle checks every other large particle without the use of cells. The cell-checking method greatly increases the efficiency of the simulation.

The second method for improving efficiency is the use of nearest neighbor lists. Let the current particle of interest be labeled particle $i$. Once the cell-checking method provides the particles close to particle $i$, the distance between each candidate (call it particle $j$) and particle $i$ is found. If this distance is smaller than a predetermined maximum distance $D_{max}$, then particle $j$ is added to particle $i$'s nearest neighbor list. Thus, the length of each side of each cell is equal to $d_{small} + D_{max}$, or one small particle diameter plus the maximum distance a particle will travel before rechecking for neighbors. At each timestep, the fastest particle is found and the distance it

traveled in that timestep is calculated. The distance the fastest particle has traveled is tracked at every timestep, and when the total distance reaches $D_{max}$, the neighbors are reevaluated. That is, the cells are rechecked for neighbors as soon as the fastest particle has traveled a distance $D_{max}$, which is usually set to be from 10 to 40% of a small particle diameter. At every timestep, only the neighbor lists for each particle are checked for contacts, saving calculation time.

In simulations with electrostatic charge most of the computer time is used calculating the electrostatic charge forces between particles. In these simulations, the cells are used to calculate the forces due to particles up to only ten cells away from each particle. Simulations using this approximation were found to give the same results as those that calculated the full force field. Because the flows are dense, however, the simulations with charge are still significantly slower than those without. A second time-saving approximation is made in these simulations: the electrostatic portion of the particle forces is only updated whenever the fastest particle has moved 10% of a small particle diameter, not at every timestep. This procedure saves a considerable amount of time because the timestep is often very small due to the contact parameters (one collision takes 50 timesteps to occur). Even the fastest particles move negligible amounts in only one timestep. By allowing the electrostatic charge force to be updated only when a distance criterion is reached, the simulation becomes more efficient.

A summary of the simulation is shown in figure 2.3.

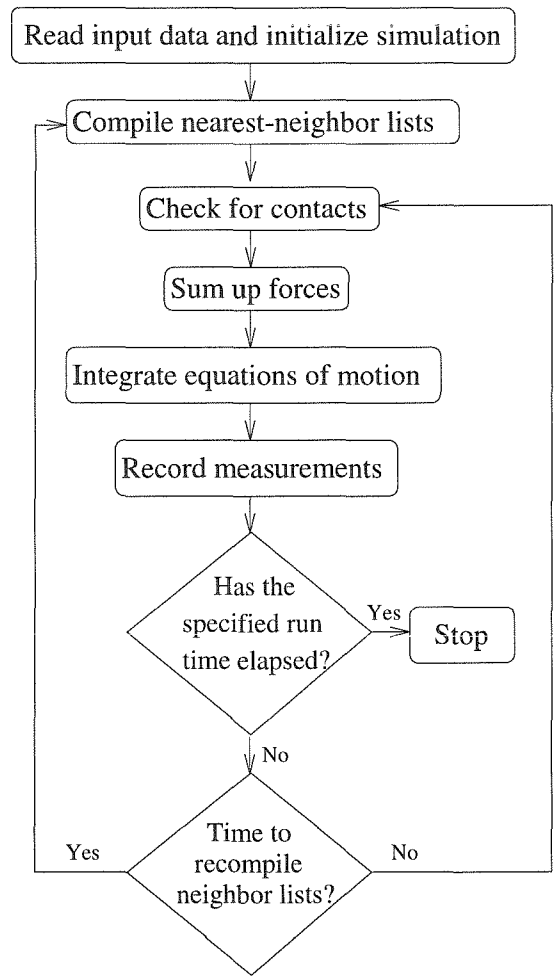


**Figure 2.3** Flow chart describing computer simulation.

# Chapter 3

# Simulations of Planar Couette Flows

Simulations of a gravity-free Couette flow were conducted using the two-dimensional discrete element simulations described in Chapter 2, with the linear spring and dashpot contact model. Particles in these simulations are in a channel between two infinite, solid, flat bounding walls a fixed distance $h$ apart, that move with velocities $\pm U/2$ in opposite directions. The upper wall travels to the right and the lower wall to the left. The right and left boundaries of the domain are periodic, so that a particle exiting on the right enters on the left with the same velocity and vertical position. Periodic boundaries enable the simulation of an infinite domain using a finite number of particles. Simulations were conducted for both mono-sized particle flows and for flows of binary mixtures of particles at various diameter ratios $\phi$. Table 3.1 shows the geometric and contact parameters utilized for these simulations. The solid fraction of the flow is defined as the total area occupied by particles divided by the area of the domain. The single-sized particle flows have solid fractions varying from 0.45 to 0.8 in increments of 0.05. Mixture flows were conducted at varying solid fraction ratios of small to large particles ($R = \nu_{small}/\nu_{large}$) for a constant overall solid fraction of 0.75. The particle density is 1280 kg/m$^3$, the approximate density of toner, for all particles. The friction coefficient for inter-particle and particle-wall collisions, $\mu$, is 0.5. This value of the friction coefficient was chosen so that it was a reasonable value physically while still being high enough to show a large amount of frictional

| parameter | | $\phi = 1$ | $\phi = 2$ | $\phi = 5$ | $\phi = 10$ |
|---|---|---|---|---|---|
| strain rate | $U/h$ | $250s^{-1}$ | $250s^{-1}$ | $250s^{-1}$ | $250s^{-1}$ |
| width | $w/d$ | 50 | 75 | 75 | 100 |
| height | $h/d$ | 10, 20, 40 | 40 | 40 | 40 |
| solid fraction | $\nu$ | 0.45–0.8 | 0.75 | 0.75 | 0.75 |
| solid fraction ratio | $R$ | - | 0.5–5 | 0.4–5 | 0.5–5 |
| coefficient of restitution (particle/particle) | $e_p$ | 0.8 | 0.8 | 0.8 | 0.8 |
| coefficient of restitution (particle/wall) | $e_w$ | 0.8 | 0.8 | 0.8 | 0.8 |
| coefficient of friction (particle/particle) | $\mu_p$ | 0.5 | 0.5 | 0.5 | 0.5 |
| coefficient of friction (particle/wall) | $\mu_w$ | 0.5 | 0.5 | 0.5 | 0.5 |
| number of particles | $N$ | 290–2037 | 1425–2520 | 880–2394 | 1326–3006 |
| number of large particles | $N_l$ | 0 | 120–475 | 19–80 | 6–26 |

**Table 3.1** Values of various parameters in planar Couette flow simulations for various size ratios, $\phi$.

dissipation. Another reason for a relatively high friction coefficient is that because the walls are flat, the friction between walls and particles is the only force driving the flow; a friction coefficient of 0.5 is high enough to achieve a steady Couette flow with significant shearing at the wall. The coefficient of restitution for all collisions, $e_w = e_p$, is 0.8. This value of the coefficient of restitution in the normal direction is chosen based on a typical value used by previous researchers [Savage and Dai, 1993; Campbell, 1993] and is reasonable for a number of materials.

Each particle is simulated as a sphere constricted to move in only two dimensions. Thus, each particle has the mass and moment of inertia of a sphere, not a rod. All simulations began with the initial condition of randomly placed particles with small random velocities. Simulations were run until the kinetic energy in the system became approximately constant. After this steady-state was reached, measurements were made over many time steps and averaged in time and over the length of the domain to gather data about the simulation.

In many dense simulations of mixtures the velocity profile was not fully symmetric even after the kinetic energy in the flow was constant. The velocity profile was not centered at zero, and hence there was a net momentum flux in one direction. After many time steps, the net momentum flux often changed directions or diminished, but this phenomenon could not readily be explained. Even when special care was taken so that the initial density distribution was uniform and the particles were given a zero initial velocity, the flow exhibited these unsteady effects. Average velocities in the flows, which should have been zero due to symmetry about the centerline, reached up to 4% of the wall velocity $U$ in some cases. Similar effects were observed by Savage and Dai [1993] in dense, bounded shear flows of identical particles as well, although for the current flows they were more prominent in the simulations of mixtures. This behavior is likely due to the periodic boundaries used in the simulations. If, at some point in the flow, there is a strong collision with one of the moving walls, there will be an instantaneous momentum flux in one direction. Due to the periodic boundaries, the particles will continue to move in that direction beyond the boundaries because they re-enter the flow with the same velocity. The motion is not hampered by other particles further down the channel. This effect is probably the result of the small size of the domain in the $x$ direction in comparison with the size of the large particles in the flow. A large particle may feel its own effect on the flow through the periodic boundaries. This is also more likely to occur in dense flows in which the particles may travel in one direction like a solid block.

## 3.1 Monosize particle flows

### 3.1.1 Flow measurements

Local measurements of flow properties are made by averaging across horizontal strips in the domain. The height of each strip is slightly larger than one small particle diameter (ranging from $1.01d_{small}$ to about $1.05d_{small}$). Averages are weighted by

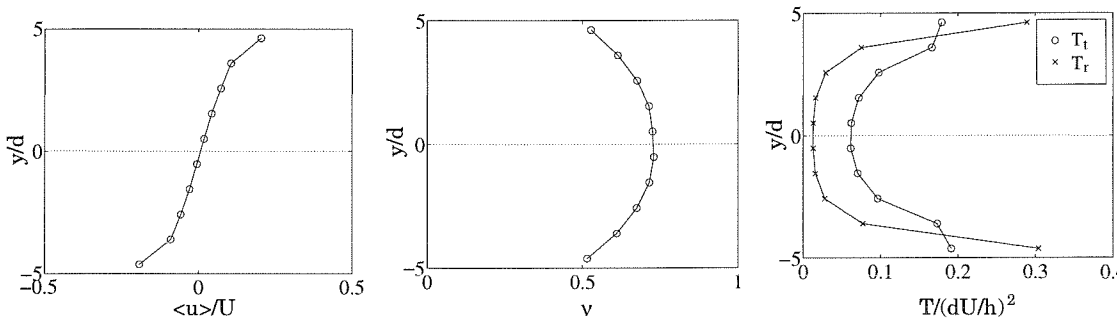


(a) Velocity (b) Solid fraction (c) Granular temperature

**Figure 3.1** Velocity, solid fraction, and granular temperature profiles for Couette flow of same-size particles ($\phi = 1$) with overall $\nu = 0.65$ and $h/d = 10$.

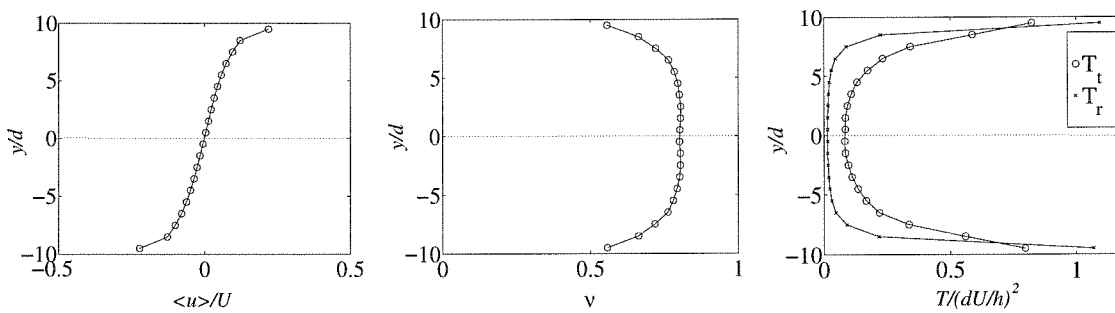


(a) Velocity (b) Solid fraction (c) Granular temperature

**Figure 3.2** Velocity, solid fraction, and granular temperature profiles for Couette flow of same-size particles with overall $\nu = 0.65$ and $h/d = 20$.

area and the fraction of the quantity attributed to a strip is equal to the fraction of the area of the particle in the strip. After reaching steady-state, quantities are averaged over a period of approximately $4 \times 10^6$ to $1.5 \times 10^7$ time steps, or at least 15 wall cycles (the time necessary for one wall to travel the width of the domain). The number of time samples in each average is at least 60, but usually greater.

Figures 3.1, 3.2, and 3.3 show typical velocity, solid fraction, and granular tem-

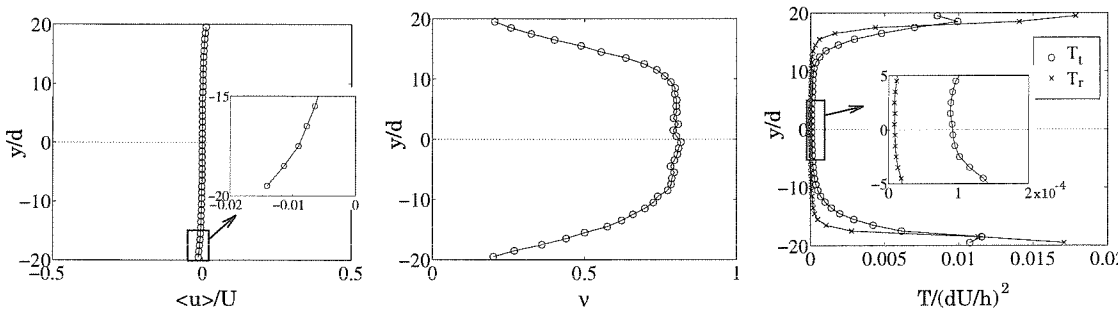


(a) Velocity (b) Solid fraction (c) Granular temperature

**Figure 3.3** Velocity, solid fraction, and granular temperature profiles for Couette flow of same-size particles with overall $\nu = 0.65$ and $h/d = 40$.

perature profiles for a same-size particle flow at $\nu = 0.65$ and three different $h/d$ ratios. Granular temperature is a term used for the fluctuation kinetic energy per unit mass of the flow; it is analogous to thermodynamic temperature in the kinetic theory of gases. The rotational and translational granular temperatures are defined in two dimensions as follows:

$$T_t \equiv \frac{1}{2}\langle u'u' + v'v' \rangle \tag{3.1}$$

$$T_r \equiv \frac{1}{2}\left(\frac{I}{m}\right)\langle \omega'\omega' \rangle, \tag{3.2}$$

where $u$ denotes the velocity component of a particle in the direction parallel to the walls, $v$ is the velocity component in the direction perpendicular to the walls, and $\omega$ is the angular velocity. The fluctuating velocities, $u'$, $v'$, and $\omega'$, are defined as the difference between the particle velocity and the average local velocity. The moment of inertia and mass of each particle are denoted as $I$ and $m$ respectively. The brackets, $\langle\rangle$, denote an area average for the particular bin. Similar qualitative results have been seen in previous studies of bounded Couette flows [Campbell and Brennen, 1985; Campbell, 1993; Savage and Dai, 1993].

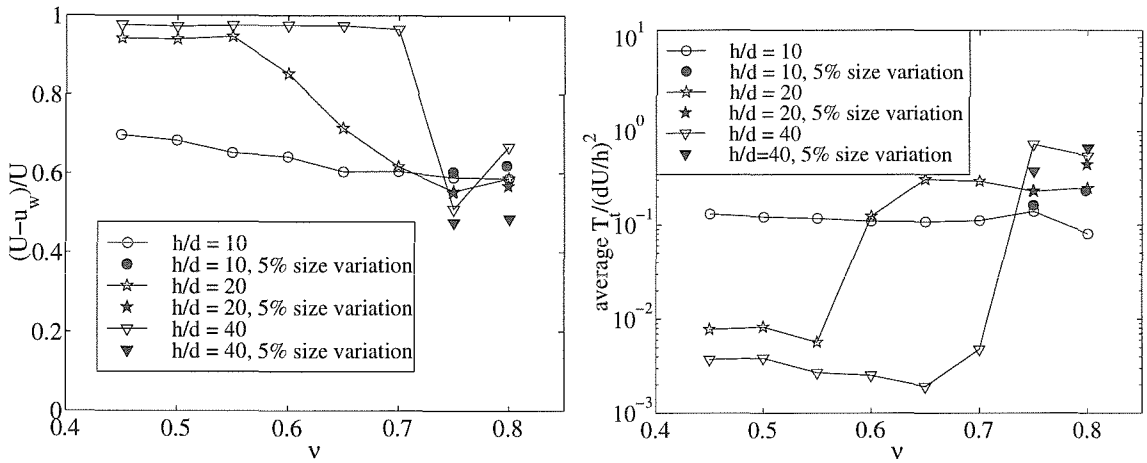


(a) Slip velocity

(b) Average translational granular temperature

**Figure 3.4** Slip velocity and the average translational temperature as a function of solid fraction for various height to particle diameter ratios in mono-sized flows.

The profiles for the flow with $h/d = 10$ are markedly different from those with $h/d = 40$. The velocity gradient is very small when $h/d = 40$, whereas it is much larger when $h/d = 10$. The solid fraction for the larger wall separation is lower at the walls and higher in the center when compared with the flow with a smaller wall separation. The geometry of the flow with $h/d = 40$ allows the particles to concentrate more heavily in the center, leaving the wall regions with a lower concentration. The difference in granular temperature from the wall region to the center of the channel is also much greater for the flow with the larger wall separation.

Slip velocities have previously been shown [Rosato and Kim, 1994; Savage and Dai, 1993] to decrease with increasing solid fraction, and the same is true for the current system, (figure 3.4(a)). The slip velocity is defined as the difference between the relative wall velocity, $U$, and the relative velocity between particles one radius from the top wall and one radius away from the bottom wall, $u_w = u(h - 0.5d) - u(0.5d)$. The filled symbols in figure 3.4 are results from simulations at the two

largest concentrations ($\nu = 0.75$ and 0.8) that were conducted with a 5% deviation in particle size. At the highest solid fraction of 0.8, a hexagonal crystalline structure was formed in the center of the channel at all values of $h/d$, which can be avoided by imposing a small variation in particle size. The values obtained for the slip velocities and granular temperatures for these cases are shown for comparison with those for identical particles.

For $h/d = 40$, except the most concentrated flows, the boundary slip velocities are over 90% of the wall velocity. In flows with $h/d = 20$, only the lowest few solid fractions have slip velocities that high, and all of the flows with $h/d = 10$ slip have lower slip velocities, between 60 and 70%. In all the shear flows the boundary layer against the wall is only a few particles thick and therefore the particles are able to avoid this region when the channel is wide by moving closer to the center. In the flows with $h/d = 40$, it is observed that most particles migrate to the center of the channel and few remain in contact with the wall in the steady state. In flows with a narrower distance between the boundaries, the influence of the wall is felt further into the center of the channel, and the particles are not able to avoid the boundary layer. The slip velocity, therefore, is lower in flows with lower ratios of $h/d$.

The slip velocity dictates the actual strain rate in the flow. Thus, although the imposed strain rate ($U/h$) is constant for all flows, the actual average strain rate increases as the slip velocity decreases. The average strain rate is defined as

$$\left(\frac{du}{dy}\right)_{av} = \frac{u(h-0.5d) - u(0.5d)}{h-d} \tag{3.3}$$

$$= \frac{u_w}{h-d} \tag{3.4}$$

that is, using the difference between the velocities one particle radius away from the wall. The average granular temperature of the system also increases with solid fraction (figure 3.4(b)), due to the increase in energy transferred from the moving walls into the flow.

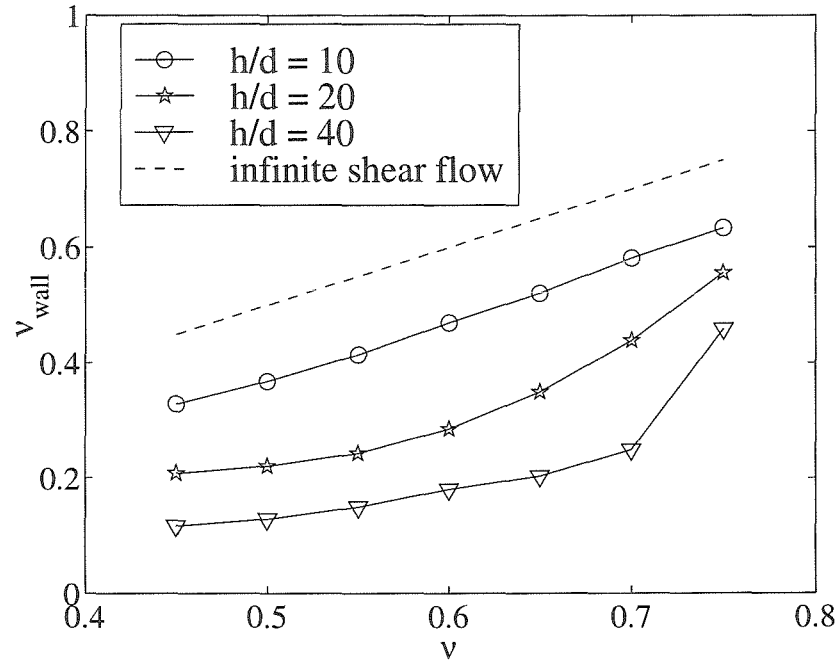


**Figure 3.5** Solid fraction at the wall (evaluated within one particle diameter of the wall) as a function of the average solid fraction.

Figures 3.4(a) and (b) illustrate the existence of a threshold in solid fraction above which the energy in the flow increases rapidly. For flows with $h/d = 10$, all solid fractions show lower slip velocities and high granular temperatures. Flows with $h/d = 20$, however, have very high slip and low temperatures until an average solid fraction of roughly 0.55, after which the slip velocity begins to decrease and the temperature rapidly increases. For flows with $h/d = 40$, this threshold solid fraction is between 0.7 and 0.75. The threshold solid fraction occurs when the particles in the center regions reach a limit of dense packing so that any additional particles must contribute to the concentration near the walls.

Figure 3.5 illustrates that for $h/d = 10$ the wall solid fraction increases approximately linearly with the average solid fraction. At $h/d = 20$, the wall solid fraction is lower than at $h/d = 10$ and increases more rapidly at higher overall solid fractions. The flow at $h/d = 40$ has a low wall solid fraction that suddenly increases above an

average solid fraction of 0.7, the same solid fraction at which the large decrease in slip velocity is observed. For reference, a dashed line with a slope of one shows the result for a constant solid fraction, as in a simple shear flow of infinite width. The results for $h/d = 10$ correspond the closest with a simple shear flow, because the gradient in solid fraction across the gap is the smallest. These results suggest that the wall solid fraction governs the dynamics of the flow and the transition from a high-slip, low-temperature flow to a lower-slip, high-temperature regime. From figure 3.5 it can be inferred that the transitional wall solid fraction is between 0.25 and 0.30. Thus, all of the results at $h/d = 10$ are above this critical value, and transitions occur between average solid fractions of 0.55 and 0.6 for $h/d = 20$ and between 0.7 and 0.75 for $h/d = 40$. The results of this study clearly indicate that the ratio of the gap width to the particle diameter, $h/d$, affects the basic behavior of the flow to a great extent due to variations in the wall solid fraction. The effect of the gap width on a the flow properties of a gravity-free Couette flow has not been studied in the past.

### 3.1.2 Wall stresses

The stress within a granular flow can be separated into a collisional and a streaming component [Campbell, 1993]. The collisional component is the result of momentum transferred in particle collisions and the streaming component is related to the momentum transported by the motion of the particles themselves. The sum of the stresses can be measured at the bounding walls. The collisional forces are averaged over time and over the length of the boundary to give average stresses in both normal and tangential directions. Due to the two-dimensional nature of the simulations, the stresses presented are actually forces per unit length of boundary, not per unit area. Figure 3.6 shows the stresses on the boundary as functions of simulation time for a flow of mono-sized particles. A steady state is reached very quickly, but the stresses continue to show large fluctuations about the mean value.

Figure 3.7 presents the average normal and shear stress on the bounding walls for

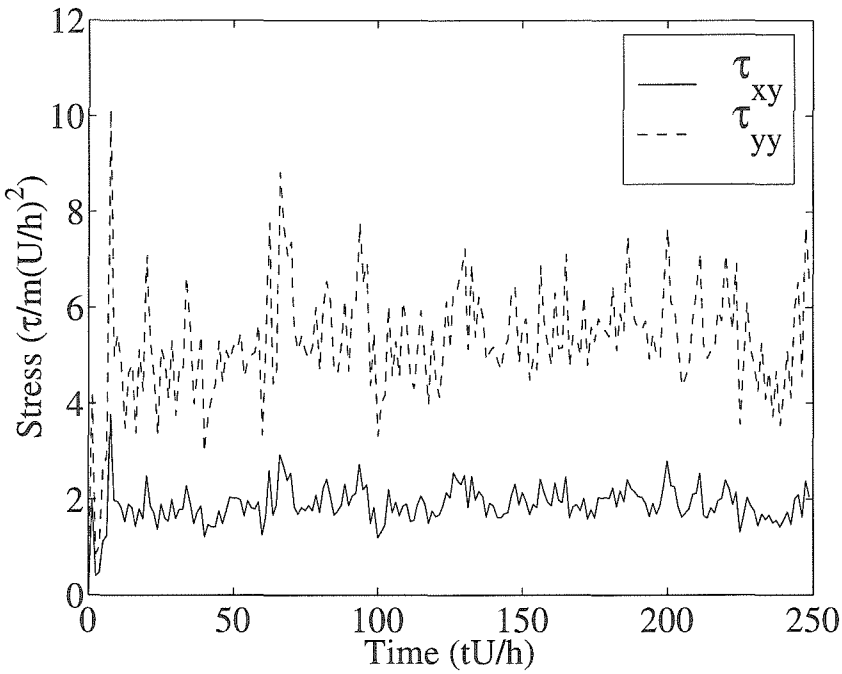


**Figure 3.6** Time variation of the normal ($\tau_{yy}$) and shear ($\tau_{xy}$) stresses at the solid boundaries for a flow of monodisperse particles with an overall solid fraction of 0.75 and $h/d = 20$.

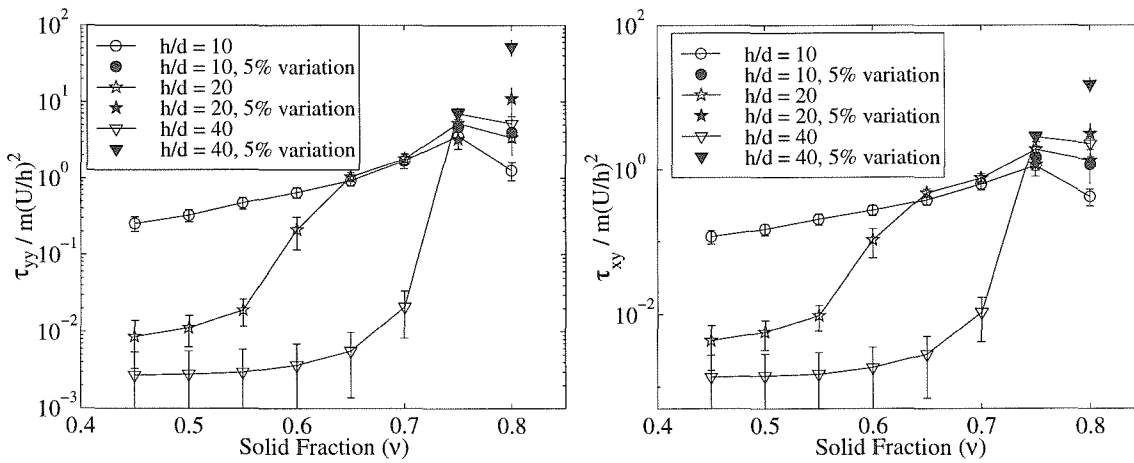


(a) Normal stress

(b) Shear stress

**Figure 3.7** Normal and shear stresses at the boundaries as functions of overall solid fraction in same-size particle Couette flows.

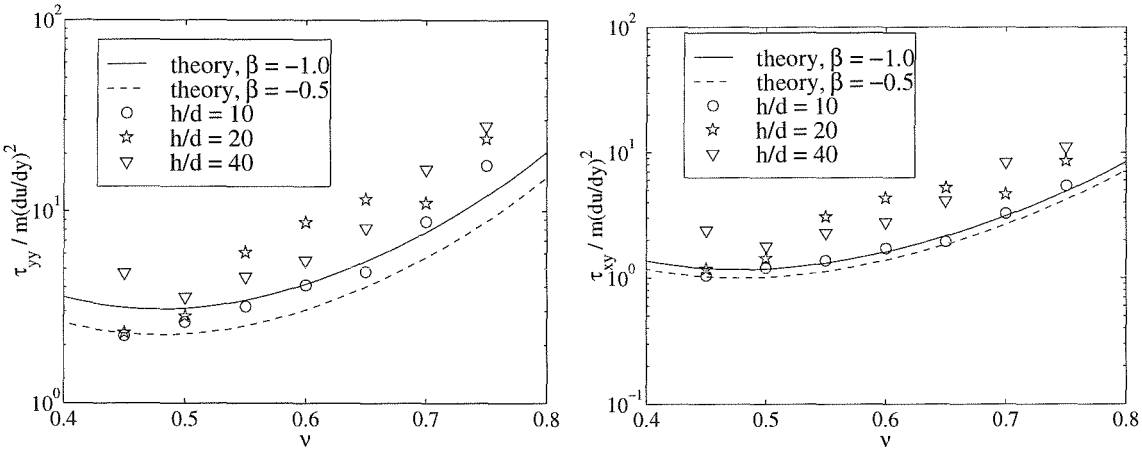


(a) Normal stress

(b) Shear stress

**Figure 3.8** Normal and shear stresses at the boundaries as functions of overall solid fraction in same-size particle Couette flows. Stresses are non-dimensionalized by the actual average strain rate and compared with the kinetic theory of Jenkins and Richman [1985] for a simple shear flow.

flows of same-size particles as a function of solid fraction. The stresses were averaged over time and the standard deviation of the fluctuations has been plotted as an error bar in the figure. Both stresses increase with solid fraction, due to the increase in collision rate with concentration. Flows with $h/d = 40$ show lower stresses at low solid fractions than flows with smaller heights, due to the lower collision rate at the walls and high slip velocities shown earlier. The solid fraction at which the flows with higher $h/d$ ratios approach the results for $h/d = 10$ varies, illustrating that the stresses increase along with the granular temperature at a critical solid fraction that depends on $h/d$. The critical value for $h/d = 20$ is above 0.55, and the value for $h/d = 40$ is even higher, above 0.7.

To explore the relationship between the actual strain rate and the stresses, the shear and normal stresses are shown in figure 3.8 non-dimensionalized by the actual strain rate $(du/dy)_{av}$ (as defined in equation 3.4) instead of $U/h$. These results

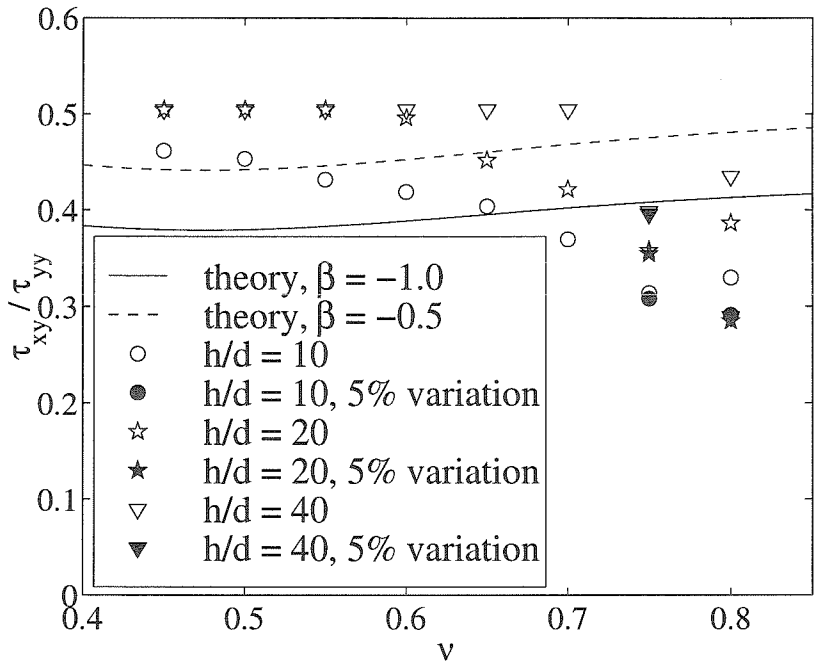


**Figure 3.9** Ratio of shear to normal stress at the boundaries as a function of overall solid fraction in same-size particle Couette flows.

illustrate that the stresses for all three gap widths collapse fairly well onto the same curve. The theory from Jenkins and Richman [1985] for identical rough disks in the limit of nearly elastic, slightly rough particles ($\beta \simeq -1, e \simeq 1$) was used to compare with the present simulation results. The coefficient $\beta$ characterizes inter-particle surface roughness, and ranges from $-1$ to $+1$, with $\beta = -1$ corresponding to perfectly smooth disks. The relationship between the stresses and the total solid fraction was derived by solving the translational energy equation for a simple shear flow with no gradients in granular temperature. Although this is not the case in the current simulations, the curves are plotted simply for comparison, for two different values of $\beta$. The expressions plotted are:

$$\frac{\tau_{yy}}{m(du/dy)^2} = \frac{(1+2\nu g_0)\left[\left(\frac{8}{\pi}+1\right)\nu g_0 + \frac{1}{\nu g_0} + 2\right]}{8g_0\left(\frac{\kappa(1+\beta)}{1+\kappa} + 2(1-e)\right)} \tag{3.5}$$

$$\frac{\tau_{xy}}{m(du/dy)^2} = \frac{\sqrt{\nu}}{8\sqrt{2g_0}} \frac{\left[\left(\frac{8}{\pi}+1\right)\nu g_0 + \frac{1}{\nu g_0} + 2\right]^{3/2}}{\left(\frac{\kappa(1+\beta)}{1+\kappa} + 2(1-e)\right)^{1/2}}, \tag{3.6}$$

where $\kappa = 4I/md^2 = 1/2$ for disks, $e$ is the coefficient of restitution, and $g_0$ is the radial distribution function for disks, evaluated at the contact point, suggested by Jenkins and Richman:

$$g_0 = \frac{16 - 7\nu}{16(1-\nu)^2}. \tag{3.7}$$

This expression was derived from the equation of state of Henderson [1975],which may not be strictly valid at the high solid fractions shown, but it is nevertheless used here for comparison with the simulations. Qualitative agreement between the simulation results is fairly good, although the theory generally under-predicts the stresses. Agreement is best for the simulations with the smallest gap width, $h/d = 10$, because they have smaller gradients in temperature and solid fraction and most closely resemble a simple shear flow.

The ratio of the shear stress to the normal stress decreases with increasing solid fraction (figure 3.9). For $h/d = 20$ and $h/d = 40$ and at low solid fractions, when the slip velocity is over 90%, the ratio is equal to the surface friction coefficient of the simulation, which is set at 0.5. For all three gap widths, the stress ratio decreases with increasing solid fraction. A similar decrease in the stress ratio at high solid fractions has previously been observed both in simple shear flows [Campbell, 1989; Lun and Bent, 1994] and Couette flows [Campbell and Brennen, 1985; Campbell, 1986; Rosato and Kim, 1994]. Campbell and Brennen [1985] explained the decrease in the stress ratio of the collisional components of the stress near the shearable limit by the formation of an internal microstructure. At large solid fractions, the particles were observed to form a layered microstructure that resulted in preferred angles of collision. The layers become more tightly packed and the effect more pronounced

with an increase in density. The preferred collision angles result in a decrease of the shear stress with solid fraction. The ratio of the streaming components of the stresses decreased even more dramatically with solid fraction in that study, resulting in a decrease in the overall stress ratio with solid fraction. The kinetic theory does not predict any such decrease in stress ratio because it does not account for the layering and microstructure observed in dense flows.

The mono-sized particle simulations with a solid fraction of 0.8 show different behavior for both trends in overall stresses and stress ratios. The stresses decrease slightly for this solid fraction and the stress ratio increases slightly. These particular simulations are examples of the unrealistic locking of the particles in the center of the channel mentioned earlier. Results for the two simulations that had a 5% deviation in particle size are also plotted in figures 3.7 and 3.9. While the results for the monodisperse and the 5% dispersed system are very similar for the solid fraction of 0.75, they differ significantly for the solid fraction of 0.8. This result illustrates that at a solid fraction of 0.8 the monodisperse system behaves in a manner that is unrealistic due to the single-size distribution of the particles and the two-dimensionality of the simulation. The results for the highest solid fraction of 0.8 are omitted from figure 3.8. This locking of the particles into a crystalline structure would not occur in a real flow because granular materials in both industry and nature always have some imperfections in the grain size or shape.

### 3.1.3 Energy dissipation and heat transfer

Discrete element computer simulations are ideally suited for the calculation of energy dissipation in the flow. This calculated dissipation can be compared with previous theoretical models for the dissipation. Analytical expressions for the dissipation term in the energy equation for granular materials have been derived using kinetic theory for many cases, including flows of smooth and rough identical particles [Jenkins and Richman, 1985; Lun, 1991; Lun and Savage, 1987; Lun *et al.*, 1984]. The analy-

sis by Jenkins and Richman [1985] most closely resembles the flows in the current simulations, modeling rough two-dimensional inelastic particles.

Jenkins and Richman [1985] derive dissipation terms from kinetic theory for the loss of both translational and rotational energy (referred to as $-\chi_{\alpha\alpha}$ and $-\chi_{33}$ in their work, but referred to here as $\gamma_t$ and $\gamma_r$) due to inter-particle collisions. These terms contain an unknown coefficient of roughness, $\beta$, which ranges from 1 to $-1$, characterizing disks ranging from perfectly rough (conserving all energy due to tangential rebound) to perfectly smooth. The simplification of the general relations for slightly rough and nearly elastic particles ($\beta \simeq -1, e \simeq 1$) is as follows:

$$\gamma_t = 2\frac{\alpha T_t}{d^2}\left(\frac{\kappa(1+\beta)}{(1+\kappa)} + 2(1-e)\right) \tag{3.8}$$

$$\gamma_r = -\frac{\alpha T_t}{d^2}\frac{(1+\beta)}{(1+\kappa)}\left(\frac{\kappa(1+\beta)}{(1+\kappa)} - 4\frac{T_r}{T_t}\right) \tag{3.9}$$

where

$$\alpha = \frac{8}{\pi}\frac{m\nu^2}{d}g_0\left(\frac{T_t}{\pi}\right)^{1/2}$$

$$\kappa = \frac{4I}{md^2}.$$

The translational and rotational granular temperatures are defined in equations 3.1 and 3.2. The factor of 4 in the last term of the rotational dissipation is due to a difference in the definition of $T_r$; in the original work it is a factor of 2.

If equations 3.8 and 3.9 are simplified for smooth disks (the case of $\beta = -1$), the expression for $\gamma_r$ (3.9 becomes zero, since perfectly smooth disks will have no rotational (frictional) dissipation; there will only be dissipation due to the inelasticity of collisions. Substituting $\beta = -1$ into expression 3.8 for $\gamma_t$, a simpler expression for

the overall dissipation $\gamma = \gamma_t$ of smooth disks is:

$$\gamma = \frac{32m\nu^2}{d^3} g_0(1-e)\left(\frac{T_t}{\pi}\right)^{3/2}. \tag{3.10}$$

This equation can be simply derived from the product of the number density, $n$, the collision rate, and the energy lost in each collision. The two-dimensional collision rate is the inverse of the collision interval, $t_c$, which is, from kinetic theory [Hunt, 1997]:

$$t_c = \frac{1}{2\sqrt{\pi} n d g_0 T_t^{1/2}}. \tag{3.11}$$

The energy lost in each collision can be expressed in terms of the granular temperature and a coefficient of restitution:

$$\Delta E = \frac{1}{2} m(1-e)^2 T_t. \tag{3.12}$$

Using the relations $n = 4\nu/\pi d^2$ and $(1-e)^2 \simeq 2(1-e)$ (for $e \simeq 1$), equation 3.10 is obtained using this simple product.

Returning to the more complex expressions of equations 3.8 and 3.9 for the more general case of $\beta$ not equal to $-1$, the sum of the two dissipation terms, $\gamma_r$ and $\gamma_t$, can be calculated. This sum is equal to the total dissipation rate due to particle-particle collisions. The theoretical dissipation terms are evaluated at $\beta = 0$ and $-0.5$ for comparison with simulation results. Figure 3.10 shows simulation results for dissipation rate per unit area, $\gamma$, as a function of position in the flow for one example of a monodisperse flow. The curves shown for the kinetic theory are for $\gamma = \gamma_t + \gamma_r$, as defined in equations 3.8 and 3.9. These expressions from Jenkins and Richman [1985] are functions of local solid fraction and granular temperature; the solid fractions and temperatures used in the calculation are those measured by the simulation. The dissipation rate is high near the walls, where the granular temperature and strain

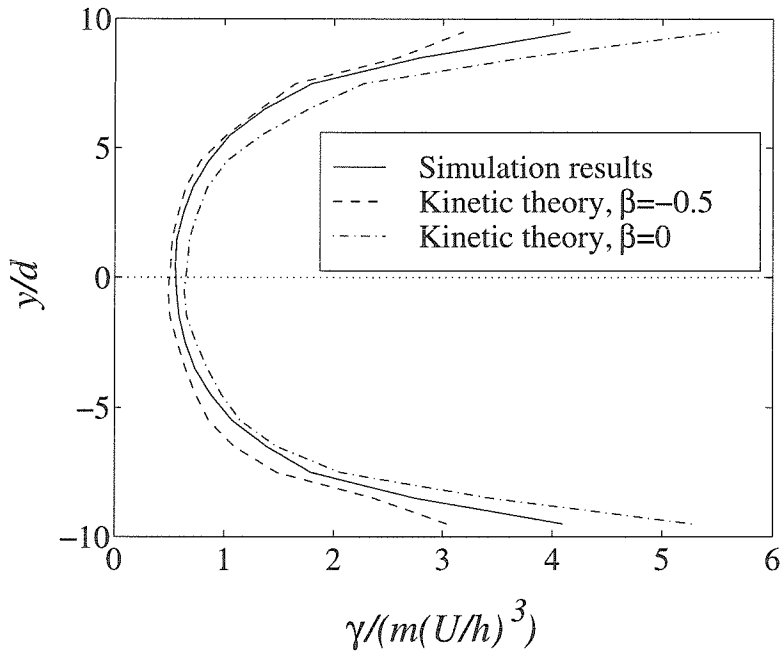


**Figure 3.10** Energy dissipation rate as a function of vertical position for Couette flow of same-size particles with overall $\nu = 0.75$ and $h/d = 20$.

rate are high as well. Figure 3.11 shows the mean dissipation rate per unit area for flows with $h/d = 20$ compared with the kinetic theory results for two different values of the roughness coefficient $\beta$. The theoretical results do not show a smooth curve because they are evaluated at the same points as the simulations and for the granular temperatures from the simulation results. Figure 3.12 shows the same results for simulations run with $h/d = 10$, $h/d = 20$, and $h/d = 40$ for comparison. The dissipation rate rises with solid fraction for all $h/d$ due to higher particle collision rates, but the behavior at low solid fractions depends greatly on the domain height. The high slip velocity at low solid fractions and large $h/d$ shows that only a very small fraction of the energy is transmitted into the flow; most is dissipated at the walls. Thus, the energy within the flow is lower and the energy dissipation rate inside the flow is also smaller than for flows with smaller $h/d$.

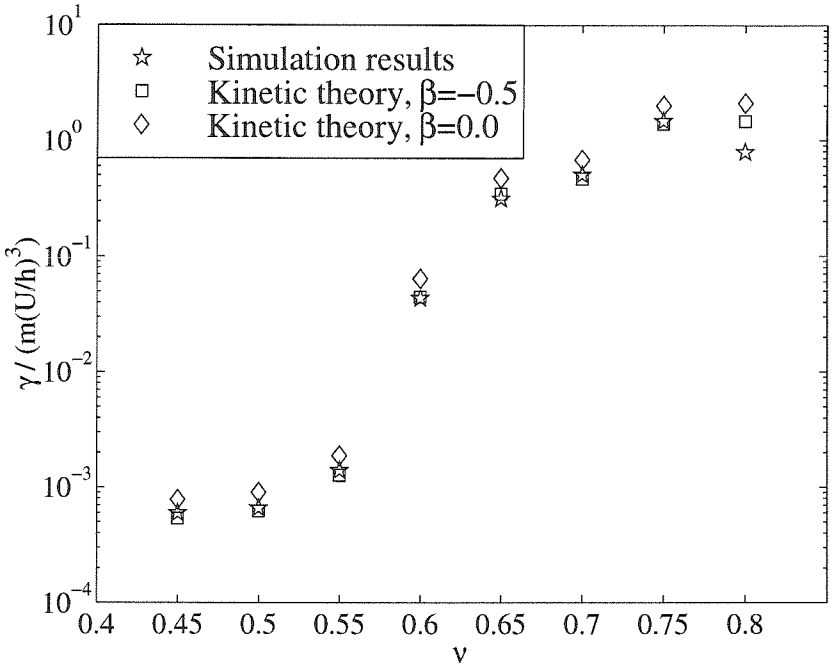


**Figure 3.11** Energy dissipation rate per unit area as a function of overall solid fraction for Couette flow of same-size particles with $h/d = 20$, for simulations and theory.

In addition to the energy dissipation rate inside the flow, the energy dissipation rate at the walls due to particle-wall collisions was calculated in the simulations. The rate of dissipation at the walls, $\Gamma_w$, is compared to the rate of work done by the walls, $W$, to determine the amount of work done on the flow inside the boundaries. The fraction of the work that is dissipated at the boundaries, $\Gamma_w/W$, shown in figure 3.13(a), decreases with overall solid fraction. Figure 3.13(b) shows the rate of work done by the boundaries as a function of solid fraction for same-size flows. The high dissipation rate at low solid fractions for all $h/d$ is consistent with the high slip velocity as shown in figure 3.4(a). The rate of work done by the walls is equal to the total shear force on the wall (the shear stress multiplied by the length of the wall) multiplied by the wall velocity. The rate of work done is necessarily equal to the total energy dissipation rate in the flow at a steady-state. All of the simulations plotted

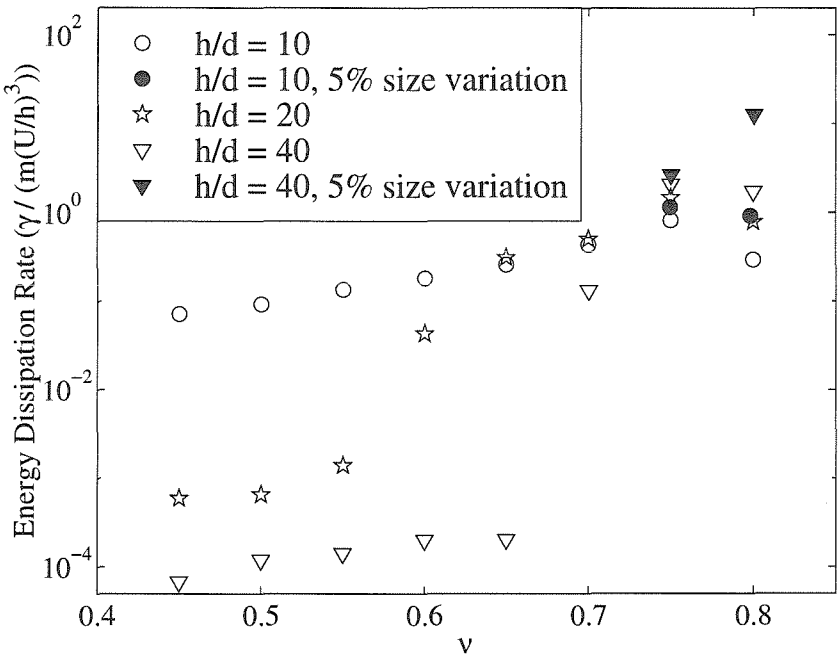


**Figure 3.12** Energy dissipation rate per unit area calculated from computer simulations for same-size particles with various $h/d$.

use the same wall velocity and length, so that the rate of work done is proportional to the shear stress at the wall (shown in figure 3.7(b)).

Although the interstitial gas (air, in this instance) can generally be neglected in the analysis of the dynamics of the flow, it cannot be neglected in the heat transfer. In order to translate the dissipation rates computed in the simulations into actual thermodynamic temperature changes, a heat transfer analysis is performed on both phases of the system. An energy equation can be solved using the total energy dissipation calculated in the simulations as a heat source to obtain thermodynamic temperature profiles in same-size flows. The general energy equation with a heat source term is expressed as:

$$\rho c_p \frac{D\mathcal{T}}{Dt} = \nabla \cdot (k_{tot} \nabla \mathcal{T}) + \gamma, \tag{3.13}$$

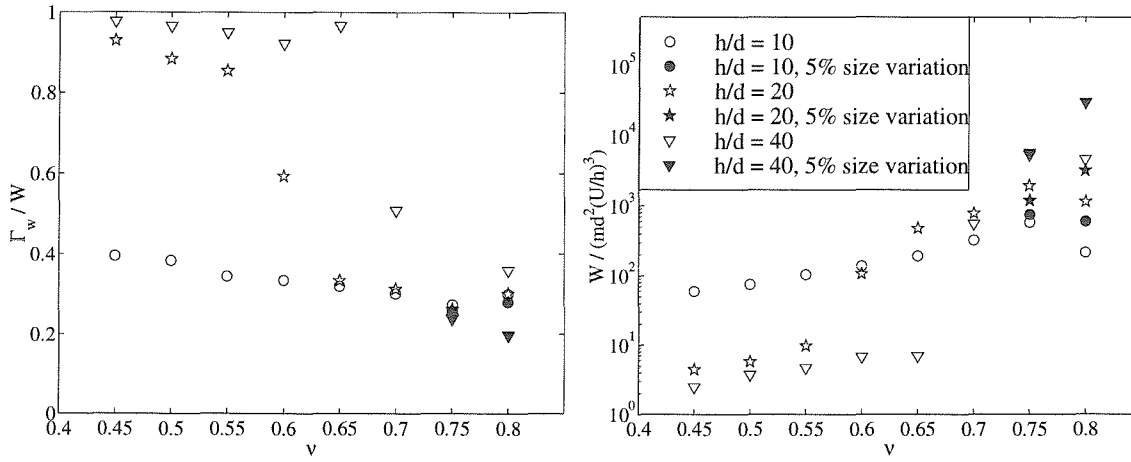


(a) Ratio of energy dissipation rate at wall to rate of work done by walls.

(b) Rate of work done by moving boundaries.

**Figure 3.13** Energy dissipation and work done by the solid boundaries as functions of solid fraction for same-size particle flows for various $h/d$. The legend on the right serves for both graphs.

where $\mathcal{T}$ is the thermodynamic temperature, and $D()/Dt$ is the material, or total derivative. The relation $\nu\rho_p c_p + (1-\nu)\rho_{air}c_{air} \approx \rho c_p$ was used in the above equation, where $\rho_p$ and $c_p$ are the density and heat capacity of the particles, and $\rho_{air}$ and $c_{air}$ are the corresponding values for air. Because this equation is three-dimensional, $\gamma$ represents the total energy dissipation rate per unit volume (due to both friction and inelasticity of collisions), both within the flow and at the walls. The two-dimensional dissipation rate calculated in the simulation is converted to three dimensions by considering the flow as a monolayer of particles constrained to move within the plane. The depth of this monolayer is one particle diameter, so the dissipation per unit volume is calculated based on this depth.

The total conductivity, $k_{tot}$, is defined as in Natarajan and Hunt [1998], as the sum of the molecular conductivity, $k_{mc}$, and the streaming conductivity, $k_{kt}$. The effective molecular conductivity used in the analysis is that proposed by Gelperin

and Einstein [1971]:

$$\frac{k_{mc}}{k_g} = 1 + \frac{\nu\left(1 - \frac{k_g}{k_p}\right)}{\frac{k_g}{k_p} + 0.28(1-\nu)^{0.63(k_g/k_p)^{-0.18}}}. \tag{3.14}$$

In the above expression, $k_g$ and $k_p$ are the conductivities of the gas and solid phases respectively. The expression for a streaming conductivity, $k_{kt}$, was derived using gas kinetic theory by Hsiau and Hunt [1993] in three dimensions, and later extended to two dimensions by Hunt [1997] using similar methods:

$$k_{kt} = \frac{\pi^{3/2}\rho_p c_p d T_t^{1/2}}{32 g_0(\nu)}. \tag{3.15}$$

This expression assumes perfectly smooth particles, and thus only uses the translational granular temperature term. This streaming conductivity is the conductivity due to energy transfer by particle motion from hotter to colder regions. The kinetic theory-derived expression for $k_{kt}$ above also assumes a low particle Biot number for a lumped mass analysis and a small ratio of the time between collisions to the thermal time constant of the particles; it applies to flows of same-size particles only.

A similar conductivity exists to account for the local variations in the fluid velocity, which enhance the energy transport when a temperature gradient exists. In a packed bed of stationary particles, this enhanced thermal transport is modeled using a dispersion conductivity, which is approximated as $k_d = C\rho_f c_f u_f d$, where $C$ is a constant, $\rho_f$ and $c_f$ are the density and thermal heat capacity of the interstitial fluid, $u_f$ is the average velocity, and $d$ is a particle diameter [Hunt, 1990]. Considering this scaling for the dispersion conductivity of a fluid in a packed bed, this contribution to the overall conductivity of the granular system has been neglected in the current analysis, because the density and thermal heat capacity of air are small when compared with those of the solid particles.

Wang et al. [1989] have shown that particle rotation does not affect heat transfer

at low particle rotational Peclet numbers, where $Pe = \omega(d/2)^2/(k_p/\rho_p c_p)$. The flow conditions in the current work have $Pe < 1$, justifying the assumption that rotation does not affect the conductivity of the system significantly.

For two-dimensional steady-state flow with periodic boundaries (i.e., no gradients in the $x$ direction) and no mean velocity in the vertical ($y$) direction, the non-dimensional energy equation reduces to

$$\frac{d}{dy}\left(k_{tot}(y)\frac{d\Theta}{dy}\right) = -\gamma(y). \tag{3.16}$$

The non-dimensional thermodynamic temperature is defined as $\Theta = \frac{\mathcal{T}-\mathcal{T}_0}{U^2/c_p}$, where $\mathcal{T}_0$ is the temperature at $y = h$. The total conductivity can be determined from equations 3.14 and 3.15 using the solid fraction and granular temperature profiles obtained from the simulations. Likewise, the non-dimensionalized dissipation term $\gamma$ is also known from the simulations, and equation 3.16 can be solved by integrating directly for the thermodynamic temperature profile. The dissipation rate, solid fraction, and granular temperature calculated in the simulations are averaged over the width of each bin, that is they are only known at discrete points. The bins are chosen to be one particle diameter wide in order to provide a sensible average for a continuum analysis. The two boundary conditions consist of an adiabatic wall condition at $y = 0$ and a fixed temperature at the upper wall $y = h$:

$$q_h|_{y=0} = k_{tot}\left.\frac{d\Theta}{dy}\right|_{y=0} = 0 \tag{3.17}$$

$$\Theta|_{y=h} = 0. \tag{3.18}$$

The solution in this case is:

$$\Theta(y) = \int_0^h \frac{1}{k(y)}\left(\int_0^y \gamma(y')dy'\right)dy - \int_0^y \frac{1}{k(y')}\left(\int_0^{y'} \gamma(y'')dy''\right)dy', \tag{3.19}$$

which is integrated numerically to give $\Theta(y)$. Figure 3.14(a) shows the dimension-

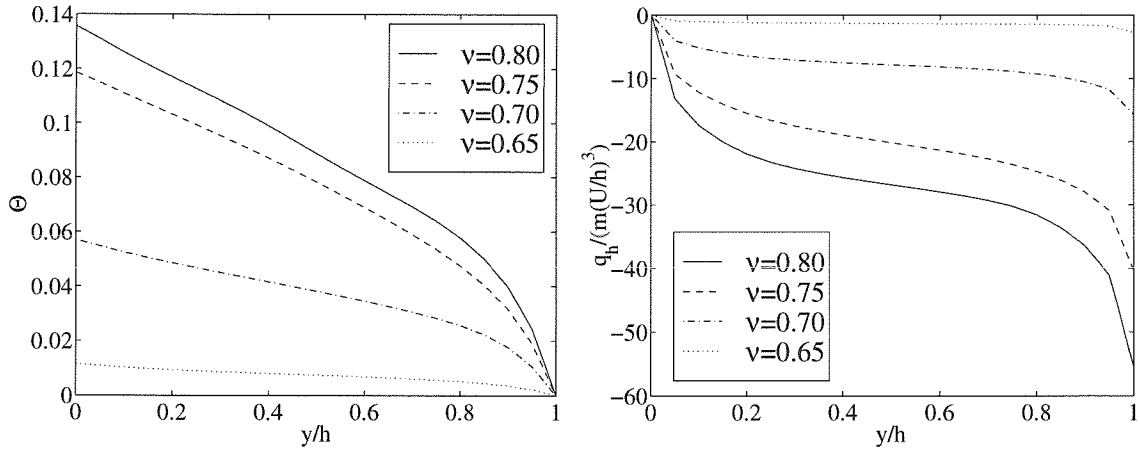


(a) Temperature

(b) Heat flux

**Figure 3.14** Non-dimensional thermodynamic temperature ($\Theta$) and heat flux ($q_h$) profiles for same-size flows of various overall solid fractions. The conductivity ratio is $k_p/k_g = 23$.

less thermodynamic temperature as a function of the vertical distance in the flow for various solid fractions at a constant conductivity ratio, $k_p/k_g = 23$, which is approximately that found in the flow of toner in a high-speed laser printer. The temperature increases with solid fraction due to the higher dissipation rate of denser flows. The heat flux is also plotted in this figure, showing that it is equal to zero at the adiabatic wall.

The slope of the temperature profile does not approach zero near the adiabatic wall due to the finite size of the bins over which the integration and properties are calculated (bins are approximately one particle diameter in width). The finite value of the heat flux one bin away from the wall results in a finite value of the derivative of the temperature near the wall as well. Decreasing the size of the bins will not alleviate this issue because of the heat generated at the wall itself, which causes a non-zero value of the heat flux at any finite distance from the wall. The relatively large bin size does not affect results away from the two walls, where there are smaller

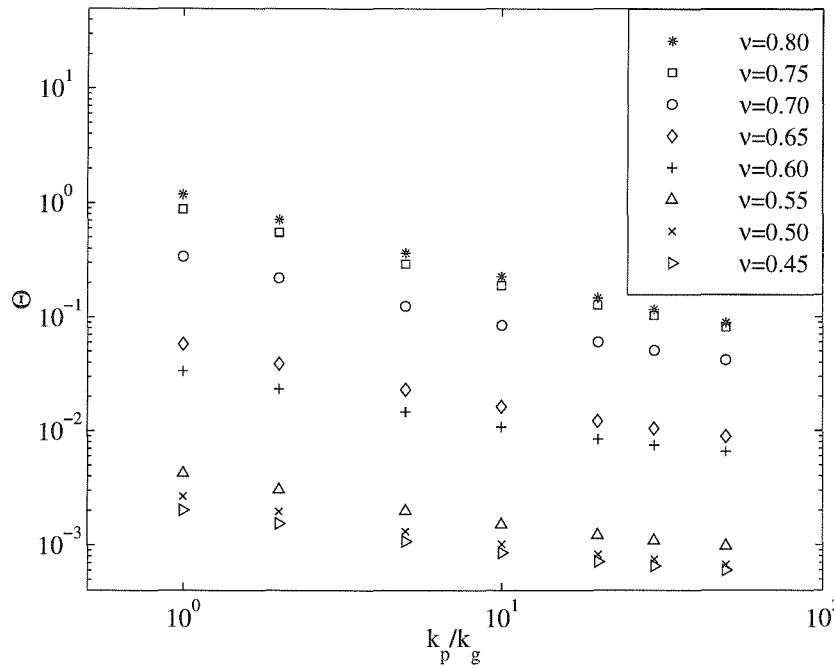


**Figure 3.15** Non-dimensional adiabatic wall temperature as a function of the conductivity ratio, $k_p/k_g$, for same-size flows of varying overall solid fractions.

gradients in heat flux and the curves are smooth.

Figure 3.15 presents the maximum temperature, which occurs at the adiabatic wall ($y = 0$), as a function of the conductivity ratio of particles to gas. The gas conductivity is constant while the conductivity ratio varies. The molecular conductivity term dominates in all the cases, so increasing the conductivity ratio increases the total conductivity. Higher conductivities decrease the maximum temperature obtained in the flow as the heat generated is conducted through the flow at a higher rate.

### 3.1.4 Kinetic theory solution

The constitutive laws of Jenkins and Richman [1985] for slightly rough and nearly elastic disks have been applied to the conservation equations to solve for the solid fraction, velocity, and granular temperature profiles in the flow. In the conservation

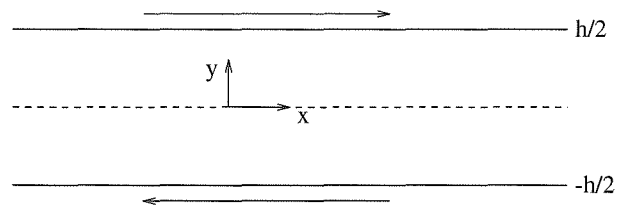


**Figure 3.16** Coordinate frame for application of conservation equations.

equations below, $\rho = \nu\rho_p$ is equal to the bulk density, $\vec{u}$ is the mean velocity, and $T$ is the translational granular temperature. The conservation of mass, momentum, and fluctuation energy equations for a two-dimensional flow are generally expressed below, following the similar analysis of Hanes et al. [1988]:

- Conservation of mass:

$$\frac{D\rho}{Dt} + \rho\nabla \cdot \vec{u} = 0, \tag{3.20}$$

  where $D()/Dt$ is the material, or total derivative.

- Conservation of linear momentum:

$$\rho\frac{D\vec{u}}{Dt} = -\nabla \cdot \mathbf{P} + \rho\vec{F}, \tag{3.21}$$

  where $\mathbf{P}$ is the total pressure tensor and $\vec{F}$ is the specific body force.

- Conservation of fluctuation energy:

$$\rho\frac{DT}{Dt} = -\nabla \cdot \vec{Q} - tr(\mathbf{P} \cdot \nabla\vec{u}) - \gamma, \tag{3.22}$$

  where $\vec{Q}$ is the fluctuation energy flux and $\gamma$ is the rate of dissipation in inelastic collisions (referred to earlier in this chapter as $\gamma_t$).

Several assumptions are now made. The definition of the geometry is given in figure 3.16. There are no body forces, and the flow is one-dimensional in the $x$ direction. Periodic boundaries in $x$ mean that there are no gradients in the flow direction. The flow is steady, so that there are no time derivatives either. The mean velocity in the transverse direction, $v$, is zero, and the mean velocity in the flow direction, $u$, is a function of $y$ only. In this special case, the conservation of mass is identically satisfied, and the two momentum equations give the result that the shear and normal stresses are constants, $S$ and $N$.

In the $x$-direction:

$$0 = \frac{dP_{xy}}{dy} \tag{3.23}$$

$$P_{xy} = \text{constant} \equiv S. \tag{3.24}$$

In the $y$-direction:

$$0 = -\frac{dP_{yy}}{dy} \tag{3.25}$$

$$P_{yy} = \text{constant} \equiv N. \tag{3.26}$$

The energy equation (3.22) reduces to:

$$\frac{dQ}{dy} - S\frac{du}{dy} + \gamma = 0, \tag{3.27}$$

where $Q \equiv Q_y$, as $Q_x$ is zero. The constitutive laws of Jenkins and Richman [1985] can now be substituted into the above simplified energy equation. First, the energy flux and shear stress are expressed in terms of the conductivity, $k$, and the viscosity,

$\mu$:

$$Q = k\frac{dT}{dy} \tag{3.28}$$

$$S = \mu\frac{du}{dy}. \tag{3.29}$$

Then, $\mu$, $k$, $N$, and $\gamma$ are expressed generally in terms of the translational granular temperature, $T$.

$$\mu = M\sqrt{T} \tag{3.30}$$

$$k = q\sqrt{T} \tag{3.31}$$

$$N = fT \tag{3.32}$$

$$\gamma = \xi T^{3/2} \tag{3.33}$$

where $M$, $q$, $f$, and $\xi$ are all functions of solid fraction $\nu$, which is in turn a function of $y$. Now,

$$T = N/f \tag{3.34}$$

$$\mu = \frac{M\sqrt{N}}{\sqrt{f}} \tag{3.35}$$

$$k = \frac{q\sqrt{N}}{\sqrt{f}} \tag{3.36}$$

The energy equation becomes a non-linear ordinary differential equation for the solid fraction $\nu(y)$ by substituting the above constitutive laws into equation 3.27.

$$\nu'' = \left(\lambda^2\frac{f^3}{Mqf'} - \frac{\xi f}{qf'}\right) - \left(\frac{f''}{f'} + \frac{q'}{q} - \frac{5}{2}\frac{f'}{f}\right)(\nu')^2, \tag{3.37}$$

where $\lambda = S/N$ is a constant, and $()'$ represents a first derivative with respect to $\nu$ except for $\nu'$, which is a derivative with respect to $y$. The definitions of the functions

$f$, $M$, $q$, and $\xi$ as functions of $\nu$ are as follows [Jenkins and Richman, 1985]:

$$\rho = \rho_p \nu \tag{3.38}$$

$$G = \nu g_0 \tag{3.39}$$

$$g_0 = \frac{16 - 7\nu}{16(1-\nu^2)} \tag{3.40}$$

$$f = \rho(1+2G) = \frac{4m\nu}{\pi d^2}(1+2G) \tag{3.41}$$

$$q = \frac{m\nu}{d\sqrt{\pi}}\left[\left(\frac{8}{\pi}+\frac{9}{2}\right)G + \frac{2}{G} + 6\right] \tag{3.42}$$

$$M = \frac{m\nu}{2d\sqrt{\pi}}\left[\left(\frac{8}{\pi}+1\right)G + \frac{1}{G} + 2\right] \tag{3.43}$$

$$\xi = \frac{16m\nu}{d^3\pi^{\frac{3}{2}}}G\left(\frac{\kappa(1+\beta)}{(1+\kappa)} + 2(1-e)\right) \tag{3.44}$$

$$\kappa = \frac{4I}{\pi d^2} \tag{3.45}$$

The assumption that the particle mass $m$ is equal to $\rho_p \pi d^2/4$ (for disks) is utilized in the above expression for $f(\nu)$. This assumption is appropriate for the theory, but in the simulations the mass is evaluated for spheres, not disks. In the above equations, $d$ is the particle diameter, $e$ the coefficient of restitution, and $\beta$ the roughness coefficient, discussed earlier in this chapter.

To solve equation 3.37, a value for the constant $\lambda = S/N$ must be specified from boundary conditions. To compare the results with the current simulations, the value of the stress ratio at the wall from the simulation has been used. Two boundary conditions in $\nu$ must also be specified:

$$\nu'(y=0) = 0 \tag{3.46}$$

$$\int_0^{h/2} \nu(y)dy = \overline{\nu}\left(\frac{h}{2}\right), \tag{3.47}$$

where $\overline{\nu}$ is the average solid fraction in the flow. To satisfy the second boundary condition, the value $\nu(y=0)$ is guessed and the numerical equation iterated until

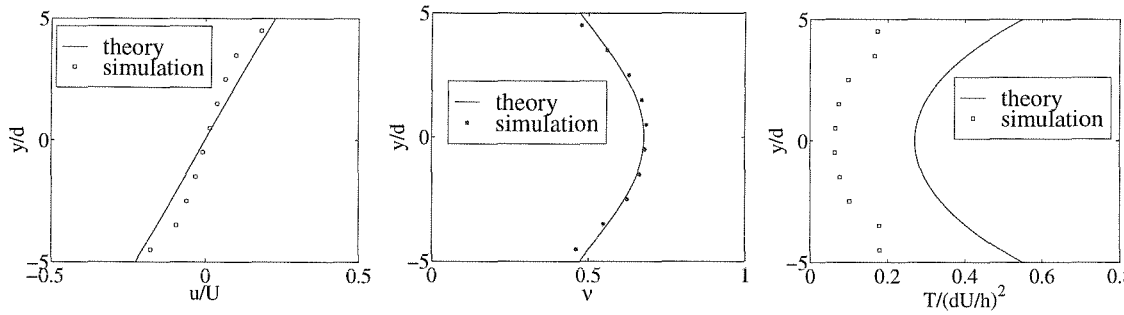


(a) Velocity (b) Solid fraction (c) Granular temperature

**Figure 3.17** Velocity, solid fraction, and granular temperature profiles for Couette flow with an average solid fraction of 0.6 and $h/d = 10$ and $\beta = 0$. Results from the computer simulations are compared with theoretical results.

the average solid fraction is correct within a tolerance of 1%. A 4th order Runge-Kutta scheme was used to solve for the solid fraction in the channel as a function of $y$. The velocity profile and granular temperature profiles can also be found from the expressions for the shear stress and the normal stress:

$$\frac{du}{dy} = \frac{S}{\mu} = \frac{S\sqrt{f}}{M\sqrt{N}} \tag{3.48}$$

$$T = N/f. \tag{3.49}$$

The boundary condition of $u(y = 0) = 0$, necessary for symmetry, was used to integrate the velocity gradient. The value of the stresses, $S$ and $N$, must be specified to use the above expressions. In this work, the values have been taken from the computer simulations.

Figures 3.17 and 3.18 show the theoretical results along with the results from computer simulations for an average solid fraction of 0.6 and gap widths of 10 and 20 particle diameters, respectively. Although the theoretical velocity profiles appear linear for these two cases, this is not the case in general. Theoretical predictions have

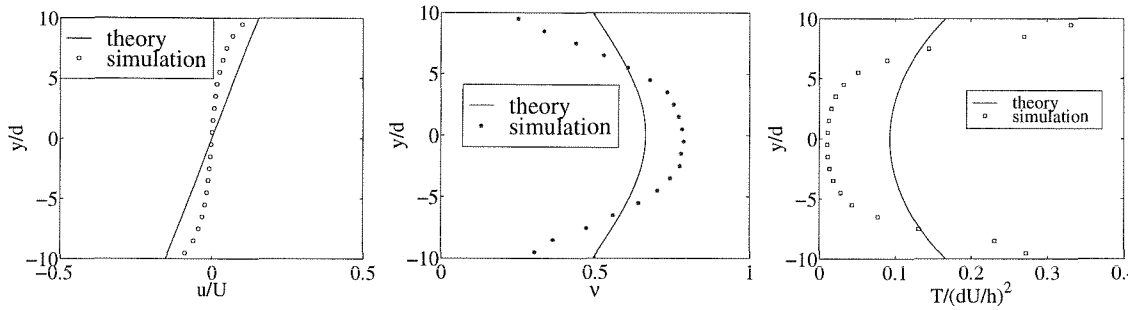


(a) Velocity (b) Solid fraction (c) Granular temperature

**Figure 3.18** Velocity, solid fraction, and granular temperature profiles for Couette flow with an average solid fraction of 0.6 and $h/d = 20$ and $\beta = 0$. Results from the computer simulations are compared with theoretical results.

the same general profile shapes, and in the case of $h/d = 10$, show good quantitative comparison with both velocities and solid fractions. In the case of $h/d = 20$ and for the temperature profile for $h/d = 10$, however, the agreement is not as good. The theoretical profiles generally have lower gradients in all three variables than the simulations. This is probably the reason that they match better for the narrower gap width, since for this width the gradients in temperature, velocity, and solid fraction are smaller than for the wider gaps. The theoretical results utilize the assumption that collisions are nearly elastic and nearly frictionless, which is not accurate for the current simulations; this is most probably the reason for the disagreement between the two.

## 3.2 Binary mixture flows

Computer simulations of gravity-free Couette flow have also been conducted with flows of particles of two different sizes. Unlike the flows of identical particles, the overall solid fraction is maintained constant ($\nu = 0.75$) for all the flows discussed in

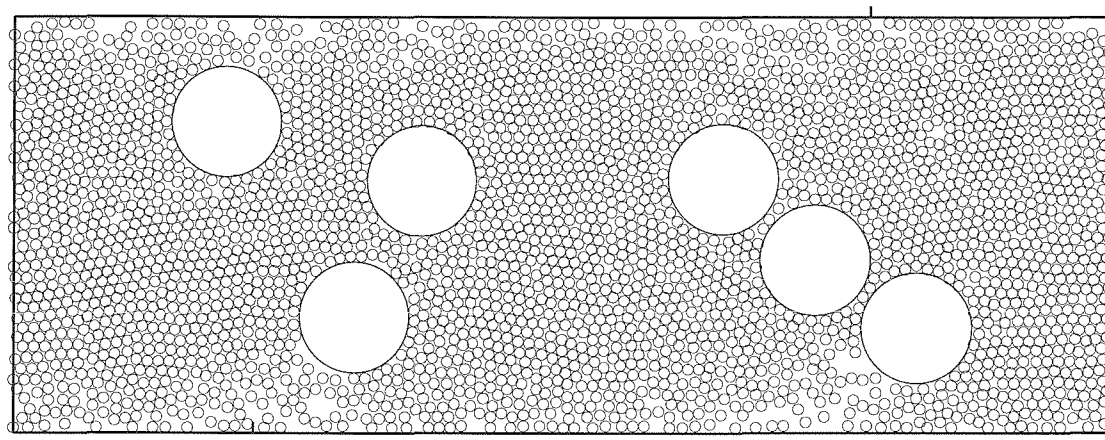

**Figure 3.19** Snapshot of simulation: $\phi = 10$ and $R = 5$.

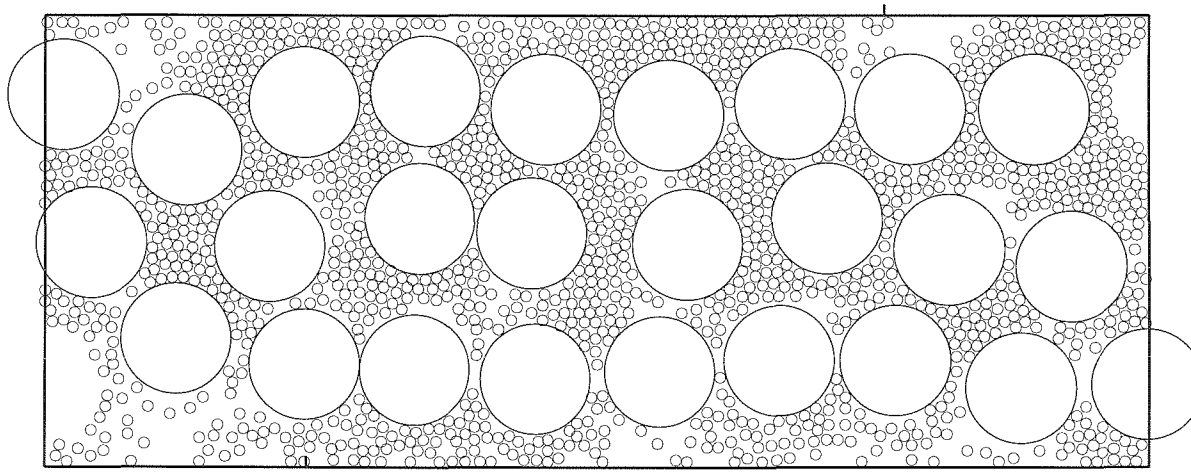

**Figure 3.20** Snapshot of simulation: $\phi = 10$ and $R = 0.5$.

this section. The gap width is also constant at $h/d_{small} = 40$ for all binary mixture flows. The ratio of solid fractions of small to large particles ($R$) and the size ratio of large to small particles ($\phi$) are varied to study their effect on the flow. The results obtained have been compared to the flows of monodisperse particles. Figure 3.19 shows a snapshot of a flow with a high value of $R = 5$ and $\phi = 10$. Figure 3.20 shows the same flow conditions with a much lower value of $R = 0.5$, illustrating the difference that the solid fraction ratio of small to large particles, $R$, makes in a flow with a given overall solid fraction.

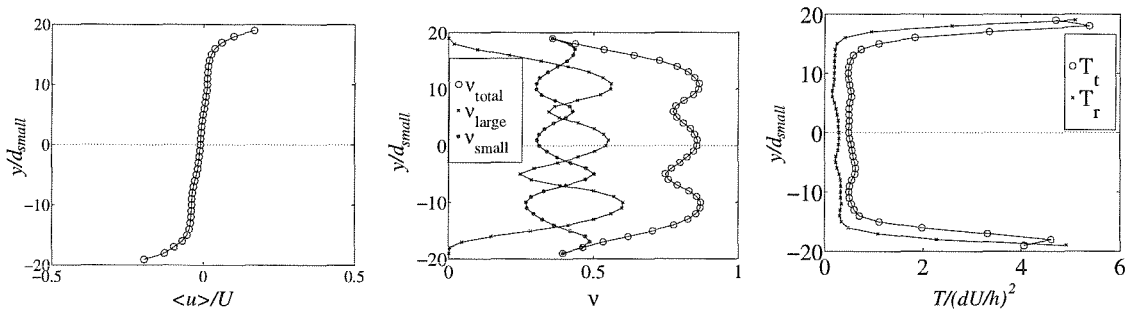


(a) Velocity (b) Solid fraction (c) Granular temperature

**Figure 3.21** Velocity, solid fraction, and granular temperature profiles for Couette flow of mixture with overall $\nu = 0.75$, $\phi = 10$, and $R = 1$.

### 3.2.1 Flow measurements

Figure 3.21 shows velocity, solid fraction, and granular temperature profiles for a binary mixture with a diameter ratio of 10. The solid fraction profiles for the large and small particles are shown separately along with the overall solid fraction. These profiles illustrate the high-shear zones nearest the walls, which correspond to low solid fractions and high granular temperatures. Solid fractions of both components decrease in the high-shear regions near the boundaries; solid fractions of large particles in flows with large diameter ratios (such as that shown in figure 3.21) are zero in those regions. The solid fraction profiles for this flow also illustrate the layering of large particles that often occurs in flows in which geometry constrains the positions of the large particles. In flows with relatively high solid fractions of large particles and diameter ratios of five or ten, the large particles are forced to form horizontal layers in the flow. This layering is discussed further in the mixing section of this chapter.

Slip velocities for mixture flows are presented in figure 3.22(a) as a function of solid fraction ratio for various diameter ratios. The slip velocity decreases with solid fraction ratio for all the flows, due to an increase in the effective solid fraction of small

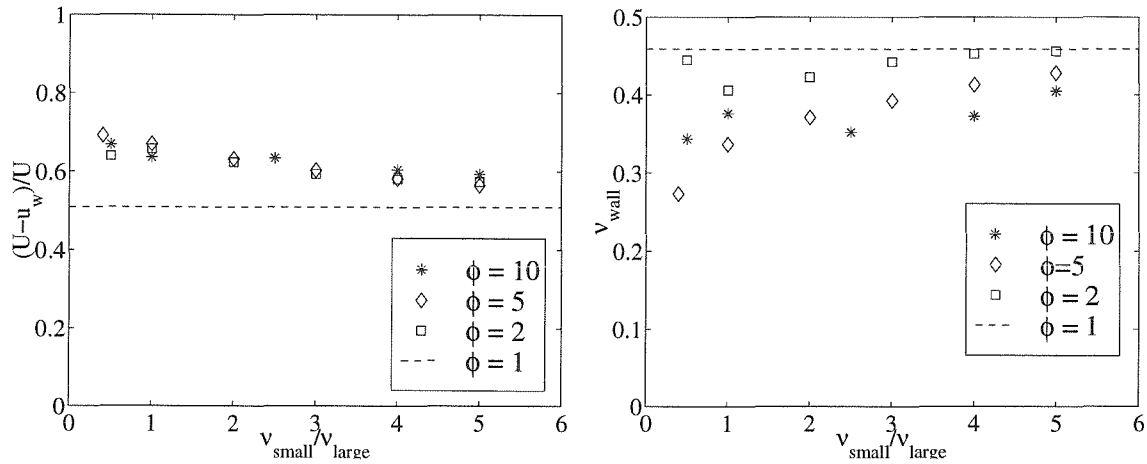


(a) Slip velocity.

(b) Solid fraction evaluated one particle radius from the wall.

**Figure 3.22** Slip velocity and the solid fraction at the wall as a function of solid fraction ratio of small to large particles in mixture flows. The dashed line represents the result for a monosized flow with the same overall solid fraction of 0.75 and the same $h/d$ of 40.

particles. When there are more small particles in the flow, the solid fraction at the wall is slightly higher, as shown in figure 3.22(b). The average granular temperature, shown in figure 3.23, decreases with solid fraction ratio.

When analyzing binary mixture flows using the kinetic theory of dense gases, previous researchers have used the assumption of the equipartition of energy between the species [Farrell *et al.*, 1986; Hsiau and Hunt, 1996]:

$$T_{t,large} m_{large} = T_{t,small} m_{small}. \tag{3.50}$$

The fluctuation kinetic energy is assumed to be constant for each species $i$ in order to relate the two species' translational granular temperatures $T_{t,i}$. To evaluate the accuracy of this assumption, the ratio of the two kinetic energies has been calculated and is shown in figure 3.24. The ratio is greater than one for all the size ratios in the

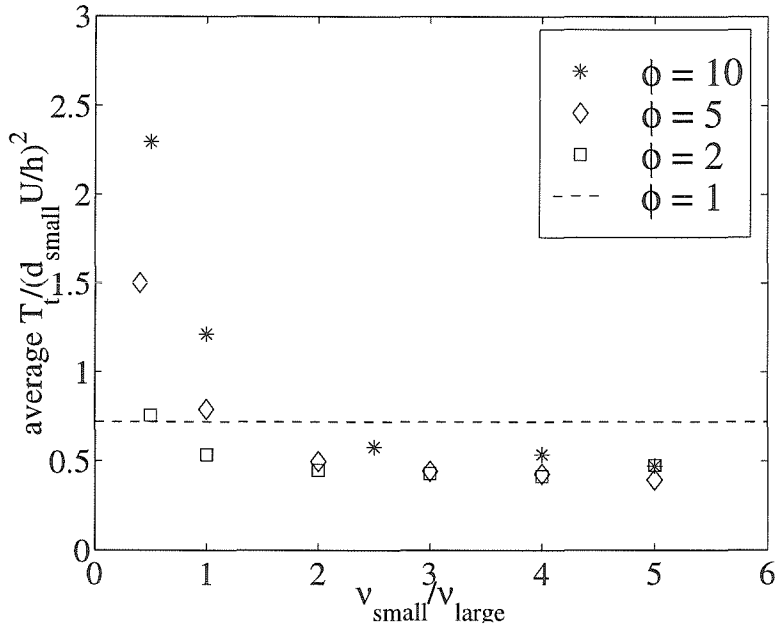


**Figure 3.23** Average translational granular temperature as a function of solid fraction ratio in mixtures for various size ratios.

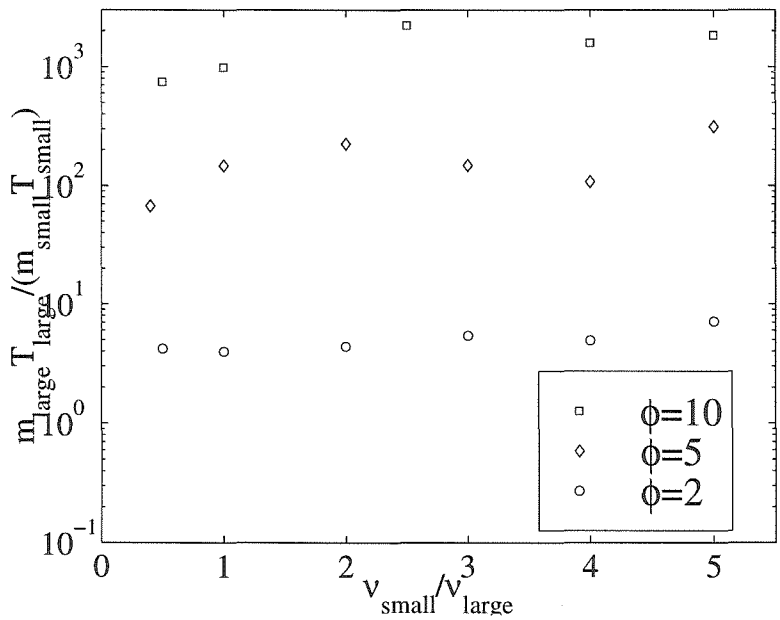


**Figure 3.24** Ratio of translational fluctuation kinetic energy of large particles to that of small particles, $T_{t,large}m_{large}/T_{t,small}m_{small}$.

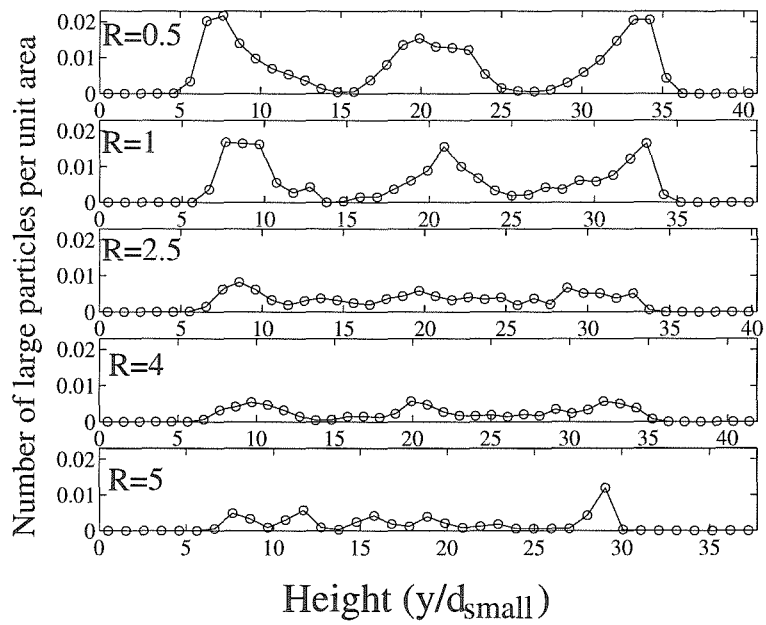


**Figure 3.25** Number of large particles per unit area at various solid fraction ratios, $R$: $\phi = 10$.

current study, illustrating the inaccuracy of the equipartition of energy assumption for these flows. It is, however, more accurate as the size ratio of the two species decreases.

### 3.2.2 Mixing

To illustrate the migration of large particles away from the wall regions for different solid fraction ratios, an analysis of the large particle positions was performed. Figures 3.25, 3.26, and 3.27 show the number of large particle centers per unit area as a function of height. Because the center of a particle cannot be closer than one radius from the wall, this region has a zero number density. The profiles for the size ratio of 10 (figure 3.25) show that as the solid fraction ratio $R = \nu_{small}/\nu_{large}$ increases, the low number density regions near the walls become wider due to the larger freedom

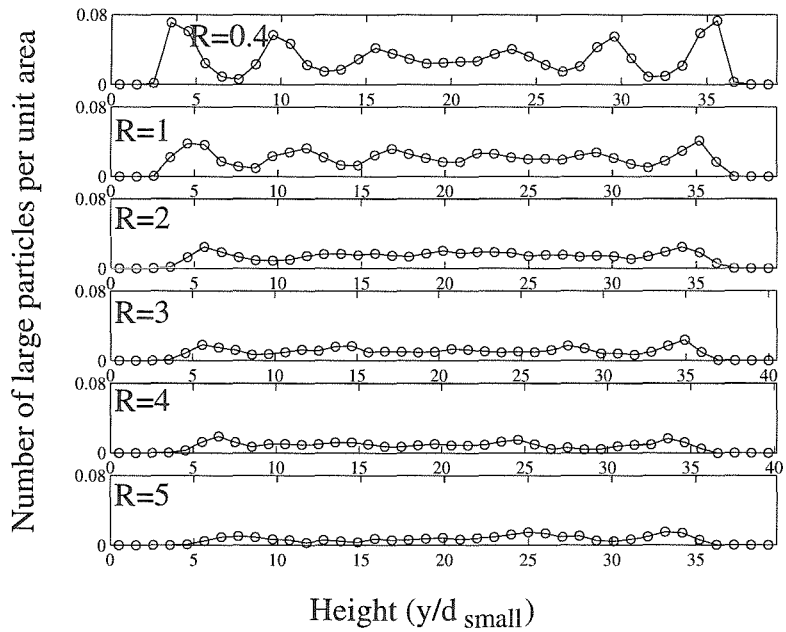


**Figure 3.26** Number of large particles per unit area: $\phi = 5$.

of motion of the few large particles. However, for low values of $R$, the motion of the large particles is constrained and they are forced towards the walls. The number density profiles of the large particles with $\phi = 5$ (figure 3.26) show a similar trend. For both $\phi = 10$ and $\phi = 5$, at high large-particle solid fractions (low values of $R$), the large particles form layers beginning at the solid boundaries. Figure 3.27 shows the same analysis for the simulations with a size ratio of only 2. This figure shows that the area near the wall with zero number density is only slightly wider than one radius; there is little migration of particles in these flows.

The snapshots of the mixture flows shown earlier in figures 3.19 and 3.20 illustrate the above behavior as well. Figure 3.19 (with the fewest large particles and highest value of $R$) shows that the large particles move freely in the central region of low shear, while avoiding the narrow regions nearest the walls. Figure 3.20 shows a flow with the lowest value of $R$; here, the large particles clearly form three distinct layers

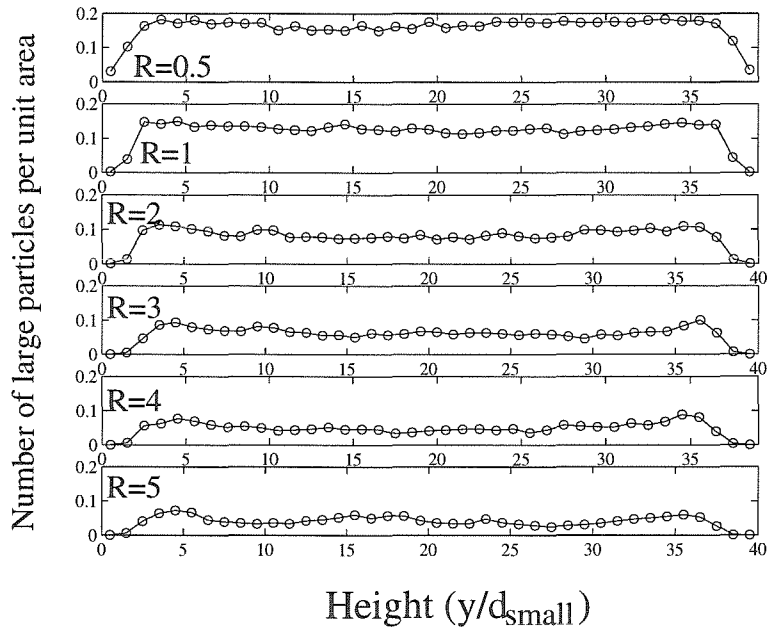


**Figure 3.27** Number of large particles per unit area: $\phi = 2$.

and are forced closer to the wall region.

### 3.2.3 Wall stresses

Figure 3.28 shows the stresses on the boundaries of a mixture flow as functions of time. The stress fluctuations are more uneven and larger in mixture flows than in mono-size flows (figure 3.6). Large spikes in the stresses usually indicate a collision of a large particle with the boundary or a squeezing of a small particle between a boundary and a large particle. The irregular occurrence of these events causes the larger fluctuations in the flows of mixtures. Average stresses in mixture flows are shown as functions of solid fraction ratio in figure 3.29. The solid fraction for all the flows is 0.75, and the stress level for the same-size flow at that solid fraction is shown as a dashed line for comparison. At low solid fraction ratios, both shear and normal stresses increase with diameter ratio $\phi$ and decrease with an increase in the solid

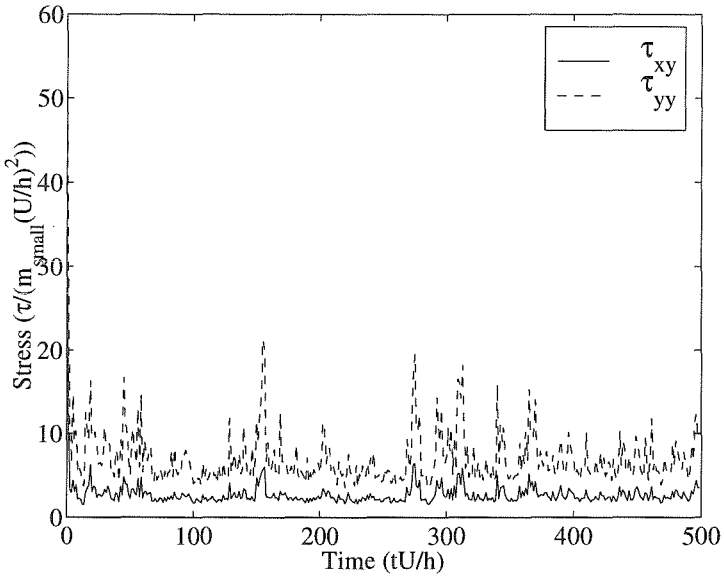


**Figure 3.28** Normal and shear stresses as functions of time for mixture flow with $\phi = 5$ and $R = 2$. The average stresses were found by taking the mean of the values after $tU/h = 60$.

fraction of small particles. The force exerted in a collision is proportional to the mass of the impacting particle; thus, larger particles increase the average stress. The stress also increases with the number of larger particles present in the flow; an increase in large particle number increases the likelihood of a collision of a large particle with the wall. At high solid fraction ratios the large particles do not generally collide with the walls, so that the stresses for simulations with few large particles are nearly identical to those for the same-size particle flow.

Figure 3.30 presents the wall stresses non-dimensionalized by the actual average strain rate, along with the value of the stresses predicted for a simple shear flow of smooth disks from Jenkins and Mancini's [1987] analysis. The theoretical expressions for the shear and normal stresses are derived using the constitutive laws of Jenkins and Mancini [1987] in the balance equation for the case of simple shear (constant granular temperature, solid fraction, and strain rate in the domain), just as was done for the same-size particles. The expressions have been simplified for a constant coefficient of

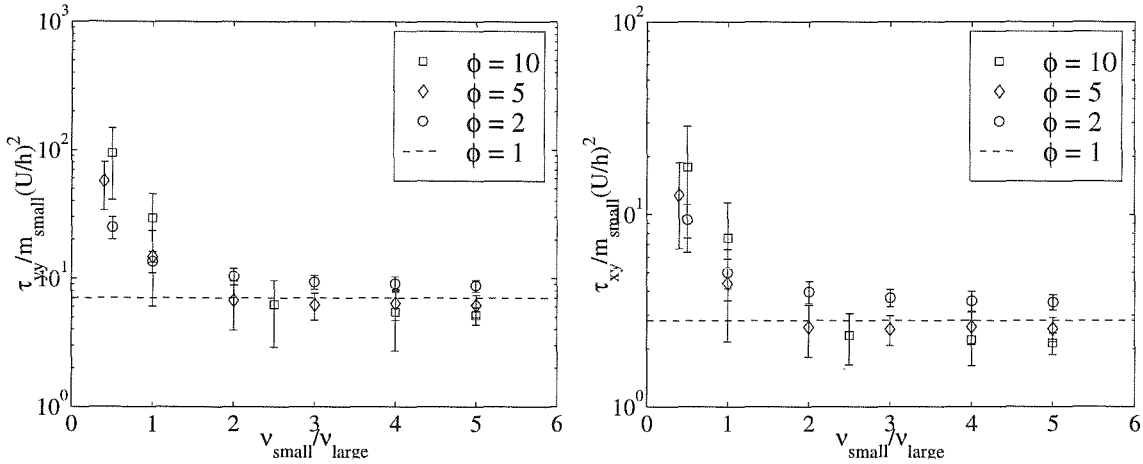


(a) Normal stress

(b) Shear stress

**Figure 3.29** Normal and shear stresses at the boundaries as functions of solid fraction ratio in mixtures, for various diameter ratios. The error bars show the standard deviation of the fluctuations in time. The dashed line corresponds with results for the mono-sized flow with the same overall solid fraction and $h/d = 40$.

restitution (which was the case in the simulations) and are shown below as functions of solid fraction ratio $R$ and size ratio $\phi$. The mass ratio has been assumed to be $\phi^2$, for disks, and small particles are denoted by $A$ and large by $B$.

$$\frac{\tau_{yy}}{m_A(du/dy)^2} = \frac{\left[\frac{\nu(R\phi^2+1)}{\pi\phi^2(R+1)} + K_{AA} + \frac{8K_{AB}}{(1+\phi)^2} + \frac{K_{BB}}{\phi^2}\right]\left[K_{AA} + \frac{4K_{AB}}{1+\phi}\left(\frac{2\phi^2}{1+\phi^2}\right)^{1/2} + K_{BB}\right]}{2(1-e)\left[K_{AA} + \frac{8\sqrt{2}K_{AB}}{(1+\phi)^3}\left(\frac{1+\phi^2}{\phi^2}\right)^{1/2} + \frac{K_{BB}}{\phi^4}\right]} \tag{3.51}$$

$$\frac{\tau_{xy}}{m_A(du/dy)^2} = \frac{\left[K_{AA} + \frac{4K_{AB}}{1+\phi}\left(\frac{2\phi^2}{1+\phi^2}\right)^{1/2} + K_{BB}\right]^{3/2}}{2\sqrt{\pi}(1-e)\left[K_{AA} + \frac{8\sqrt{2}K_{AB}}{(1+\phi)^3}\left(\frac{1+\phi^2}{\phi^2}\right)^{1/2} + \frac{K_{BB}}{\phi^4}\right]^{1/2}} \tag{3.52}$$

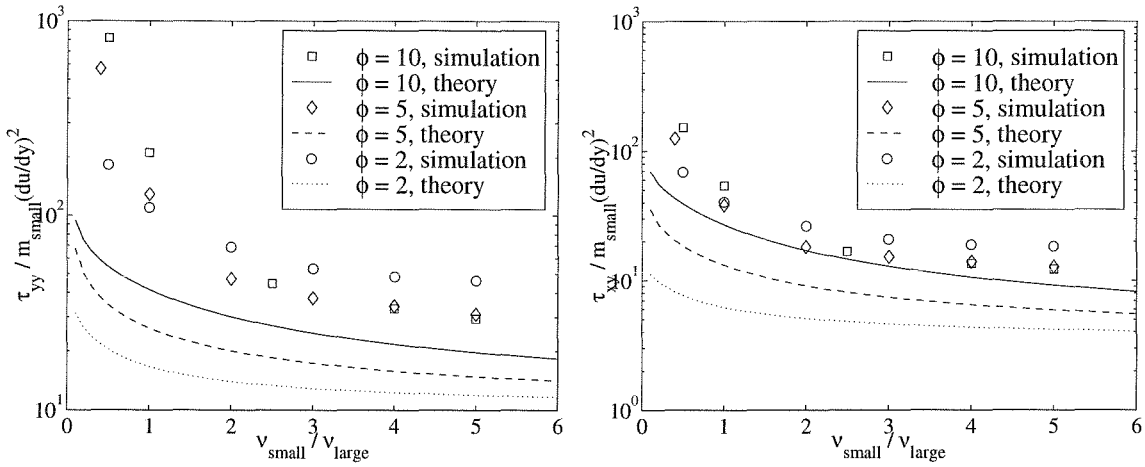


(a) Normal stress

(b) Shear stress

**Figure 3.30** Normal and shear stresses at the boundaries as functions of solid fraction ratio in mixtures, for various diameter ratios. The continuous lines show the kinetic theory predictions for a binary mixture of smooth disks in a simple shear flow [Jenkins and Mancini, 1987].

where

$$g_{AA} = \frac{1}{1-\nu} + \frac{9}{16}\frac{\nu(R\phi+1)}{\phi(1-\nu)^2(1+R)} \tag{3.53}$$

$$g_{BB} = \frac{1}{1-\nu} + \frac{9}{16}\frac{\nu(R\phi+1)}{(1-\nu)^2(1+R)} \tag{3.54}$$

$$g_{AB} = \frac{1}{1-\nu} + \frac{9}{8}\frac{\nu(R\phi+1)}{(1+\phi)(1-\nu)^2(1+R)} \tag{3.55}$$

$$K_{AA} = \frac{2}{\pi}\left(\frac{R}{R+1}\right)^2 \nu^2 g_{AA} \tag{3.56}$$

$$K_{BB} = \frac{2}{\pi}\left(\frac{1}{R+1}\right)^2 \nu^2 g_{BB} \tag{3.57}$$

$$K_{AB} = \frac{1}{8\pi}\frac{R(\phi+1)^4}{\phi^2(1+R)^2}\nu^2 g_{AB} \tag{3.58}$$

The theory captures the qualitative behavior but greatly under-predicts the simulation data. The most likely reason for this is that in the theoretical expression the

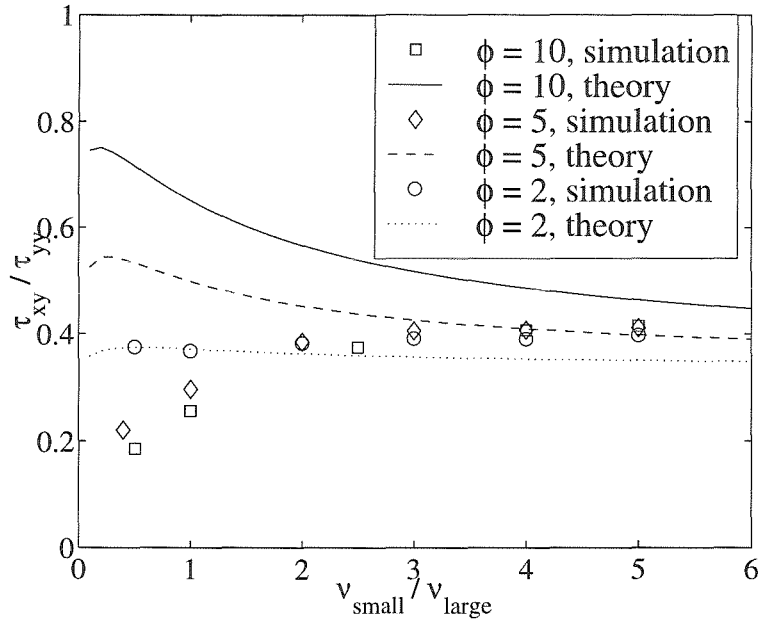


**Figure 3.31** Ratio of shear to normal stress at the boundaries as a function of solid fraction ratio in mixtures, for various size ratios. Predictions for a simple shear flow of smooth binary mixtures of disks [Jenkins and Mancini, 1987] are shown as well.

mass ratio of the particles is the square of the size ratio (for disks), while in the simulations the mass ratio is equal to the cube of the size ratio. The theoretical comparison also only applies for smooth particles, while the simulations use rough particles. Additionally, just as with the theoretical comparison for same-size flows, the theory applies to a simple shear flow with no gradients in temperature and a constant velocity gradient. The ratio of shear to normal stresses is also compared to the theoretical prediction in figure 3.31. Just as was the case for the flows of identical particles, the stress ratio is not predicted correctly in the theory because its behavior is dictated by the collision angle distribution, as will be explained in the next few paragraphs.

Figure 3.32 shows the ratio of shear to normal stress on the wall as a function of solid fraction ratio. For flows with $\phi = 2$ the stress ratio is roughly constant and close to that for same-size flows. Flows with diameter ratios of 5 and 10 exhibit low

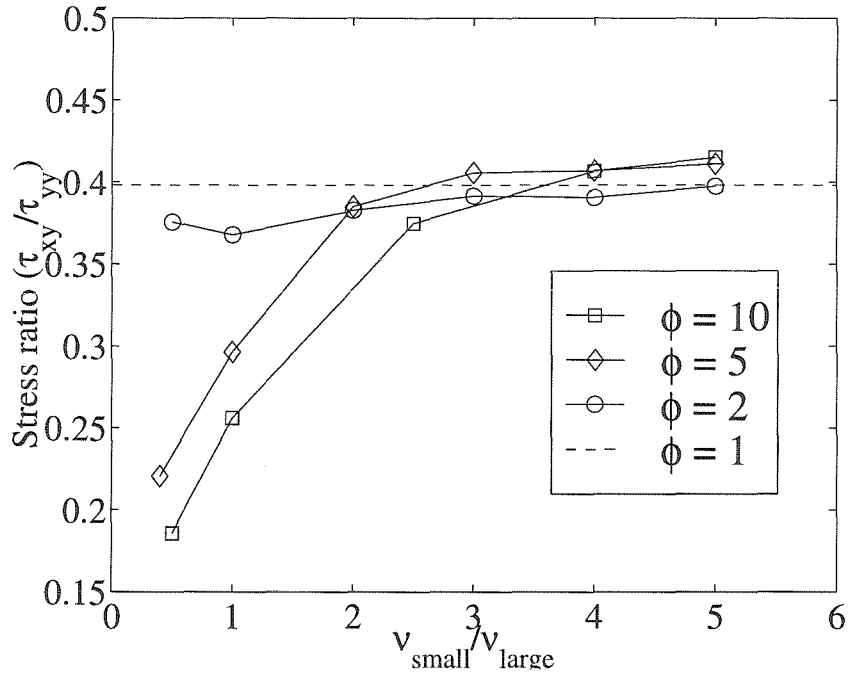


**Figure 3.32** Ratio of shear to normal stress at the boundaries as a function of solid fraction ratio in mixtures, for various size ratios. The value for the mono-size flow with the same overall solid fraction of 0.75 and $h/d = 40$ is shown as a dashed line.

shear to normal stress ratios at low solid fraction ratios of small to large particles. The explanation for the lower shear stresses in flows with many large particles and high size ratios lies in the angular distribution of particle-particle collisions.

One can define a collision angle distribution function $n(\theta)$ as the number of collisions occurring at a given $\Delta\theta$ divided by the total number of collisions. The collision angle, $\theta$, is defined in figure 3.33, and $\Delta\theta$ is the angular region used for averaging collisions in the simulation. In the current work the region from $-\pi/2$ to $\pi/2$ is divided into 15 regions, so that $\Delta\theta = \pi/15$.

Figure 3.34 shows the collision distribution for a mixture flow with a diameter ratio of 5 at two different solid fraction ratios of small to large particles. The distribution for the flow with a small solid fraction ratio is much flatter than that for the high solid fraction ratio. In any shear flow, the collision angle distribution is expected

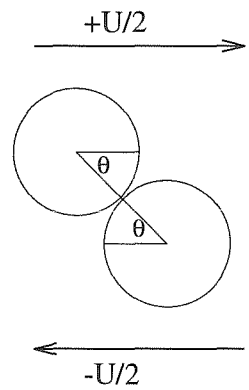


**Figure 3.33** Definition of collision angle, $\theta$, with respect to the relative motion of the upper and lower walls.

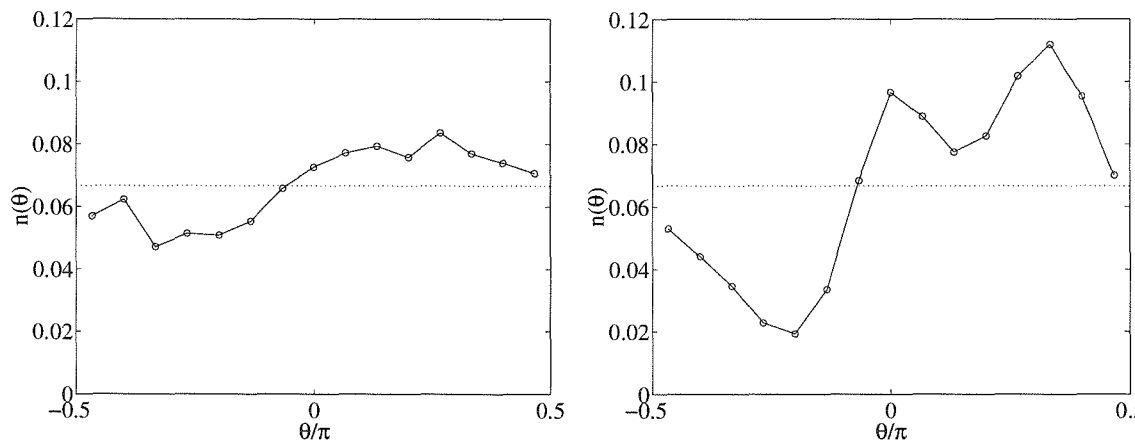


(a) $R = 0.4$ (b) $R = 5$

**Figure 3.34** Collision angle distribution functions for $\phi = 5$ at two different solid fraction ratios. The mean value of the function is shown as a dotted line.

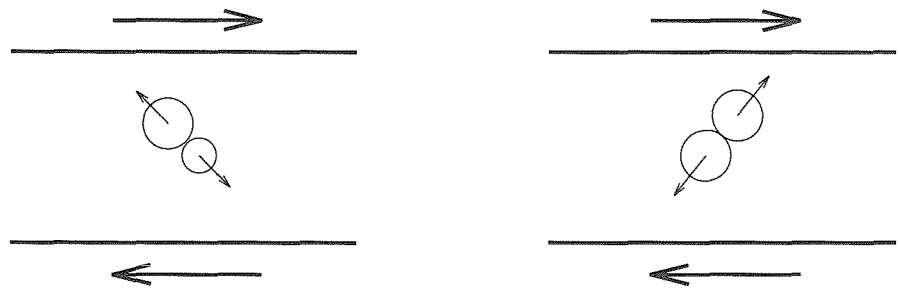


**Figure 3.35** Diagram of positive (a) and negative (b) collision angles. Arrows indicate trajectory after collision.

to be larger between 0 and $\pi/2$, corresponding to collisions occurring in the upper left and lower right quadrants of the particles [Campbell and Brennen, 1985]. The difference between the collision distribution function and its mean value quantifies the flatness or steepness of the distribution. The integral of this difference over the region of positive collision angles illustrates the extent to which collisions statistically occur in the positive $\theta$ region over the negative.

$$I_N = \sum_{\theta=0}^{\pi/2} (n(\theta) - n_{avg}) \tag{3.59}$$

Here the integral, $I_N$, is based on the summation of the difference between the value of $n(\theta)$ in each bin $\Delta\theta$ and the average. The average value, $n_{avg}$, is the value that corresponds to no preferential angle and an even collision distribution. The summation $I_N$ shows how frequently collisions occur at a positive angle.

Figure 3.35 shows two collisions with different collision angles. The collision on the left is occurring at $0 < \theta < \pi/2$ and contributing to a positive shear stress at the wall, due to a high relative tangential velocity with the wall after the collision. The collision on the right is occurring at $-\pi/2 < \theta < 0$ and will have a lower post-collisional relative tangential velocity with the wall, and therefore a small shear stress.

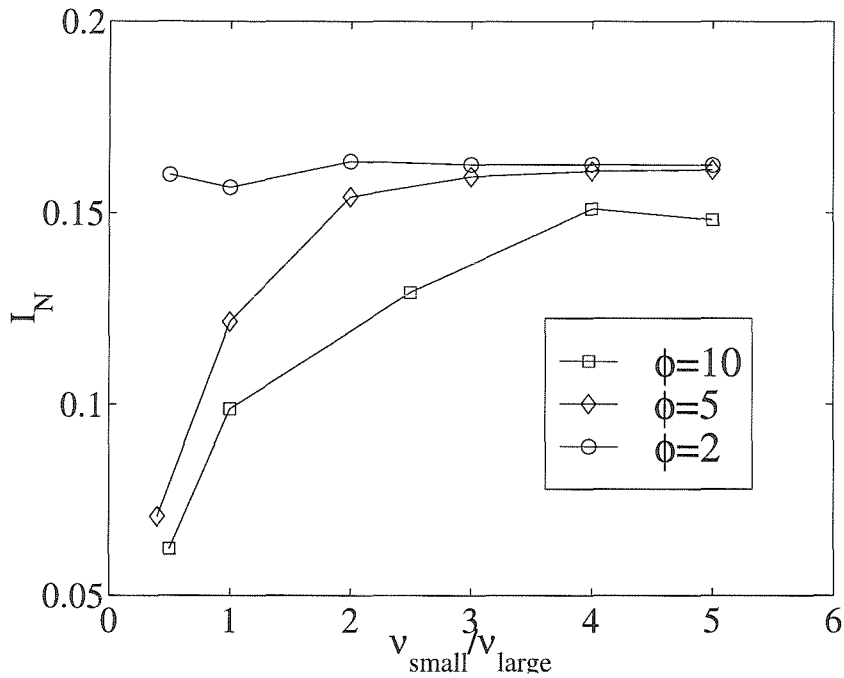


**Figure 3.36** Integral of positive half of the collision distribution function as a function of solid fraction ratio for various diameter ratios.

The normal stress at the wall is not affected by the wall collision angle.

Figure 3.36 shows that the collision distribution is much flatter for flows with size ratios of 5 or 10 and low solid fraction ratios of small to large particles. These flatter collision distribution functions result in smaller shear stresses, and therefore, lower shear to normal stress ratios in these flows. The flows with a diameter ratio of two do not exhibit a decrease in stress ratio or a flattening of the collision distribution function.

Flows with many large particles and high size ratios show a smaller velocity gradient in the center of the flow. In these flows with many large particles, the large particles inhibit the shearing of the small particles surrounding them, since the small particles are forced to move with the same velocity as the large particle. This small velocity gradient reduces the effect of the shear flow on the collision angle distribution. Particles in the central region of the flow behave as a plug without high relative

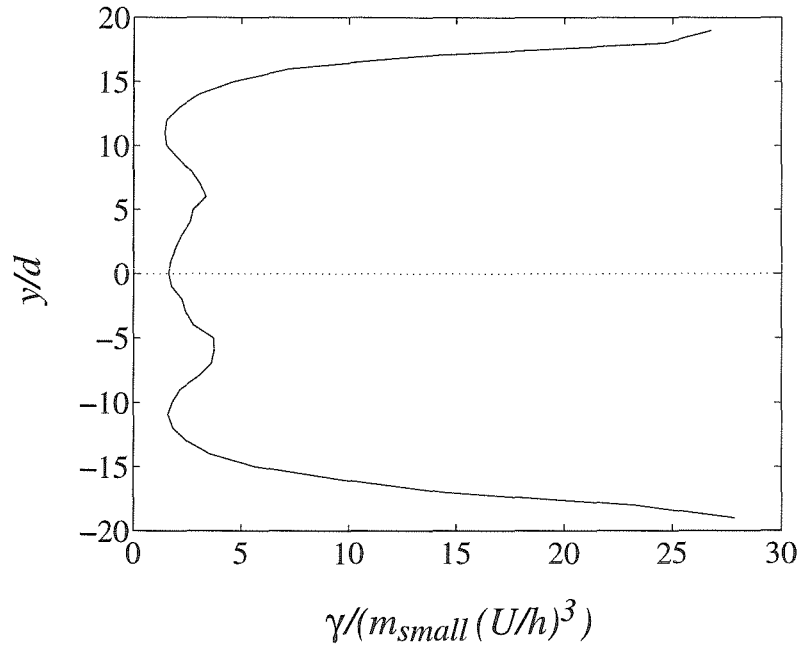


**Figure 3.37** Energy dissipation rate as a function of position for a Couette flow of a particle mixture. Overall $\nu = 0.75$, $\phi = 10$, and $R = 1$.

velocities; therefore, the distribution of collisions is more even than in flows with large velocity gradients. Flows with few large particles or with a size ratio of only two, however, have larger velocity gradients in the center region of the flow, leading to larger preferences in the collision distribution and higher stress ratios.

### 3.2.4 Energy dissipation and heat transfer

Energy dissipation calculations were conducted for the flows of binary mixtures in the same manner described in section 3.1.3 for flows of particles of the same size. Although kinetic theory derivations for binary flows do exist [Farrell *et al.*, 1986; Jenkins and Mancini, 1987; Jenkins and Mancini, 1989], all assume perfectly smooth particles and have not been applied to this flow.

Figure 3.37 shows results similar to those for same-size particle flows for the dissi-

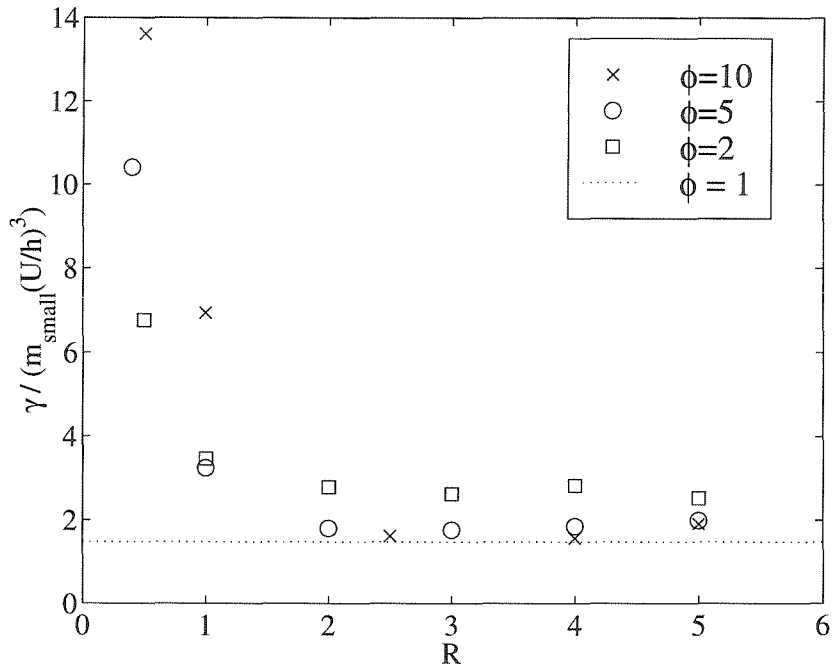


**Figure 3.38** Energy dissipation rate as a function of solid fraction ratio for Couette flow of mixtures. Overall $\nu = 0.75$.

pation rate as a function of vertical position in mixtures; dissipation increases in the high granular temperature and high strain rate regions near the walls. Figure 3.38 shows the dissipation rate as a function of solid fraction ratio, $R = \nu_{small}/\nu_{large}$, for various diameter ratios. This figure exhibits a trend of lower dissipation rates with higher solid fraction ratios. Thus, for a constant overall solid fraction, when there are more large particles in the flow, the dissipation is greater than when there are relatively few. The trend becomes more apparent at the larger diameter ratios. Collisions of large particles with small particles or with each other dissipate more energy than collisions between two small particles. This phenomenon is explained by the proportionality of the kinetic energy decrease to the mass of the colliding bodies if the coefficient of restitution is held constant, which it is in this case. The mass ratio of large to small particles is proportional to the cube of the diameter ratio, so the flows with larger diameter ratios show more dissipation. At the highest solid fraction

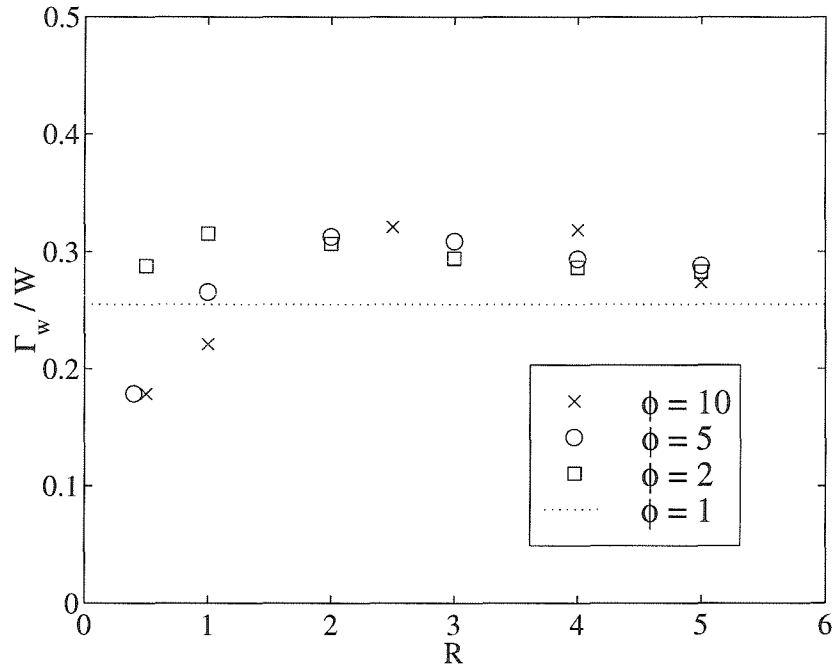


**Figure 3.39** Ratio of energy dissipation rate at wall to rate of work done by walls as a function of solid fraction ratio for mixture flows with overall $\nu = 0.75$.

ratio, for all three size ratios, the dissipation rate approaches the limit of that for the same-size flow with the same overall solid fraction, which is plotted as a dotted line. Figure 3.39 shows that the fraction of work dissipated in a mixture at the boundaries increases slightly with solid fraction ratio. The dotted line shows the value of this ratio for same-size flows with the same overall solid fraction. Only flows with many large particles exhibit a ratio lower than that for the mono-sized system. Figure 3.40 presents the rate of work done as a function of solid fraction ratio for binary mixtures, non-dimensionalized by the same quantity for a same-size flow. The results indicate that the work done by the walls in a mixture is generally higher than that done in a flow of single-size particles at the same solid fraction. At high diameter ratios and large numbers of large particles, the work done is almost 35 times that of the flow of one particle size at $\nu = 0.75$ and $h/d = 40$.

The energy equation used for same-size particle flows can also be applied here

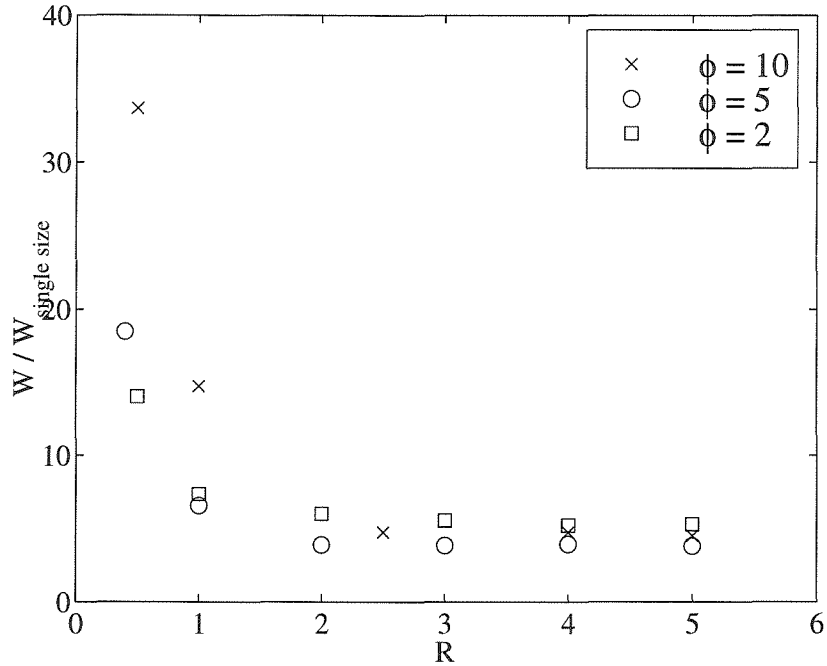


**Figure 3.40** Rate of work done by moving boundaries as a function of solid fraction ratio for mixture flows with overall $\nu = 0.75$. The work is normalized by the value of the work done in a flow with a diameter ratio of one and the same solid fraction.

for binary mixtures in the same form (equation 3.16). However, the kinetic theory-derived expression for the kinetic, or streaming, conductivity, $k_{kt}$, does not apply for mixture flows. In the same-size flow calculations, however, this streaming term only accounts for at most 3% of the total conductivity used in the calculation; the molecular conductivity, $k_{mc}$, is far larger at all solid fractions. Therefore, the analysis is followed in the same manner as in the same-size flows, with the exception of neglecting the contribution of the streaming conductivity, $k_{kt}$, so that $k_{tot} = k_{mc}$. The resulting adiabatic wall temperature, $\Theta = (\mathcal{T} - \mathcal{T}_0)/(U^2/c_p)$, is shown in figure 3.41 as a function of solid fraction ratio for various size ratios. The temperature follows the same trend as the dissipation rate in these flows; flows with many large particles dissipate more energy, resulting in a higher thermodynamic temperature.

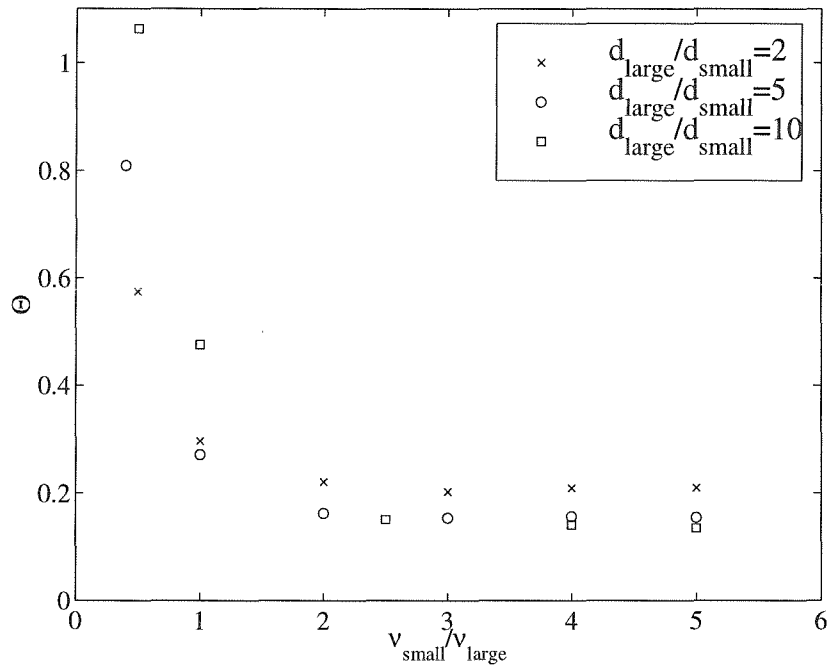


**Figure 3.41** Non-dimensional adiabatic wall temperature as a function of solid fraction ratio for various diameter ratios in mixture flows, for $k_p/k_g = 23$.

### 3.2.5 Simulations including electrostatic charge effects

In many granular flows of small particles and powders, other inter-particle surface forces become extremely important to the flow dynamics. In an effort to model the effect of one common force that is found in many industrial flows, electrostatic charging between particles has been added to the discrete element simulations. The purpose of these specific simulations is to understand shear flows of carrier particles and toner particles in high-speed photocopiers and laser printers. Carrier particles are often five to ten times larger than toner particles and are used to ease the handling of the small toner particles. While being mixed with carrier particles, toner particles accumulate an opposite charge to that of the carriers, allowing them to be attracted to the larger carrier beads.

To model this interaction, binary mixture simulations were conducted in the same

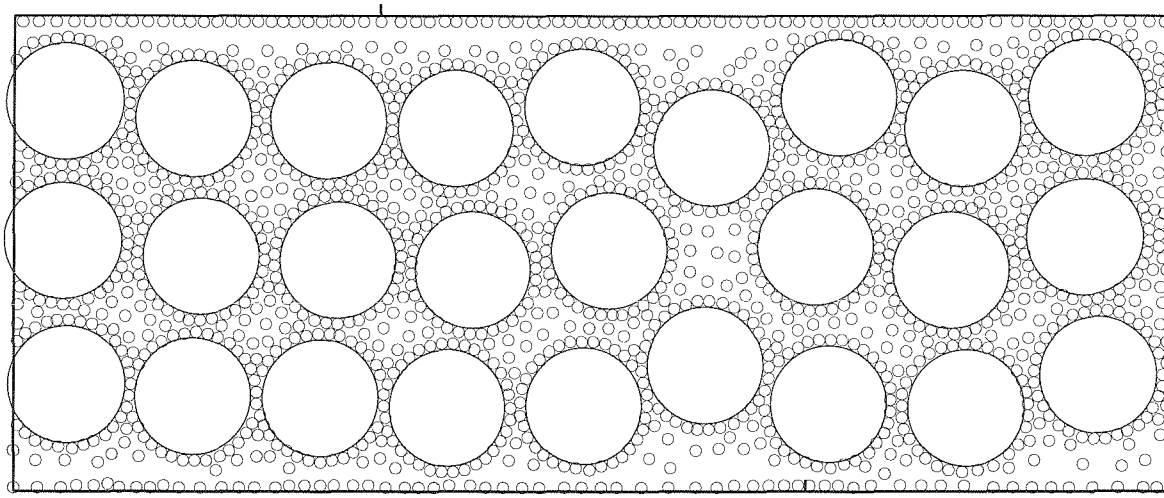

**Figure 3.42** Snapshot of flow for a simulation with electrostatic charge and $\phi = 10$, $R = 0.5$, $h/d_{small} = 40$, and overall $\nu = 0.75$.

plane geometry as those described earlier without charge (that is, $\nu = 0.75$ and $h/d_{small} = 40$), with the only difference being the addition of a point charge at each particle's center. The large and small particles are oppositely charged so that the net charge in the domain is zero. Thus, the relative magnitude of the charges depends on the solid fraction ratio of the two species. The charge placed in each small particle is $6.7 \times 10^{-16}$ Coulombs. This value is one-tenth of that of an average toner particle [Eklund *et al.*, 1994], and was chosen so that it would be large enough to attract particles to each other but small enough to avoid large overlapping of the simulation particles.

Figures 3.42 and 3.43 are snapshots of flows with charged particles at two different solid fraction ratios. The small particles form layers around each of the large particles as well as a layer against the solid boundaries. Although the boundaries are uncharged, the small particles are repelled from the other small particles with like charge in the flow and adhere to the walls. The normal force against the walls is large enough for the layer of small particles to travel at the same speed as the moving wall. The number of layers around each large particle increases with the solid fraction ratio,

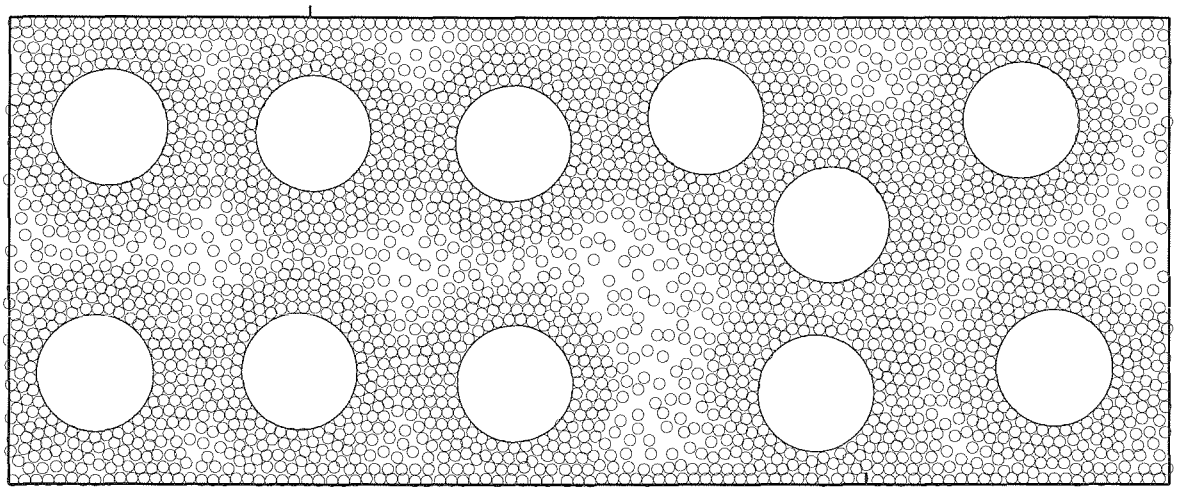

**Figure 3.43** Snapshot of flow for a simulation with electrostatic charge and $\phi = 10$, $R = 2.5$, $h/d_{small} = 40$, and overall $\nu = 0.75$.

because as the number of large particles decreases, the charge on each large particle increases to maintain a net charge of zero in the flow. As the charge on each large particle increases, the force between large and small particles also increases, allowing more layers of small particles to be attracted to a single large particle.

Figure 3.44 shows the velocity, solid fraction, and granular temperature profiles of simulation shown in figure 3.42. The velocity profile shows that the mean velocity in the flow is zero and only the particle layer against the wall is moving at the speed of the wall. The rest of the particles are not shearing and do not feel the effect of the walls. The solid fraction profiles in figure 3.44(b) show that the large particles in this flow form three distinct layers. The small particle solid fraction shows a large jump nearest the boundaries (at $y/d_{small} = -20$ and 20), corresponding to the layers against the wall observable in the snapshot in figure 3.42.

Simulations with charge were run for one diameter ratio, $\phi = 10$, and three solid fraction ratios, $R = 0.5$, 1, and 2.5. Wall stresses were measured just as in the uncharged mixtures, and the results are presented in figure 3.45 along with the results of the uncharged simulations (repeated from figure 3.29). Simulations with charge show that the wall stresses increase significantly as a function of the solid fraction

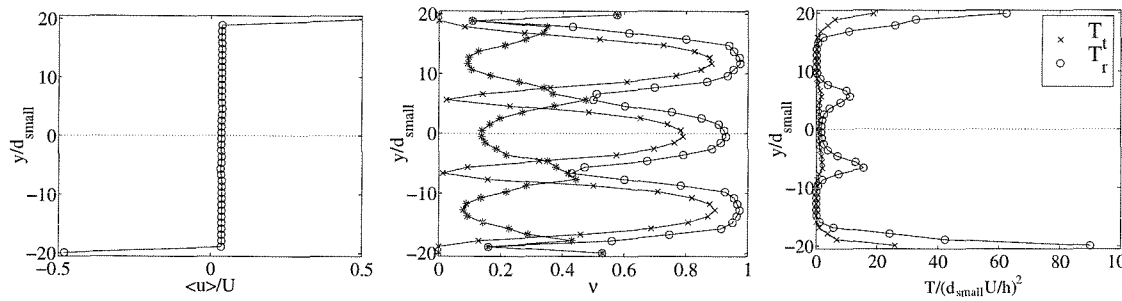


(a) Velocity

(b) Solid fraction ($\circ$ = $\nu_{total}$, $\times$ = $\nu_{large}$, and $\star$ = $\nu_{small}$).

(c) Granular temperature

**Figure 3.44** Velocity, solid fraction, and granular temperature profiles for Couette flow of mixture with charge and overall $\nu = 0.75$, $\phi = 10$, and $R = 0.5$.

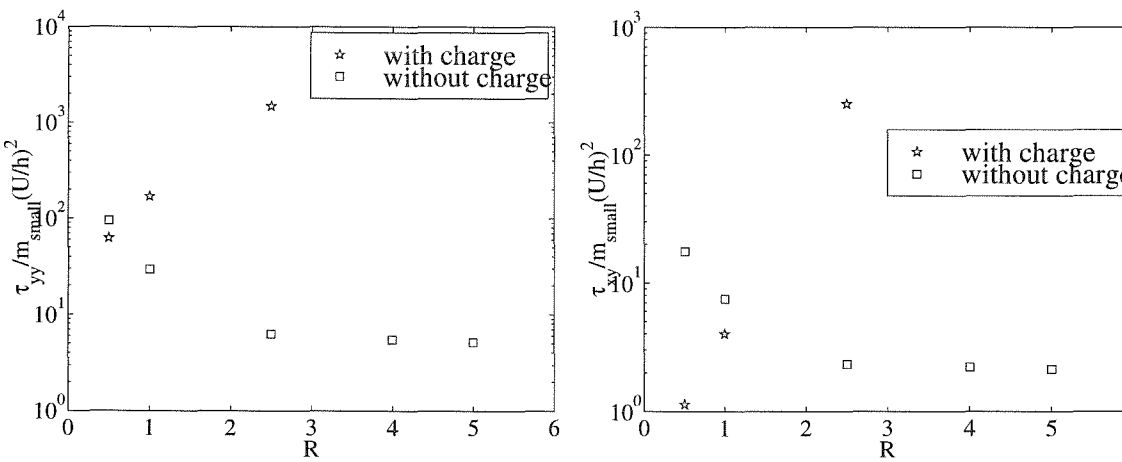


(a) Normal stress

(b) Shear stress

**Figure 3.45** Normal and shear stresses at the boundaries as functions of solid fraction ratio in mixtures with diameter ratio of 10 with and without electrostatic charge.

ratio of small to large particles, $R$. This behavior differs from that of the uncharged system, whose wall stresses decrease with solid fraction ratio. The increased stresses in the charged simulations are caused by the additional layers of small particles against the wall, as well as the closer proximity of the large particles to the walls, as seen in figure 3.43.

The simulations performed with electrostatic charge illustrate the usefulness of the discrete element method for modeling flows with complex interaction forces. The geometry of these specific simulations was not ideal because when charge was added, the particles hovered in the channel, with minimal wall contact. There was almost no velocity gradient in the channel and no flow resulted. Future simulations for modeling of charged flows should include gravity as well, forcing the particles to contact their boundaries and be sheared. Qualitatively, however, the simulated flow resembles flows of toner and carrier particles, in that the large carrier particles become surrounded with smaller particles adhering to them due to the charge attraction. The simulation behavior confirms that discrete element simulations can be used to model flows with electrostatic charging, and at least qualitative similarity can be achieved even with the extremely simple model implemented here.

# Chapter 4

# Experiment

A cylindrical Couette flow apparatus has been devised to perform experiments on granular shear flows. Both flows of particles of the same size as well as flows of mixtures of two different particle sizes are studied experimentally. Several different kinds of measurements are made in the apparatus, including shear stress measurements and velocity measurements. In this chapter, the experimental instrumentation, measurement methods, and apparatus are described.

## 4.1 Apparatus

The experimental apparatus illustrated in figure 4.1 consists of two concentric aluminum cylinders whose surfaces are coated with grade 40 (3M extra coarse) sandpaper. The inner cylinder is attached to a shaft that is rotated by a motor, while the outer cylinder remains stationary. Spherical glass beads with diameters of 3, 4, 6, or 8 mm are sheared between the inner rotating cylinder and the outer stationary cylinder.

Figure 4.1 illustrates the experiment in its horizontal orientation, with the shaft perpendicular to gravity. The entire apparatus can also be rotated ninety degrees so that the cylinder is oriented vertically, parallel to the direction of gravity. The outer cylinder has an inner diameter of $20 \pm 0.1$ cm. Three inner cylinders with varying

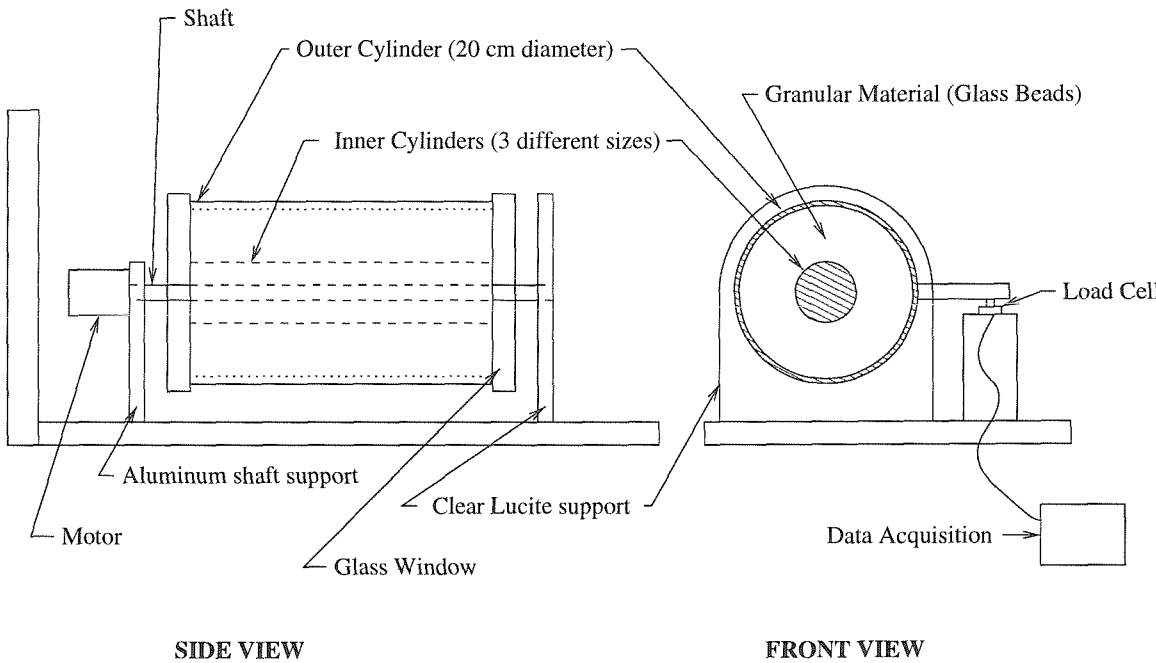


**Figure 4.1** Experimental apparatus.

diameters (8, 12, and 14±0.1 cm) have been constructed and are interchangeable, allowing the width of the gap between the cylinders to vary between 6, 4, and 3 cm. The length of the cylinders is 31.75±0.5 cm. The glass window and clear 'lucite support on one end of the cylinders allows for visual observation of the flow within the apparatus. High-speed video can be taken through this window in order to digitally track the particles inside. Figure 4.2 is a photograph of the apparatus.

Table 4.1 catalogs the equipment used for the experiment. The DC motor driving the inner cylinder was able to run at variable speeds up to 46 RPM (4.8 radians/second), with a maximum torque of 37 N-m (330 in-lbs) and a gear ratio of 41.2:1. An optical encoder attached to the motor determined the exact rotational speed of the inner cylinder. The rotational speed was displayed digitally as the experiment ran so that the rotation rate of the inner cylinder could be set with an accuracy of ±0.01 rad/s at any time.

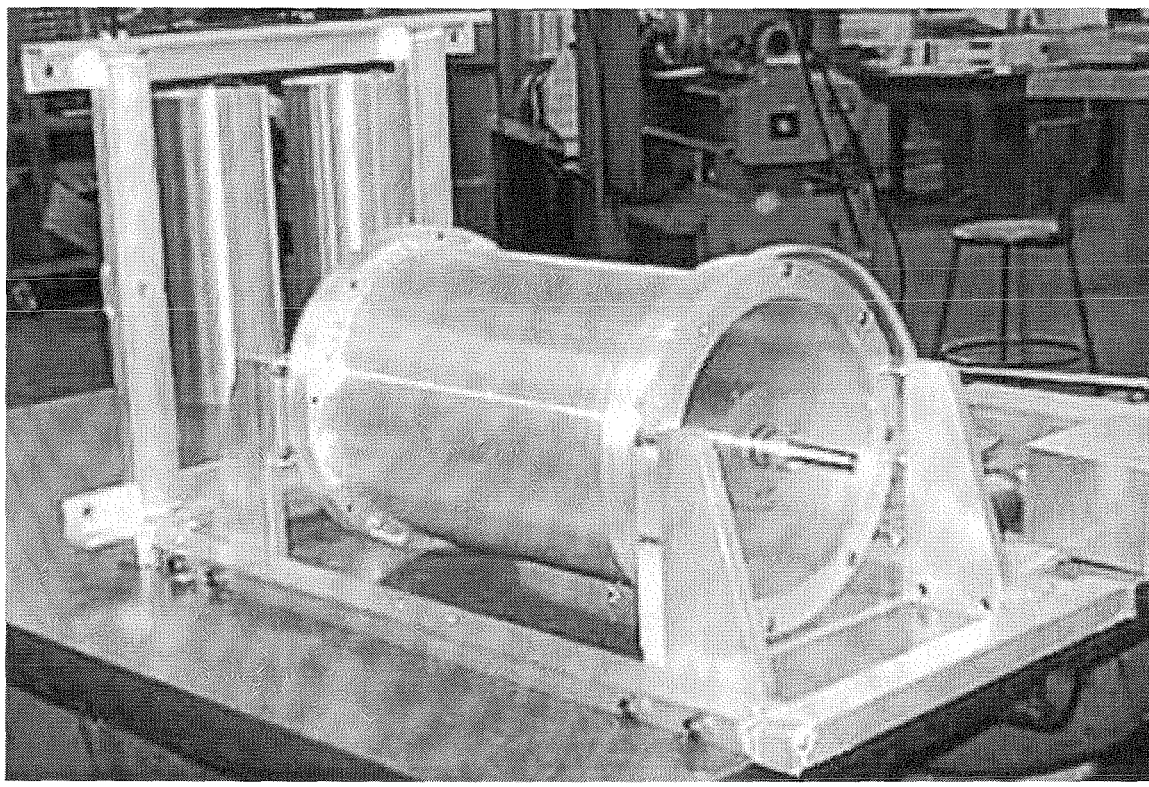

**Figure 4.2** Photograph of horizontally oriented experimental apparatus with the smallest of the three inner cylinders. The other two cylinders can be seen in the background, standing vertically.

## 4.2 Measurement techniques

Various experimental measurements, including shear stress, particle velocities, and mass fraction were made using the apparatus and equipment described above.

### 4.2.1 Shear stress on outer cylinder

One of the initial goals of the experimental work was to measure the shear stress on the cylinders as a function of various parameters, including rotational speed, particle size, and fill level. The shear stress on the outer cylinder was measured in the following manner. The outer cylinder is decoupled from the inner cylinder and free to rotate separately. It has an aluminum arm attached to one side that rests on a load cell

| Equipment | Manufacturer | Model | Specifications |
|---|---|---|---|
| 90V DC GearMotor | Bison | 011-348-7041 | $\frac{1}{4}$HP, 37 N-m torque |
| Variable-speed drive | Minarik | MM23001C | |
| Optical encoder | Minarik | PK21-30-5V | 30 pulses per rev. |
| Rate indicator | Red Lion | CUB50000 | Counter and display for encoder output |
| Power supply | Red Lion | APS | For CUB5 & PK21 |
| Load cell | Sensotec | 13 | max. load: 25 lbs. |
| Universal inline transducer amplifier | Sensotec | 008-0295-00 | For load cell |
| Data acquisition card | RC Electronics | | 1MHz samp. rate |
| High-speed video camera | RedLake | | 500 f/s |
| Imaging board | EPIX | PIXCI-SV3 | Rev. 3.0 |
| Imaging PC software | EPIX | XCIP | |

**Table 4.1** List of equipment used in experiments.

when the experiment is running. The load cell measures the force necessary to keep the outer cylinder from rotating when there is a granular material between the two cylinders. Because the total torque is constant, and independent of the radial distance at which it is measured, this force measurement can be used to calculate the torque on the system. The torque is then used to calculate the shear stress, or the tangential force per unit area on the outer cylinder. Specifically,

$$Torque = (F_{measured})(R_{load\ cell}) = (F_{outer\ cylinder})(R_{outer}) \tag{4.1}$$

$$\tau_{r\theta,\,outer} = \frac{F_{outer}}{Surface\ Area} = \frac{(F_{measured})(R_{load\ cell})}{(R_{outer})(Surface\ Area)}, \tag{4.2}$$

where the torque is equal to the force measured on the load cell ($F_{measured}$) multiplied by the radial distance between the center of the cylinders and the load cell ($R_{load\ cell}$). $F_{outer}$ is the corresponding force on the inner surface of the outer cylinder, and $R_{outer}$ is the radial distance from the cylinder center to the inner surface of the outer cylinder. The appropriate surface area is the portion of the outer cylinder area that is covered by beads. This is equal to $2\pi R_{outer}L$ when the cylinder is in the vertical orientation,

where $L$ is the fill level of the beads in the cylinder. The shear stress on the outer cylinder is represented as $\tau_{r\theta,outer}$. The contribution to the torque of the shear stress on the aluminum base of the outer cylinder is neglected in this analysis. The base area is significantly smaller than that of the barrel, especially at large fill heights, and the coefficient of friction of the glass beads on aluminum is presumed to be very low.

The load cell signal was amplified using the Universal In-Line Amplifier (see table 4.1) so that the output signal ranged between zero and five volts. The output voltage was read by one channel on the RC Electronics data acquisition card. The resolution of the data acquisition was $\pm$ 5 mV, which translates to $\pm$ 0.11 N in the force. The load cell and amplifier system was calibrated using a shunt calibration according to the manufacturer's instructions. To verify this calibration, tests were done by placing known weights on the load cell and determining the output signal. This method was much less accurate than the shunt calibration because it was difficult to place the large weights on the small surface of the load cell, and was only used to confirm the calibration.

The amplified signal from the load cell was read by a data acquisition system run on a PC with an Intel 386 processor. The sampling period used for the majority of measurements was either 1 or 2 ms. This high sampling rate was used to capture the large fluctuations in the stress measurements accurately, with 5 to 10 samples per period of the highest frequency fluctuations. Samples were taken continuously for 32 seconds, and the resulting signal was averaged over this period. Before each set of runs, the load cell was allowed to warm up for at least 10 minutes and the outgoing signal was zeroed by adjusting the amplifier. Data was acquired for 32 seconds at this approximate zero. The average of this signal (usually less than 5 mV) was then subtracted from the subsequent set of data. Data acquisition began after the experiment was running at the desired rotation rate for at least three rotations.

### 4.2.2 High-speed imaging analysis

High-speed video of the flow was taken through the glass window at the front of the experiment. A high-speed digital black and white video camera was used at a framing rate of either 125 or 250 frames per second. High-speed video was digitized using an EPIX digitizing card in a Pentium Pro 200 MHz PC running the Windows NT operating system. A commercial software package provided by the card manufacturer was used with the card to digitize video images. A particle tracking algorithm provided with the software was used to track features (usually light reflected off individual glass beads) of the flow from one frame to the next.

To determine the particle angular velocity as a function of radial position, video was taken of one section of the front of the cylinder, for example, of a square region at the very bottom covering an angular arc of perhaps 20 degrees. Great care was taken to ensure that the light source was sufficiently far from the front of the apparatus and oriented in such a way that each light reflection spot traveled with its corresponding particle. After being digitized, the contrast of the image was enhanced so that all pixels above a particular gray level became white, and the others black. This threshold level was different for each video and depended on the lighting of a particular experimental run. The image was converted to a series of white spots on a field of black, each corresponding to the light reflection off a particle surface. The computer program then tracked each spot from one frame to the next, marking its position in each of the two frames. The framing rate of the video was chosen so that each particle moved a fraction of one particle diameter in one frame, and the analysis could be performed on each particle without confusing the locations of two separate particles. A program was written to repeat this process over a sequence of several hundred frames. The $(x, y)$ location of the center of each light reflection at each of two consecutive frames was converted into a location in $(R, \theta)$ coordinates. The velocity of each particle in the $R$ and $\theta$ directions was then determined as a function of radial location, $R$.

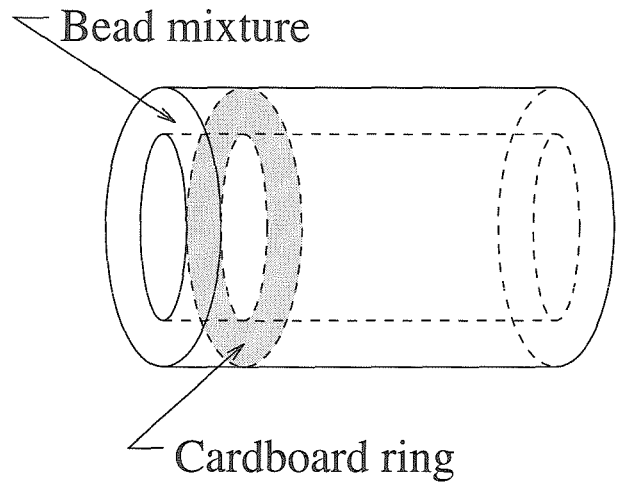


**Figure 4.3** Diagram illustrating placement of cardboard bottom in the experiment to shorten the length. The dyed bead mixture was placed in the front region near the glass window.

In the flow of a mixture of particles of two different sizes, it was necessary to make measurements of each type of particle separately. To accomplish this, the smaller particles were first dyed black. High-speed video was taken of the experiment running, but only the reflections off of the undyed larger particles were tracked by the software. Velocity measurements were made using the procedure outlined above. In addition to determining particle velocities, the same data could be analyzed to find the number of large particles as a function of radial location. The number of light reflections at any given radial location was divided by the total number of light reflections appearing in a particular run. This normalization was necessary due to differences in lighting that may have occurred between runs. To perform the same analysis on the smaller particles, the larger ones were dyed black and the process was repeated. The experiments with the dyed particles were performed with a cardboard separator in the apparatus, shortening the effective length of the experiment (see figure 4.3), thus requiring fewer dyed particles. It addition, the shallower depth (usually only 5-7 cm) corresponded more closely with the geometry of the three-dimensional computer simulations with which data was compared.

### 4.2.3 Bulk measurements of mass fraction

Another type of measurement performed on the experiment was a bulk measurement of the mass fraction of each type of particle in a particle mixture of two different sizes. Using the experiment in its horizontal orientation with the false bottom cardboard ring (see figure 4.3), the experiment was run for between 10 and 20 minutes. The apparatus was then carefully rotated 90 degrees to its upright position and the window removed to gain access to the bead mixture. Eight aluminum separators were inserted into the mixture at 45 degree intervals, separating the circular region into eight sectors. The particles were removed from each sector, separated, and weighed (with an accuracy of $\pm 1$ gram, or roughly 2%). This procedure yielded measurements of the mass fraction of each kind of particle as a function of angular location.

# Chapter 5

# Cylindrical Couette Flow: Experiments and Simulations

This chapter contains results from experiments and computer simulations and provides comparisons between the two for the same conditions. Comparisons between computer simulations and experiments are extremely important for validation of the simulation models. In flows of identical particles, mean velocities and velocity fluctuations are measured. In binary mixtures, segregation of the two mixture components is investigated using both experiments and simulations.

## 5.1 Single size particle flows

This section presents velocity profiles and fluctuation velocities from experiments and three-dimensional simulations of cylindrical Couette flow for identical particles.

Much of current granular flow theory is derived from the analogy between particles in a granular material and individual molecules in a dense gas. Thus, the temperature of a gas is analogous to the fluctuation velocity of the granular particles. Experimental measurements of both components of the fluctuation velocity have previously been made by Drake [1991] and Natarajan, Hunt and Taylor [1995] in inclined chute flows and vertical channel flows, respectively.

Experiments in two-dimensional cylindrical Couette flows have also been conducted recently. Elliot, Ahmadi, and Kvasnak [1998] conducted rapid Couette flow experiments on spherical glass particles 12 mm in diameter confined in a monolayer. The particles were placed between inner and outer walls that rotated in opposite directions and were roughened by the attachment of toothed rubber belting. The axis of rotation was vertical, parallel to the direction of gravity. Video imaging very similar to that used in the current experiments was used to measure solid fractions, velocities, and fluctuation velocities in the two-dimensional system. Average solid fractions in this study were low (less than 30% in three dimensions) and strain rates in the material were between 6 and 16 $s^{-1}$, higher than in the current experiments. Veje, Howell and Behringer [1999] recently conducted experiments on photoelastic disks resting on a smooth surface and being slowly sheared between a rotating inner wheel and an outer stationary ring, each coated with plastic "teeth." The inner cylinder rotated with a period of between 100 and 2000 seconds, significantly more slowly than in the current experiments. The initial dilation of the material was investigated as well as packing density profiles, mean velocity profiles and spin profiles for different rotation rates and packing fractions.

Because of the difficulty in making experimental measurements in granular flows, computer simulations are often used in their study. The research presented in this chapter offers direct quantitative comparison of results from experiments and computer simulations.

The experiment described in the previous chapter was used to study flows of particles of the same size. Two different sizes of spherical glass beads (6 mm and 4 mm in diameter) were used in the apparatus. In addition, two different sizes of the rotating inner cylinder were used: the largest inner cylinder, with a diameter of 14 cm, and the medium inner cylinder, with a diameter of 12 cm. The outer cylinder, with an inside diameter of 20 cm, was stationary while the inner cylinder rotated at various speeds up to approximately 45 RPM. Both shearing surfaces were covered

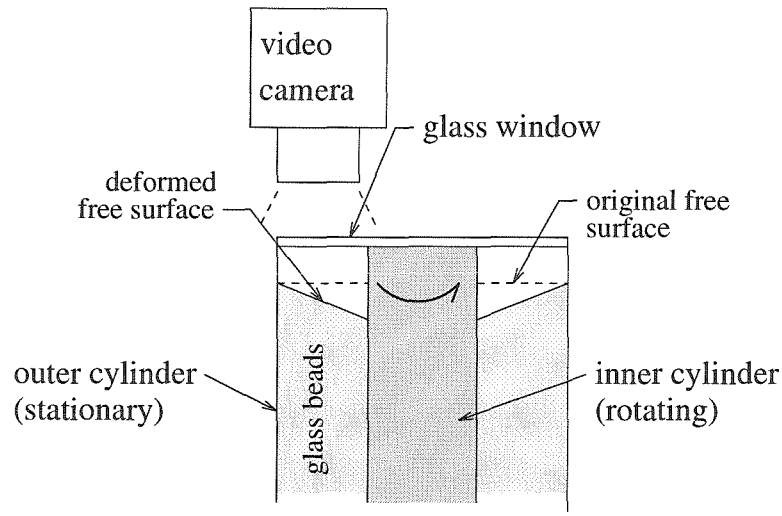


**Figure 5.1** Cross-section of top region of vertically-oriented experiment, illustrating the original and final free surface locations.

with sandpaper for roughness. This section discusses the mean particle velocities and fluctuation velocities determined through the use of high-speed imaging. The imaging method is described in Chapter 4.

### 5.1.1 Vertical orientation: experiments

When the experiment is vertically oriented, with the cylinder axis parallel to the direction of gravity, the viewing window is at the top. The free surface of the glass beads is a few centimeters away from the glass window. Velocities for the vertical experiments were determined for the particles at the free surface only; it is not clear how these velocities might differ from those within the flow. The flow is observed to have a vortical nature; that is, while the inner cylinder rotates, the free surface is not level, but rather it slopes down toward the inner cylinder (see figure 5.1).

Due to this unevenness in the free surface where the video was taken, the radial component of the particle velocities was not zero, because particles were continually

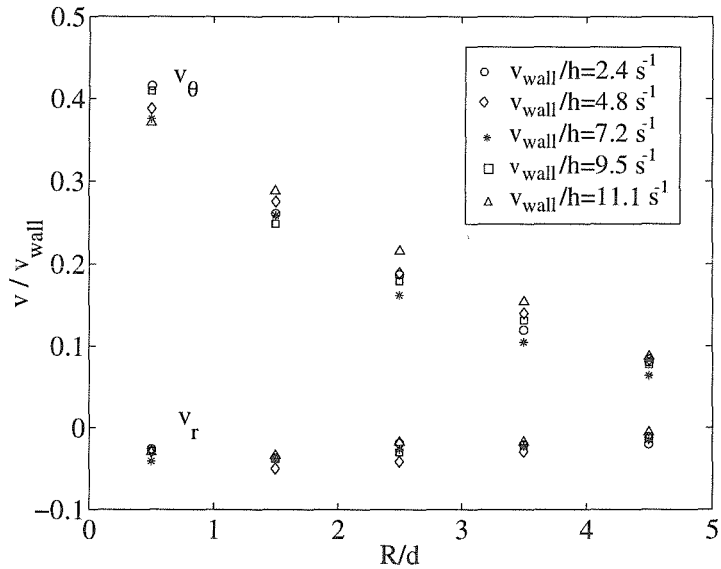


**Figure 5.2** Experimental velocity profiles at various strain rates for vertical orientation with largest inner cylinder and 6 mm beads ($h/d = 5$).

rolling down the inclined surface toward the inner cylinder. Khosropour et al. [1997] performed similar experiments in a vertically-oriented Couette flow apparatus, and observed the velocity of one large particle in a flow of smaller beads. A convection pattern was observed in which a thin (a few small particle diameters) layer of beads near the inner cylinder traveled downwards. The observations of that experiment are similar to those of this experiment, although it was not possible to make quantitative observations of the phenomenon in the current apparatus. However, an observer of the current vertical experiments would clearly see particles rolling down the inclined free surface and a net motion toward the inner cylinder.

The slanting of the free surface made measurements of velocities at the surface difficult, because the camera did not observe a level plane. Nevertheless, measurements were made of flows with the largest inner cylinder and 4 mm and 6 mm beads ($h/R_{inner} = 0.43$, with $h/d = 5$ and $h/d = 7.5$). Mean particle velocity profiles in the

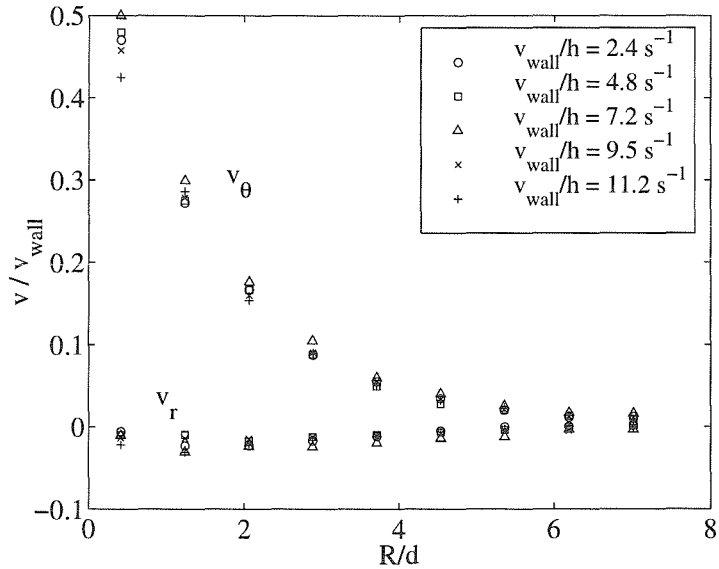


**Figure 5.3** Experimental velocity profiles at various strain rates for vertical orientation with largest inner cylinder and 4 mm beads ($h/d = 7.5$).

flow direction ($v_\theta$) and the transverse direction ($v_r$) are shown in figures 5.2 and 5.3. Experiments were performed at five different rotation rates, specified by the strain rate, $v_{wall}/h$. The mean velocity of the particles in each averaging bin (roughly one particle diameter in width) is calculated by comparing consecutive frames of high-speed video (see Chapter 4). The velocity is plotted in figures 5.2 and 5.3 as a function of the radial location, which is normalized by the particle diameter $d$. The position $R/d = 0$ corresponds to the location of the inner rotating cylinder, and $R/d = 5$ or 7.5 corresponds to the stationary outer cylinder surface. The velocity at each location has been normalized by the velocity of the moving inner cylinder surface ($v_{wall}$). The particle velocities collapse fairly well when normalized by the wall velocity in this manner. Therefore, the shape of the velocity profile is independent of the velocity of the inner wall, and the velocity of the particles is linearly proportional to the wall velocity. Measurements of the mean radial velocity component show that

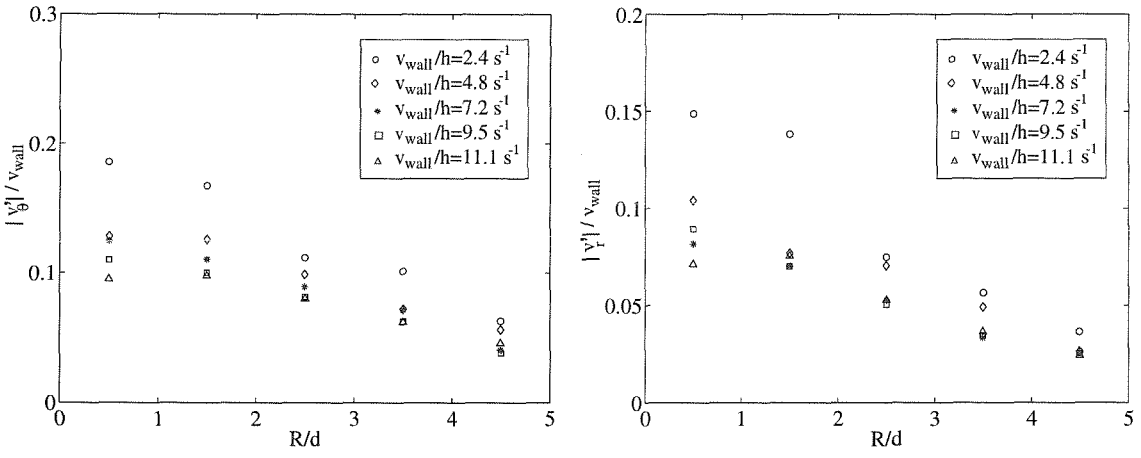


(a) Flow ($\theta$) direction

(b) Perpendicular ($R$) direction

**Figure 5.4** Experimental profiles for the two measurable components of fluctuating velocity at various strain rates with largest inner cylinder and 6 mm beads ($h/d = 5$); vertical orientation.

the radial velocity is slightly negative, due to the avalanching of particles toward the inner cylinder.

In the recent study of a two-dimensional vertical Couette flow by Elliot et al. [1998], velocity profiles were found to be generally linear with $R/d$, unlike those of the current study. In that study, both inner and outer walls were moving, and, additionally, the surface roughness was probably greater than that of the current experiments (they used toothed rubber belting). In addition, although the profiles were generally the same at various strain rates, the slip velocity at the outer wall decreased with increasing strain rate, a phenomenon not observed in the current study. The mean velocity profiles in the similar two-dimensional study of photoelastic disks by Veje et al. [1999] resemble the current profiles more closely, because only the inner cylinder is rotating, just as in the current work. In that work, the gap width is approximately 15 particle diameters in width, and the velocity profile levels off near zero at around

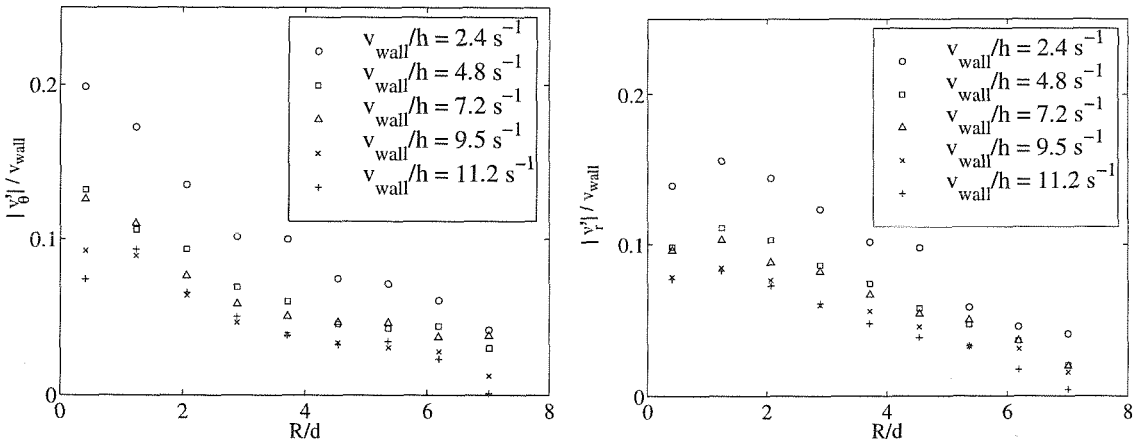


(a) Flow ($\theta$) direction

(b) Perpendicular ($R$) direction

**Figure 5.5** Experimental profiles for the two measurable components of fluctuating velocity at various strain rates with largest inner cylinder and 4 mm beads ($h/d = 7.5$); vertical orientation.

$R/d = 7$ for all rotation rates. At the lower velocities near the outer cylinder, the non-dimensional velocities were not rate invariant. In that work, the authors suggest that the breakdown in rate invariance is caused by fluctuations in the packing profiles during shorter times, and that rate independence might be observed if data were obtained over much longer times. As in the work of Elliot et al. [1998], the boundary conditions of the work of Veje et al. [1999] are also very different from the ones in the current study.

Fluctuation velocities were also measured for the flow described above. The fluctuation velocity of a particle is calculated by subtracting the mean velocity of its averaging bin from its velocity. The average fluctuation velocity in each bin is calculated by squaring each particle's fluctuation velocity, averaging this quantity over all

the particles in the particular bin over time, and taking its square root:

$$|v'| = \sqrt{\langle (v - \langle v \rangle)^2 \rangle}. \tag{5.1}$$

Figures 5.4(a) and (b) show the fluctuation velocities in the flow direction, $v'_\theta$, and transverse direction, $v'_r$, as functions of radial distance. Because the fluctuation velocity is related to the standard deviation of the mean velocity, any errors in velocity measurement are attributed to fluctuations in the velocity. Such errors are due to a particle not being tracked correctly from one frame to the next and being attributed a false velocity far from the mean. Because the error is not systematic and is not directional, it will cancel to zero in the mean velocity measurements. In the fluctuation measurements, however, these errors will be considered fluctuations in the mean and contribute to the quantity plotted in figures 5.4 and 5.5. Unfortunately, it is not possible to separate the fluctuation velocity from the standard deviation due to error in the measurement. However, there is clearly a component of this quantity that does scale with velocity, indicating that the measurement of fluctuations is not overwhelmed by the error. The magnitudes of the fluctuation velocities in both directions increase closer to the inner cylinder, where there is a higher mean velocity gradient. Experiments by Natarajan et al. [1995] in vertical chutes also showed a larger transverse fluctuation velocity near the regions of higher strain rate, although the fluctuation velocity in the flow direction was generally constant. Measurements of fluctuation velocities in the work of Elliot et al. [1998] are nearly constant across the gap, but in that work the velocity profile was generally linear, with no large differences in the velocity gradient.

### 5.1.2 Horizontal orientation: experiments

Measurements using high-speed imaging are more accurate and easier to make when the experiment is horizontally oriented. The particles in this orientation are flush

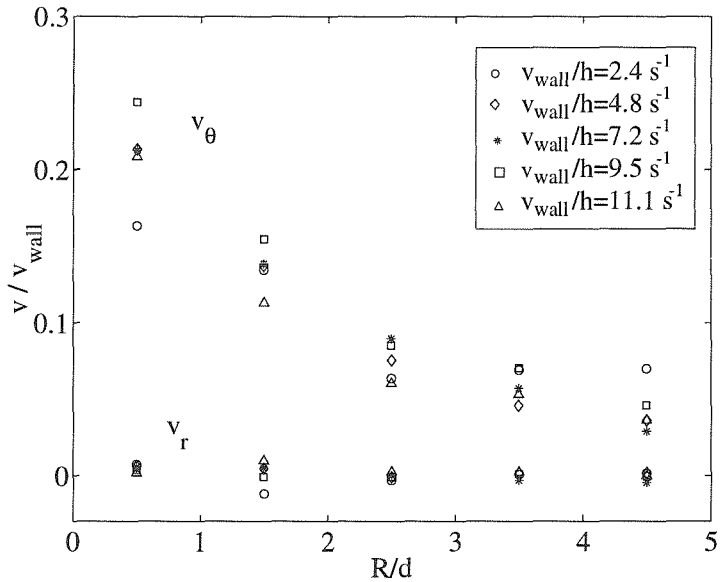


**Figure 5.6** Experimental velocity profiles at various strain rates for horizontal orientation with largest inner cylinder and 6 mm beads ($h/d = 5$).

with the surface of the glass, so the video camera can focus on the plane of the foremost particles. It is not clear from the experiments how particle velocities at the glass window differ from the velocities within the cylinder. In this orientation, measurements have been made using two different inner cylinder sizes (14 cm and 12 cm diameters) and two different sizes of glass beads (4 mm and 6 mm diameters). All measurements presented here were taken from video of the bottom of the experiment, nearest the floor and 180 degrees from the free surface, over an angle of approximately twenty degrees.

Figures 5.6–5.9 show the mean velocity in both the flow direction ($v_\theta$) and the transverse direction ($v_r$) as a function of non-dimensional radial position, $R/d$, for various strain rates, $v_{wall}/h$. Each figure represents data for a different value of $h/d$, based on varying both the gap width, $h$, and the particle diameter, $d$. In all four cases, the flow velocities scale with the wall velocity and the normalization collapses

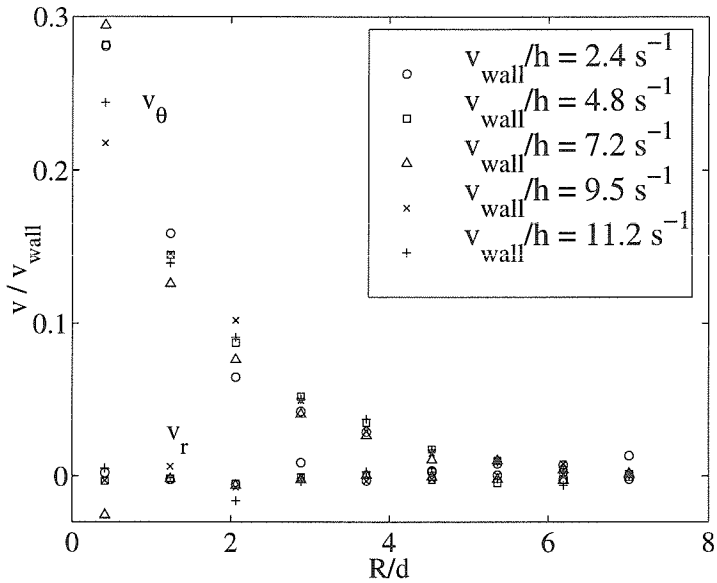


**Figure 5.7** Experimental velocity profiles at various strain rates for horizontal orientation with largest inner cylinder and 4 mm beads ($h/d = 7.5$).

the profiles for all the strain rates onto one curve. This result indicates, just as in the case of the vertically-oriented experiment, that the particle velocity scales linearly with the velocity of the inner cylinder. The mean radial velocities are very close to zero in all cases, as would be expected in a Couette flow.

The velocity of the particles adjacent to the inner cylinder (at $R/d = 0$) ranges from about $0.25v_{wall}$ to $0.35v_{wall}$, indicating that there is significant slip at the inner wall, from 65 to 75%. The velocity near the outer stationary cylinder is very close to zero in all cases except that of $h/d = 5$. It was visually observed that in this case of $h/d = 5$ the particles adjacent to the outer cylinder were not stationary; rather there was slip occurring at that cylinder as well. For the other experimental runs, the particle layer adjacent to the outside cylinder was not moving perceptibly. Figures 5.8 and 5.9, corresponding to the runs with the middle inner cylinder and a gap width $h$ of 4 cm, show that there are several particle layers near the outer wall that have

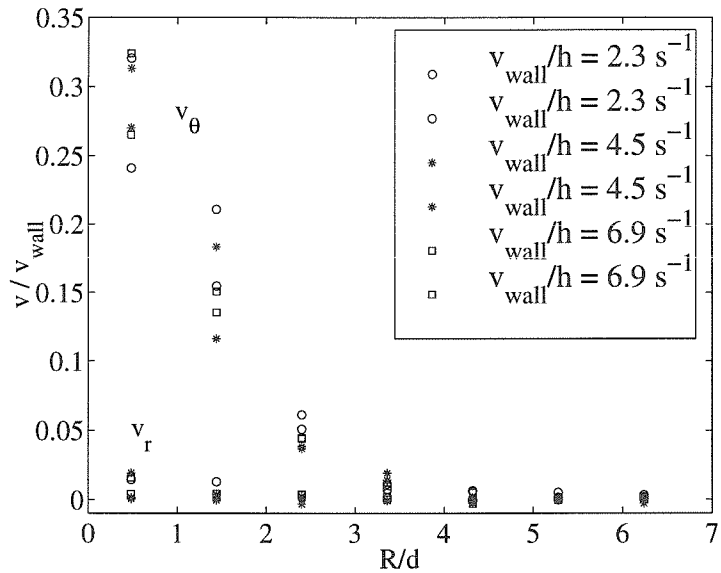


**Figure 5.8** Experimental velocity profiles at various strain rates for horizontal orientation with middle inner cylinder and 6 mm beads ($h/d = 6.67$). Each strain rate was repeated.

zero velocity. The number of non-shearing layers of particles does not seem to be a function of $h/d$ alone. For the run with $h = 3$ cm ($h/R_{inner} = 0.43$) and $h/d = 7.5$, there are two stationary layers near $R = h$. When $h = 4$ cm ($h/R_{inner} = 0.67$) and $h/d = 6.67$, however, there are three stationary layers of particles. Thus, a larger gap width $h$ results in a smaller region of shearing near the inner cylinder, regardless of the ratio $h/d$. At a given $h$, however, the number of non-shearing particle layers does depend on $h/d$, with larger values producing more stationary layers.

Ideally, $h/d$ would be the only variable in this Couette flow of particles, but the results show a dependence on $h/R_{inner}$ as well. If it were possible to keep $h/R_{inner}$ very small, the only variable would be $h/d$. However, in this experiment the value of $h/R_{inner}$ is either 0.43 or 0.67, both of order one. The mean velocity profiles illustrate that both $h/d$ and $h/R_{inner}$ are significant variables in the system.

The fluctuation velocities in both the flow direction ($\theta$) and the direction per-

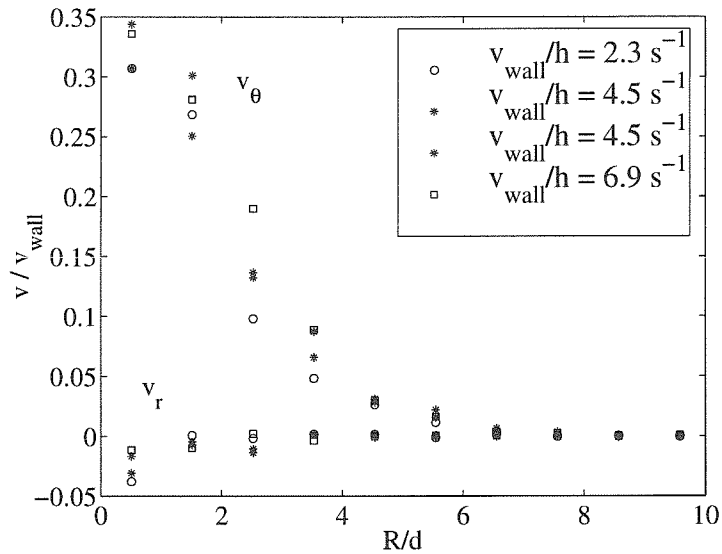


**Figure 5.9** Experimental velocity profiles at various strain rates for horizontal orientation with middle inner cylinder and 4 mm beads ($h/d = 10$). The run with the strain rate of 4.5 was repeated.

pendicular to the mean flow ($R$) were also measured in the horizontally oriented experiment. The definition of the fluctuation velocity is given in equation 5.1. The results for these measurements are shown in figures 5.10–5.13 for each of the four values of $h/d$. Each plot shows the fluctuation velocities for several different wall velocities, normalized by the wall velocity. The fluctuation velocities increase near the inner cylinder, where the flow is more agitated. The normalization collapses the results into bands, but there is still some scatter. This scatter is attributed to some error in the automated measurement technique, as explained in section 5.1.1 for the vertically-oriented experiment. Several of the experiments were repeated to illustrate the repeatability and quantify the scatter in the measurements.

In conclusion, results from the horizontally oriented experiments with particles of the same size show that average velocities scale linearly with the wall velocity. In addition, measurement of fluctuation velocities show that they increase in the region

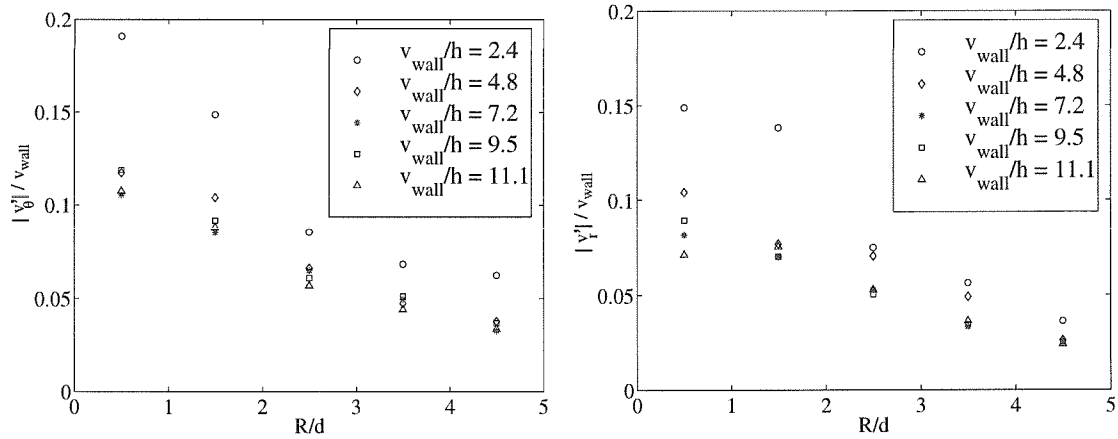


(a) Flow ($\theta$) direction

(b) Perpendicular ($R$) direction

**Figure 5.10** Experimental profiles for the two measurable components of fluctuating velocity at various strain rates with largest inner cylinder and 6 mm beads ($h/d = 5$).

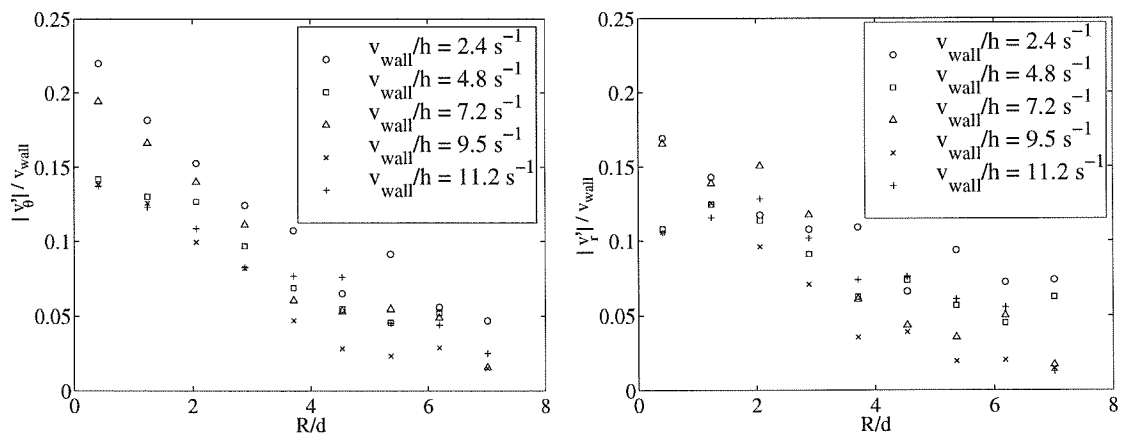


(a) Flow ($\theta$) direction

(b) Perpendicular ($R$) direction

**Figure 5.11** Experimental profiles for the two measurable components of fluctuating velocity at various strain rates with largest inner cylinder and 4 mm beads ($h/d = 7.5$).

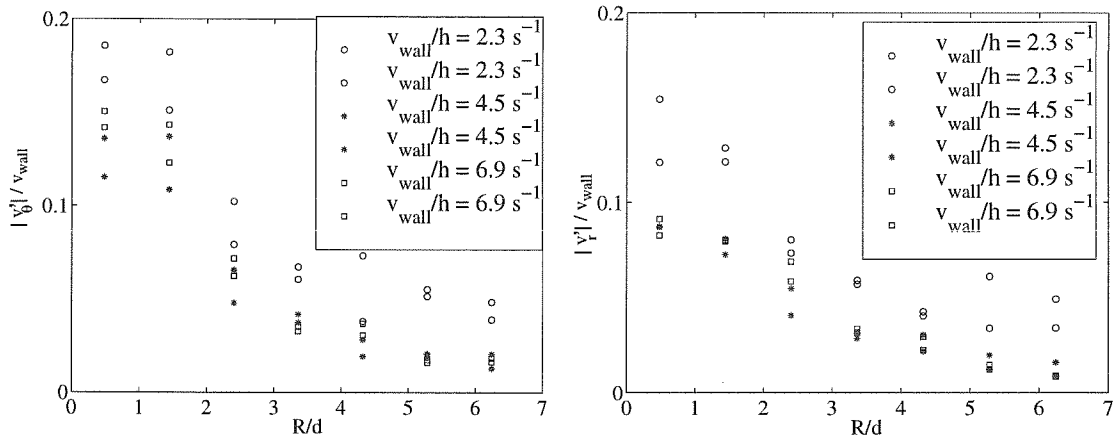


(a) Flow ($\theta$) direction

(b) Perpendicular ($R$) direction

**Figure 5.12** Experimental profiles for the two measurable components of fluctuating velocity at various strain rates with middle inner cylinder and 6 mm beads ($h/d = 6.67$).

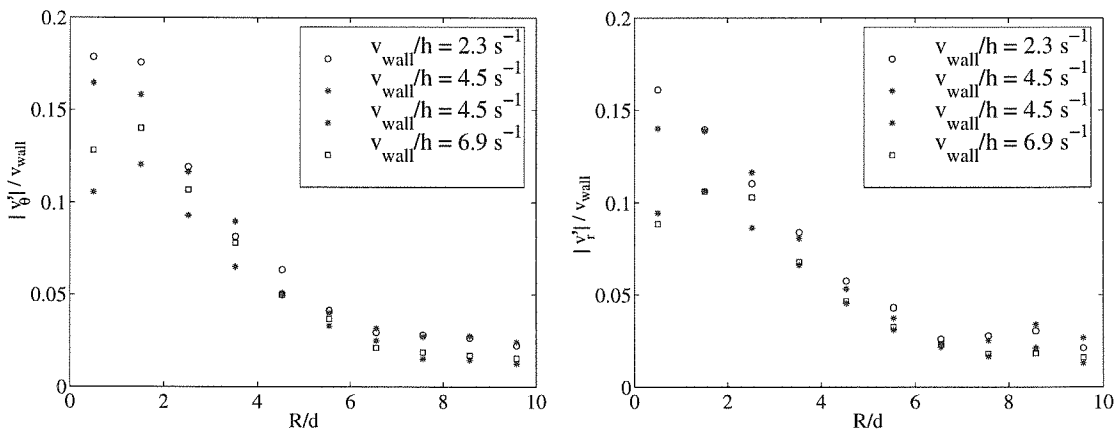


(a) Flow ($\theta$) direction

(b) Perpendicular ($R$) direction

**Figure 5.13** Experimental profiles for the two measurable components of fluctuating velocity at various strain rates with middle inner cylinder and 4 mm beads ($h/d = 10$).

of higher shear near the inner wall. This result has also been shown experimentally for transverse fluctuation velocities in a vertical chute [Natarajan *et al.*, 1995]. In all of the current experiments, the fluctuation velocities in the flow direction ($\theta$) are higher than those in the transverse, or perpendicular ($R$), direction. This anisotropy in the fluctuation velocities was also observed in certain regions by Elliot et al. [1998] in two-dimensional vertical Couette flows and by Natarajan et al. [1995] in the vertical chute experiments.

### 5.1.3 Horizontal orientation: computer simulations

Discrete element computer simulations, described in Chapter 2, were performed for comparison with experimental velocity and fluctuation velocity profiles. The simulations are three-dimensional and include contact forces and gravity forces. The normal contact force is modeled using the spring/dashpot contact model for almost all the simulations. The latched spring method is used in one simulation for comparison (see section 2.1.1 for description of contact models). The dimensions of the inner and outer cylinders in the simulations are identical to those of the experiment. The depth of the simulations, however, is only five particle diameters. The number of particles in the simulation is chosen so that the size of the free surface region is similar to that observed in the experiment. The front and rear walls of the simulations are flat surfaces with a coefficient of friction $\mu_w$ of 0.1. In the experiment, the front surface is glass and the rear aluminum, so that a low friction coefficient is expected. The inner and outer cylinders of the simulation have a wall friction coefficient of $\mu_w = 0.7$, to model the rough sandpaper. The inter-particle friction coefficient is chosen to be $\mu_p = 0.3$, to model the interaction of glass on glass. Smooth glass particles would be expected to have a lower friction coefficient than 0.3, but the particles used in the experiment develop roughnesses and are not perfectly circular; in the simulation, the higher coefficient of friction is chosen to incorporate these effects. The coefficient of restitution of collisions between particles, $e_p$, is 0.9 for most simulations, except one

for which $e_p = 0.7$ for comparison. The coefficient of restitution of particle collisions with all walls is $e_w = 0.7$. The density of the particles is approximately the density of glass, 2500 kg/m$^3$.

The particles were arranged in an initial random position with a small random velocity within the cylinder and allowed to settle under gravity. Each simulation was run for three seconds and properties were averaged for the last 1.5 seconds, once they had achieved a constant kinetic energy; samples were taken at a rate of either 50 or 100 samples per second. Average velocity profiles and fluctuation velocity profiles were calculated by averaging values in strips of about one particle diameter. All the results in this section are calculated at the bottom section of the circle, over an arc of 45° furthest from the free surface. The profiles are calculated at the front surface of the simulations; that is, only particles whose center is at $z < 0.75d$ are included in the averages. This is done so that the measurements are as close as possible to the experimental velocities, which are measured at the glass window. The strain rates ($v_{wall}/h$) for the simulations are 11s$^{-1}$ for the runs modeling the largest inner cylinder ($h/d = 5$ and $h/d = 7.5$), and 7s$^{-1}$ for those with the middle inner cylinder ($h/d = 6.67$ and $h/d = 10$). These are highest strain rates that the experiment was able to run, and the corresponding experimental results shown are taken from experiments run at approximately those strain rates.

Figure 5.14 shows the velocity profiles for two different simulations run under identical conditions, except that one uses the latched spring model and the other the spring/dashpot model. The latched spring model describes the physics of a normal collision more accurately than the spring/dashpot model, and it was thought that it might compare more favorably with experimental results. This does not seem to be the case, as the velocity profiles of the two contact models are nearly identical. The results from the corresponding experiment with $h/d = 7.5$ are also shown in figure 5.14, and show that the simulation results compare favorably those from experiments. Figure 5.15 presents the results from the two contact models along with

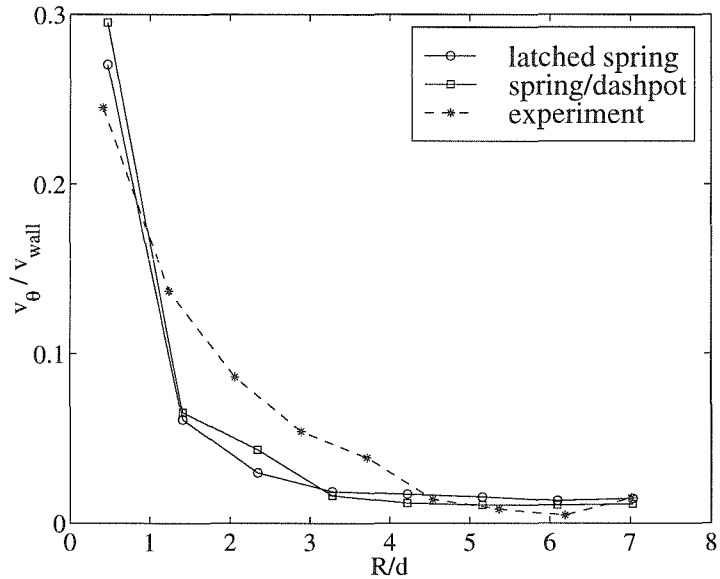


**Figure 5.14** Comparison of experimental velocity profiles with simulations using two different normal contact models; $h/d = 7.5$.

those from experiments for the fluctuation velocities in the flow direction (a) and the transverse direction (b). The simulations in this case both overpredict the fluctuation velocities from the experiments. It is not clear why the simulations do not model the correct fluctuation velocities.

Figures 5.16 and 5.17 present results from simulations and experiments at $h/d = 5$. The simulations were both run with the spring/dashpot contact model and identical conditions except for the particle-particle coefficient of restitution, which was 0.9 for the first simulation and 0.7 for the second simulation. This coefficient of restitution comparison was made to determine whether the fluctuation velocities would match experiments more accurately at this lower value of $e_p = 0.7$. The results show that although the simulation average velocity profiles match experiments relatively well, the fluctuation velocities do not. Just as in the case for $h/d = 7.5$, the simulation fluctuation velocities are significantly higher than those measured in experiments; the

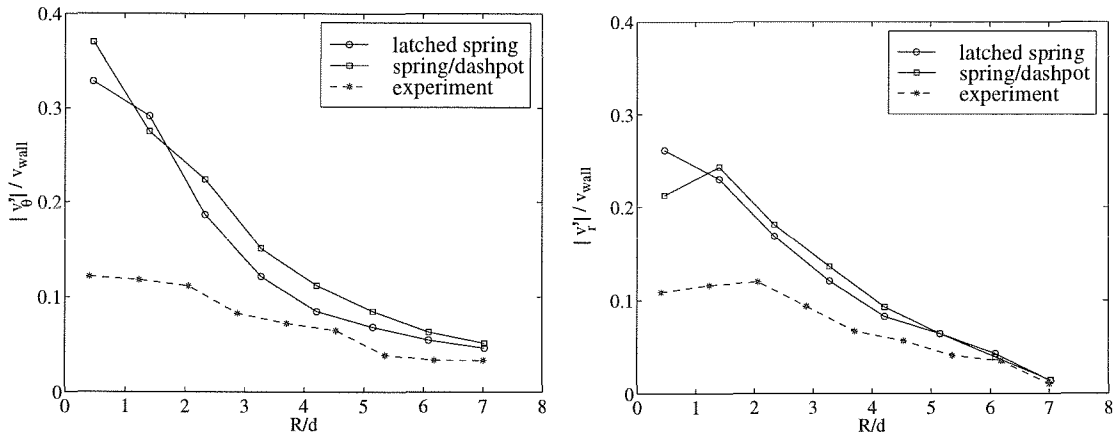


(a) Flow ($\theta$) direction

(b) Perpendicular ($R$) direction

**Figure 5.15** Comparison of experimental fluctuation velocity profiles with simulations using two different normal contact models; $h/d = 7.5$.

lower coefficient of restitution does not seem to make a difference in this case.

Figures 5.18 and 5.20 present the average velocity profiles from simulations and experiments for $h/d = 6.67$ and $h/d = 10$ respectively. Figures 5.19 and 5.21 show the results for the fluctuation velocity profiles. These simulations were both run with the spring/dashpot contact model and the particle coefficient of restitution of 0.9. Just as in the other two examples with the largest inner cylinder, the fluctuation velocities from the simulations are significantly higher than those in the experiments. In addition, it is clear that as $h/d$ increases, the velocity profiles do not match very well either (this is especially true in figure 5.20). The average velocity profile from the simulation has a much steeper slope near the inner wall than that of the experiment. The actual velocity at the wall is also somewhat lower in the simulations for many cases. Perhaps these discrepancies could be attributed to the simplistic contact models used by the simulations or the inaccuracy of the contact parameters chosen.

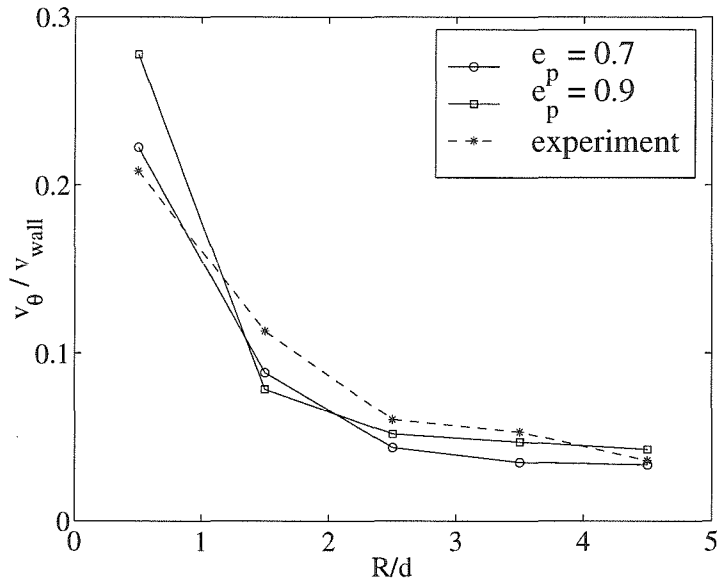


**Figure 5.16** Comparison of experimental velocity profiles with simulations using two different particle-particle coefficients of restitution $e_p$ with the spring/dashpot contact model; $h/d = 5$.

Much of the general flow behavior is reflected by the simulation results, however. For example, the general shape of both the average velocities and the fluctuating velocities is accurate. The increasing value of the fluctuation velocities near the inner rotating wall is observed in both simulations and experiments. In addition, the radial fluctuation velocity is generally lower than the angular fluctuation velocity in both. Therefore, although the simulations do not make accurate quantitative predictions, qualitative agreement is very good.

## 5.2 Mixtures

Experiments and high-speed imaging analysis were also conducted for flows of mixtures of particles of two different sizes. These mixtures were one-to-one by mass mixtures of 4 mm and 6 mm particles. Segregation was not studied in the vertically-

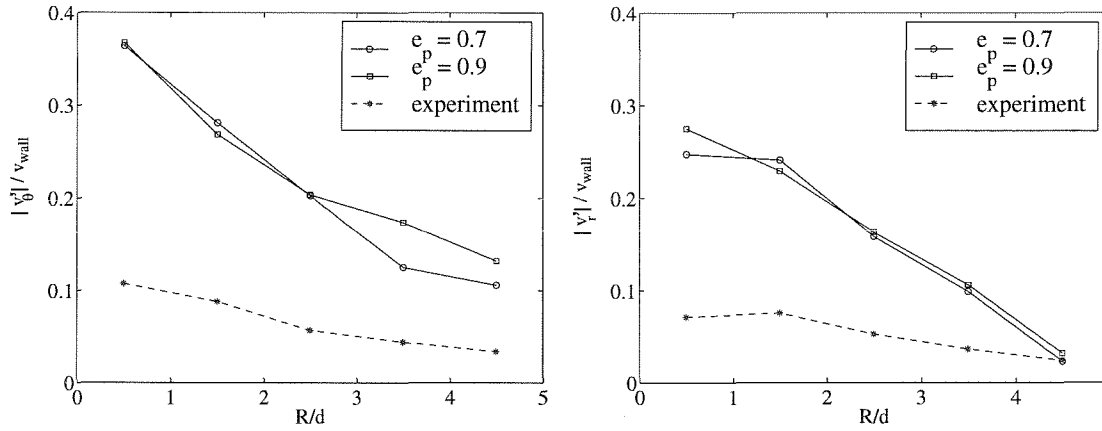


(a) Flow ($\theta$) direction

(b) Perpendicular ($R$) direction

**Figure 5.17** Comparison of experimental fluctuation velocity profiles with simulations using two different particle-particle coefficients of restitution; $h/d = 5$.

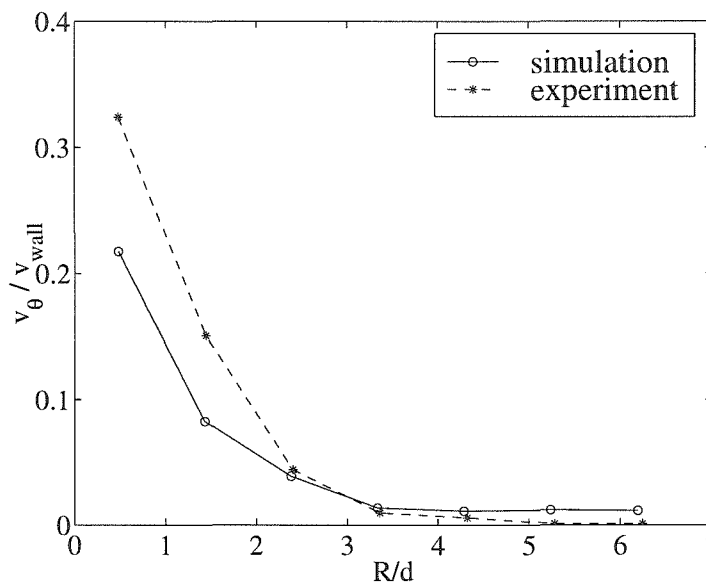


**Figure 5.18** Comparison of experimental velocity profiles with simulations for $h/d = 6.67$.

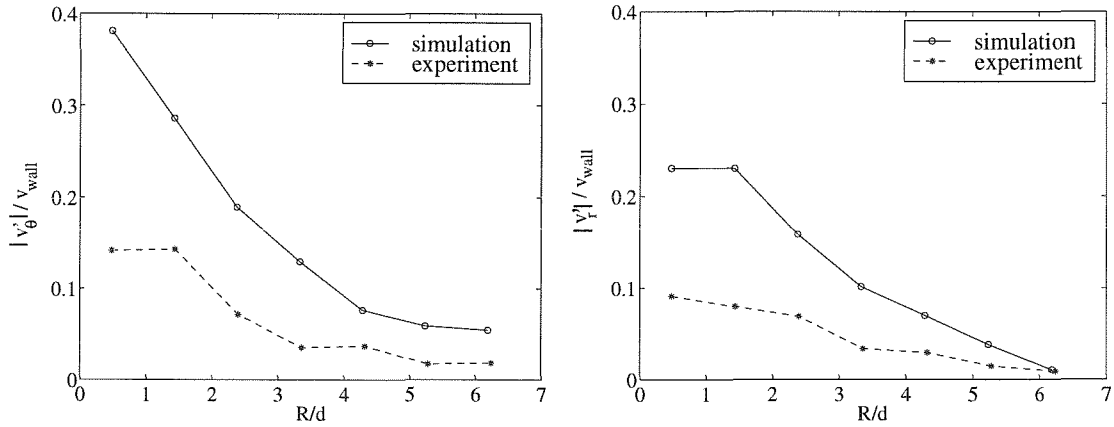


(a) Flow ($\theta$) direction

(b) Perpendicular ($R$) direction

**Figure 5.19** Comparison of experimental fluctuation velocity profiles with simulations for $h/d = 6.67$.

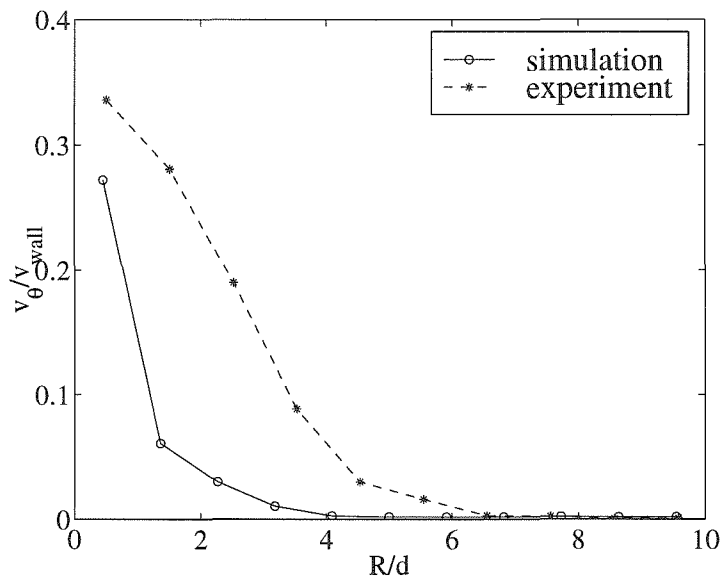


**Figure 5.20** Comparison of experimental velocity profiles with simulations for $h/d = 10$. Simulations use $e_p = 0.9$ and spring/dashpot contact model.

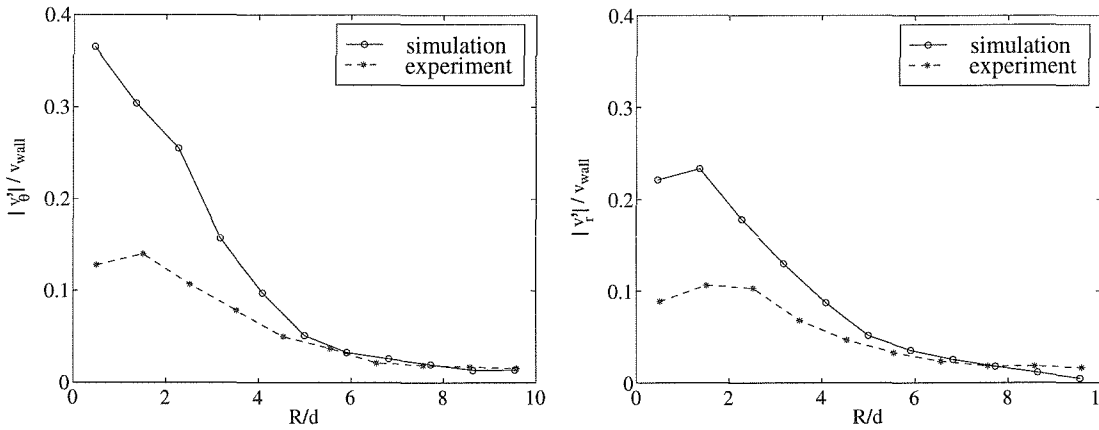


(a) Flow ($\theta$) direction

(b) Perpendicular ($R$) direction

**Figure 5.21** Comparison of experimental fluctuation velocity profiles with simulations for $h/d = 10$.

oriented experiment. Previous work has been conducted in the area of vertical segregation of Couette flows, however, in a recent study by Khosropour et al. [1997]. In that study, experiments of a vertically-oriented Couette flow similar in geometry to the current experiment were conducted using a single large particle (2 or 3 mm) placed in the bottom of the apparatus. The apparatus was then filled with smaller (1 mm) particles. The location of the larger particle was traced over time and its rising velocity was measured. A convection pattern was observed in which a layer of particles traveled downward at the inner cylinder wall, while the rest of the flow traveled upward at a slower velocity. After migrating upwards, the large particle remained at the free surface near the moving inner cylinder. It followed the convection pattern up to the free surface but was then unable to travel down along the inner cylinder due to its larger size. This sort of segregation pattern was not investigated specifically in the current experimental apparatus, but it was observed that after running for long periods of time in the vertical orientation, only large particles could be seen at the

free surface of the flow that initially contained a mixture of two particle sizes.

The current experiments on mixture flows were conducted in the horizontal orientation, so that any segregation of the large and small particles could be observed through the glass window at the front. Three-dimensional computer simulations of the same flow as in the experiment were conducted using the discrete element simulations described in Chapter 2. Both normal contact models (the spring/dashpot model as well as the latched spring model) were used to provide comparisons between each model and the experimental data.

### 5.2.1 Experiments

The experiment was run in its horizontal orientation with the false bottom described in Chapter 4 (see figure 4.3), so that the effective depth of the flow was only 5–7 cm. The front region of the experiment between the cardboard and the glass window was filled with a mixture of equal masses of 4 mm and 6 mm spherical glass beads. Two different sizes of the inner cylinder were used: the largest cylinder, with a diameter of 14 cm, and the medium cylinder, with a diameter of 12 cm. These correspond with a gap width, $h/d_{small}$, of 7.5 and 10 respectively. The velocity of the inner cylinder was approximately 18 cm/s, corresponding to a strain rate of $v_{wall}/h = 6\text{s}^{-}1$ for the runs with the large inner cylinder, and 27.5 cm/s ($v_{wall}/h \approx 6.9\text{s}^{-1}$) for the runs with the medium-sized inner cylinder.

### 5.2.2 Three-dimensional computer simulations

Three-dimensional discrete element simulations (described in Chapter 2) were used in conjunction with experiments to study the segregation pattern in the horizontally oriented cylindrical Couette flow. Interstitial gas forces are not accounted for in the simulations. Khosropour et al. [1997] conducted experiments on segregating Couette flows in a vacuum as well as in air and concluded that the absence of air did not change the results; thus, it is assumed that the error associated with the absence of

interstitial air in the current computer simulations is negligible.

The flows simulated are shear flows with gravity in the same geometry as the experimental flows. The main difference is that the depth of the simulations is only 5 large particle diameters. The experimental apparatus, even with the cardboard false bottom, is approximately 5 to 7 cm, or 8 to 12 large diameters long. All the other dimensions (cylinder diameters and particle diameters) are the same as those of the experiment. As in the same-size simulations, the number of particles in the simulations was chosen so that the free surface looked similar to that of the experiments. The inner and outer cylinders have a coefficient of wall friction, $\mu_w = 0.7$, to drive the flow, while the inter-particle friction coefficient, $\mu_p$, is 0.3. The front and rear boundaries are flat walls with a coefficient of friction of 0.1. The coefficient of restitution of inter-particle collisions is $e_p = 0.9$, and the coefficient of restitution of all wall collisions (including those against the front and rear walls) is $e_w = 0.7$. The density of the particles in the simulation is also approximately that of glass, 2500 kg/m$^3$. The nominal strain rate in the simulation, $v_{wall}/h$, is 11s$^{-1}$ when $h/d_{small} = 7.5$ and 7s$^{-1}$ when $h/d_{small} = 10$. These rates were chosen to coincide with the maximum shear rate possible in the experimental apparatus, although the experiments were actually performed at strain rates of 6s$^{-1}$ and 6.9s$^{-1}$, respectively. The overall solid fraction in three dimensions, $\nu$, defined as the ratio of particle volume to total volume, is 0.52, although it is much higher in most regions of the flow, since there is some empty space allowed at the top of the cylinder. As in the experiments, equal masses of large and small spherical particles are placed in the simulated container, and their diameter ratio is 1.5.

Just as was the case with the same-size particle simulations described in section 5.1.3, all simulations begin with the initial condition of randomly placed particles with small random velocities. They are allowed to settle under gravity and reach a steady state while the inner cylinder rotates. A steady state for the flow is generally defined as the state for which the kinetic energy is roughly constant. In the case

of mixture flows, however, segregation is a time-dependent process and it is more difficult to determine the steady-state condition. The steady state in the current work was determined by plotting the standard deviation of the concentration ratio of large to small particles at different angular locations against time. The simulation with $h/d_{small} = 7.5$ and the spring/dashpot contact model was run for 45 seconds of simulation time. The standard deviation of the angular number density profile was roughly constant after 20 seconds elapsed. Radial velocity profiles and number distributions were averaged between 30 and 35 seconds and compared with the averages taken between 40 and 45 seconds, with no differences between the two results. The simulation with $h/d_{small} = 7.5$ that utilized the latched spring contact model was run for a total of 35 seconds, and the properties were averaged for the last five seconds at a sampling rate of 20 times per second. The simulation with $h/d_{small} = 10$ was only run with the spring/dashpot contact model. It ran for 40 seconds, and properties were averaged for the last 2.5 seconds of the run. Generally, the result at a typical location represents the condition in an average of between 200 and 1000 particles.

### 5.2.3 Results and comparisons

Measurements in both computer simulations and experiments have been made at three angular locations of the flow. A snapshot of a mixture simulation running with $h/d_{small} = 7.5$ after 20 seconds is shown in figure 5.22, along with the three measurement locations, referred to as "left," "bottom," and "right." Angular velocity profiles and number density profiles are measured and compared at these three locations. In simulations, the measurements are made at each location over an arc of 45°. In experiments, the arc over which the measurements are made is usually between 15 and 30°.

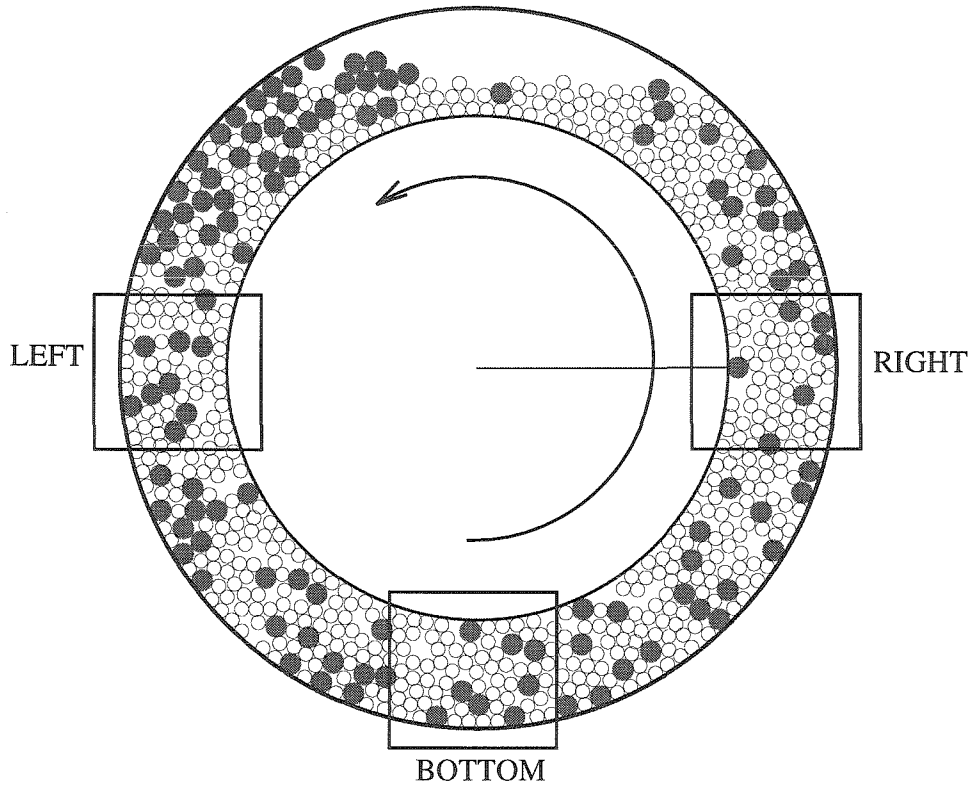


**Figure 5.22** View of front of computer simulation with the three measurement locations. The larger particles are shaded, and the arrow illustrates the direction of rotation of the inner cylinder. Only particles whose centers are at a depth of $< 1d$ are shown at their full size, so that there are some gaps and some overlaps in the snapshot.

### Velocity profiles

Figures 5.23, 5.24, and 5.25 show the velocity of each kind of particle in the angular direction, $v_\theta$, normalized by the velocity of the inner cylinder, $v_{wall}$, for experiments and simulations with $h/d_{small} = 7.5$. Experiments performed at different cylinder rotation rates with identical particles show that the velocity of the particles scales with the wall velocity in this manner (see section 5.1). The normalized velocity is plotted as a function of the radial coordinate normalized by the small particle

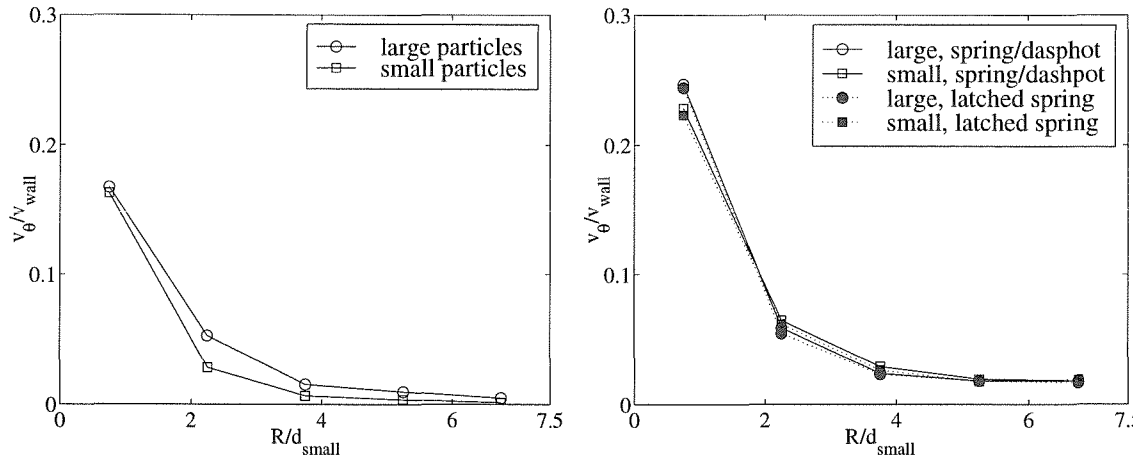


(a) Experiment (b) Simulation

**Figure 5.23** Velocity profiles for $h/d_{small} = 7.5$ at the left.

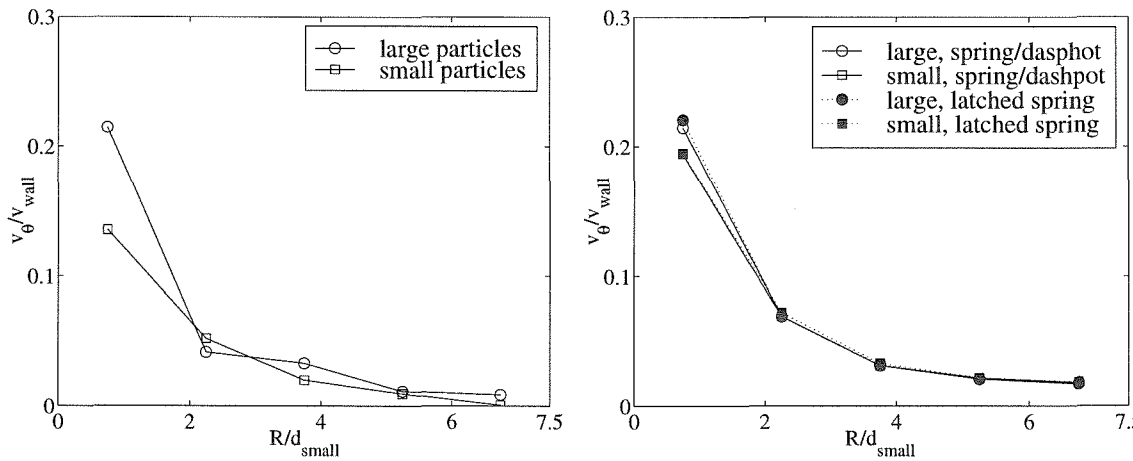


(a) Experiment (b) Simulation

**Figure 5.24** Velocity profiles for $h/d_{small} = 7.5$ at the bottom.

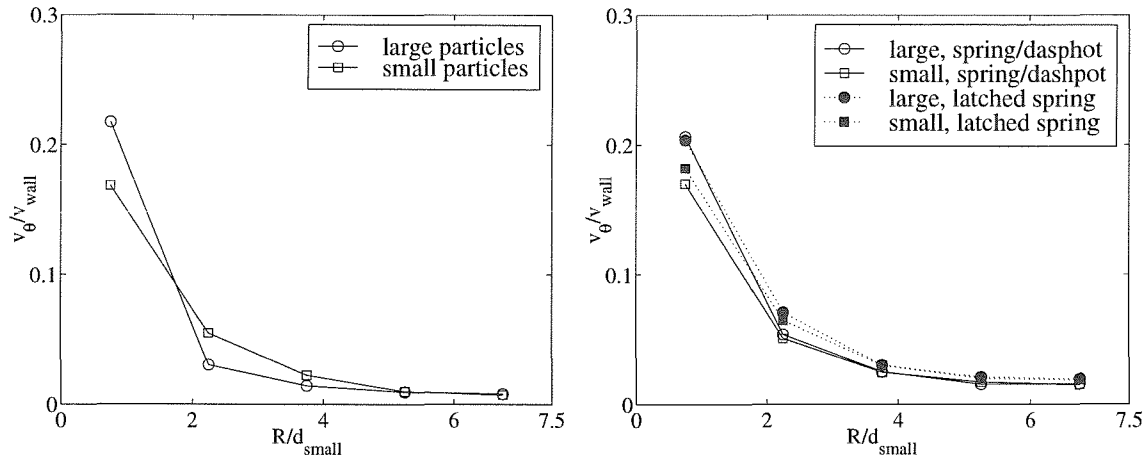


(a) Experiment (b) Simulation

**Figure 5.25** Velocity profiles for $h/d_{small} = 7.5$ at the right.

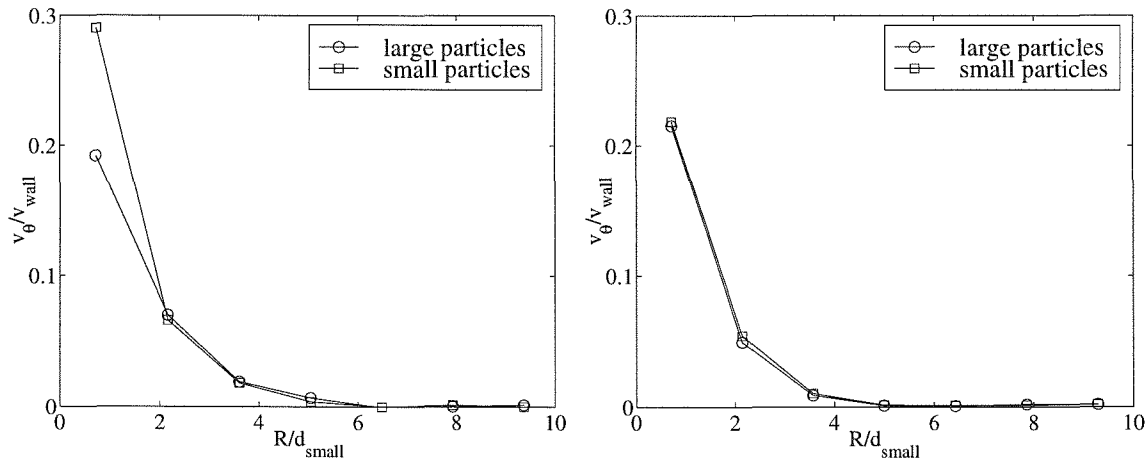


(a) Experiment (b) Simulation

**Figure 5.26** Velocity profiles for $h/d_{small} = 10$ at the left.

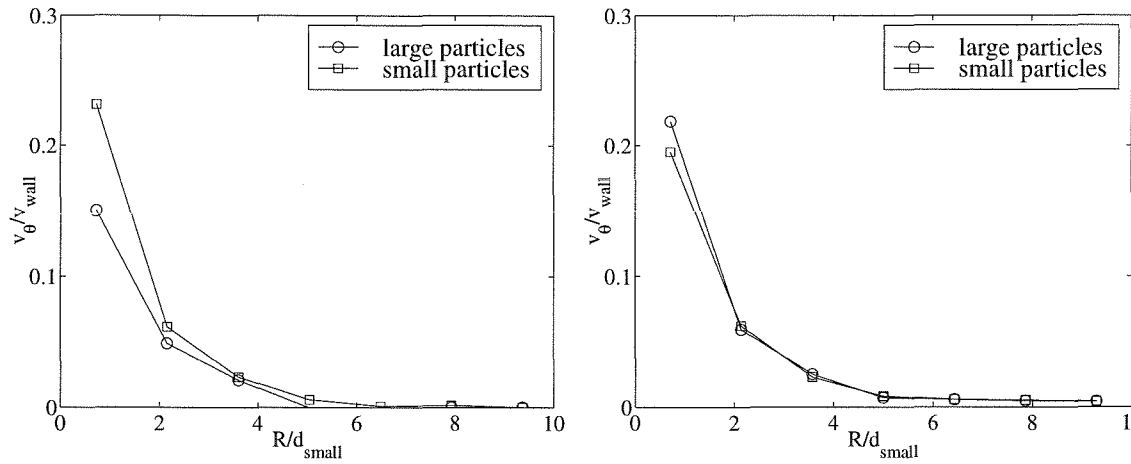


(a) Experiment (b) Simulation

**Figure 5.27** Velocity profiles for $h/d_{small} = 10$ at the bottom.

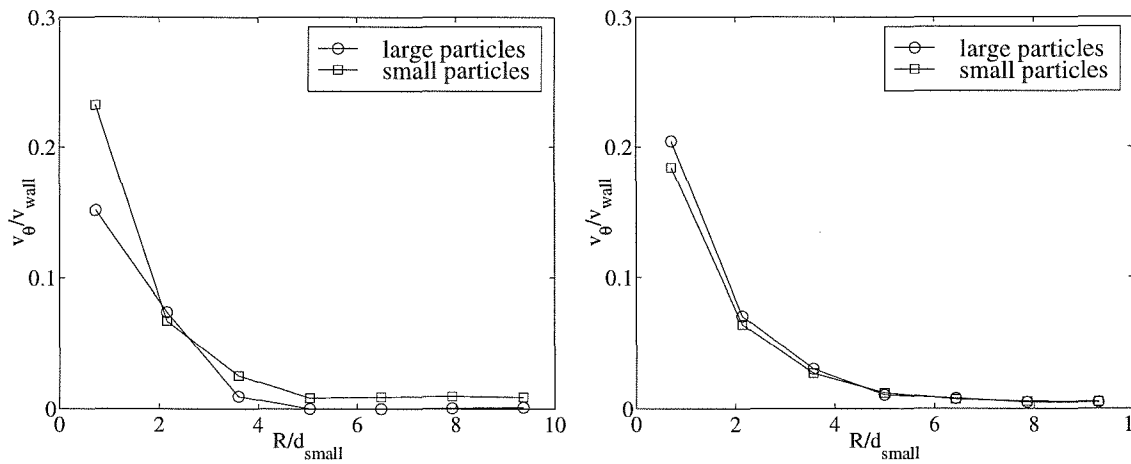


(a) Experiment (b) Simulation

**Figure 5.28** Velocity profiles for $h/d_{small} = 10$ at the right.

diameter (which is 4 mm in this case). The position $R/d_{small} = 0$ corresponds to the inner moving cylinder, while $R/d = 7.5$ corresponds to the outer, stationary cylinder. The corresponding plots for $h/d_{small} = 10$ are shown in figures 5.26, 5.27, and 5.28. The plots on the right side of each figure show the simulation results; these represent averages at the front surface of the simulations to correspond with the glass window of the experiment. The velocity profiles show no significant difference between the velocities of the two different kinds of particles except very near the inner wall, where smaller particles often have higher velocities. The experimental and simulation profiles agree very well for most cases. Results of simulations performed with the latched spring model are shown in filled symbols. The velocity profiles do not show a significant dependence on the contact model.

### Number density profiles

To determine angular as well as radial separation of large and small particles, measurements of number density of each kind of particle were made at each of three locations around the circle, as shown in figure 5.22. Due to changes in lighting among different experimental runs, the total number of particles counted using the digitizing method was not constant. It was thus necessary to normalize the number of particles of each type counted at a given radial location by the total number of particles of that size counted. To compare the number of large and small particles at each location, a quantity $N$ has been defined as follows:

$$N_{small} = \frac{\frac{n_{small}}{n_{small,tot}}}{\frac{n_{small}}{n_{small,tot}} + \frac{n_{large}}{n_{large,tot}}} \tag{5.2}$$

and, for the large particles,

$$N_{large} = \frac{\frac{n_{large}}{n_{large,tot}}}{\frac{n_{small}}{n_{small,tot}} + \frac{n_{large}}{n_{large,tot}}}. \tag{5.3}$$

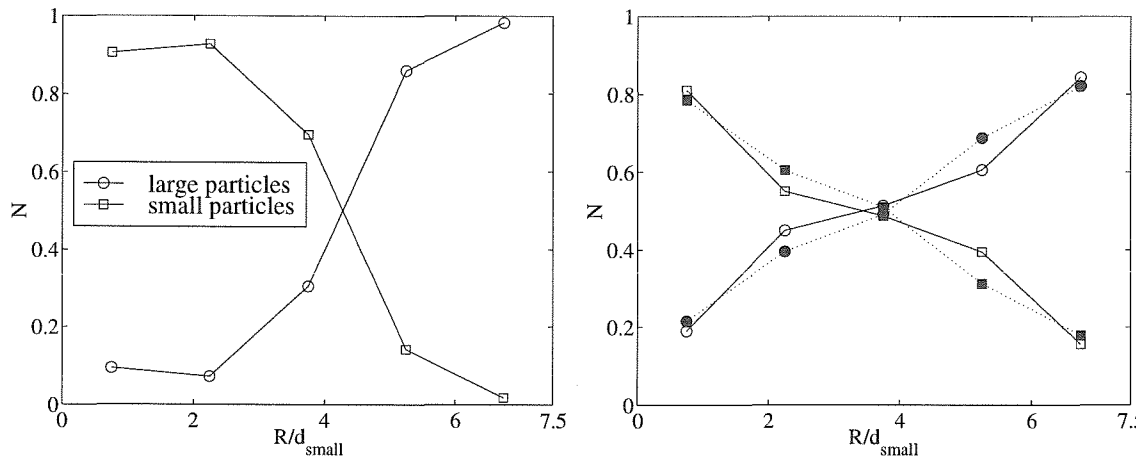


(a) Experiment (b) Simulation

**Figure 5.29** Results for $h/d_{small} = 7.5$ at the left side of the circle. The filled symbols represent simulations using the latched spring contact model.

Using this formulation, $N_{small} + N_{large} = 1$ at every radial location. Figures 5.29, 5.30 and 5.31 show the results for both experiments and simulations of the same flow as a function of radial position $R/d_{small}$, for $h/d_{small} = 7.5$. Although more simple and accurate results are possible using the computer simulations, the same quantity has been plotted for comparison. Figures 5.29(a), 5.30(a) and 5.31(a) illustrate the pattern of segregation observed visually in the experiment. At all locations, large particles are concentrated heavily around the outer, stationary cylinder, while small particles are concentrated around the inner cylinder. But the ratio of the two kinds of particles in the central region varies depending on angular location. Toward the left side of the circle, there are more large particles in the flow, while on the right side there are more small particles. Thus, the radial segregation from the inner to the outer cylinder depends upon angular position as well. Although some segregation is observed in the simulations (notably in 5.29(b)), significantly more radial segregation is observed in the experiment. Again, results for both the spring/dashpot contact

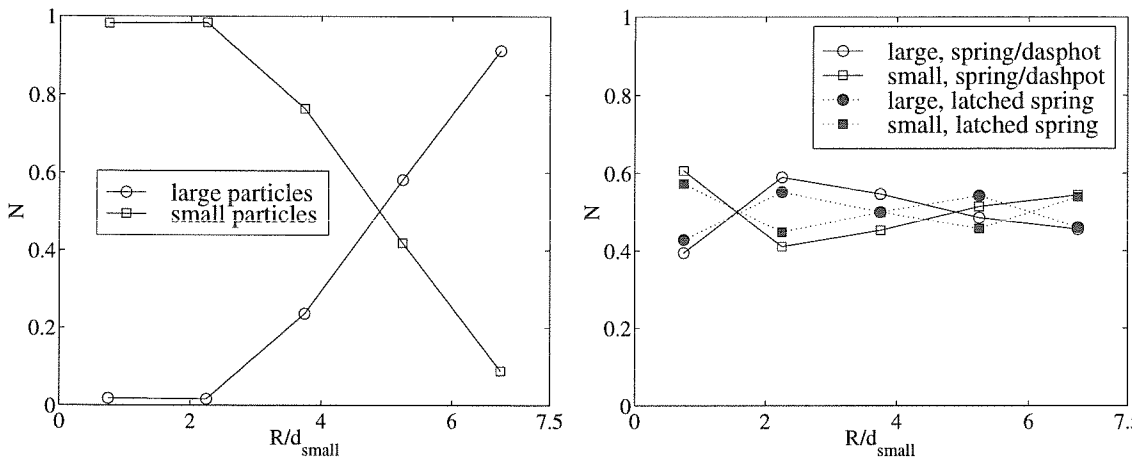


(a) Experiment (b) Simulation

**Figure 5.30** Results for $h/d_{small} = 7.5$ at the bottom of the circle.

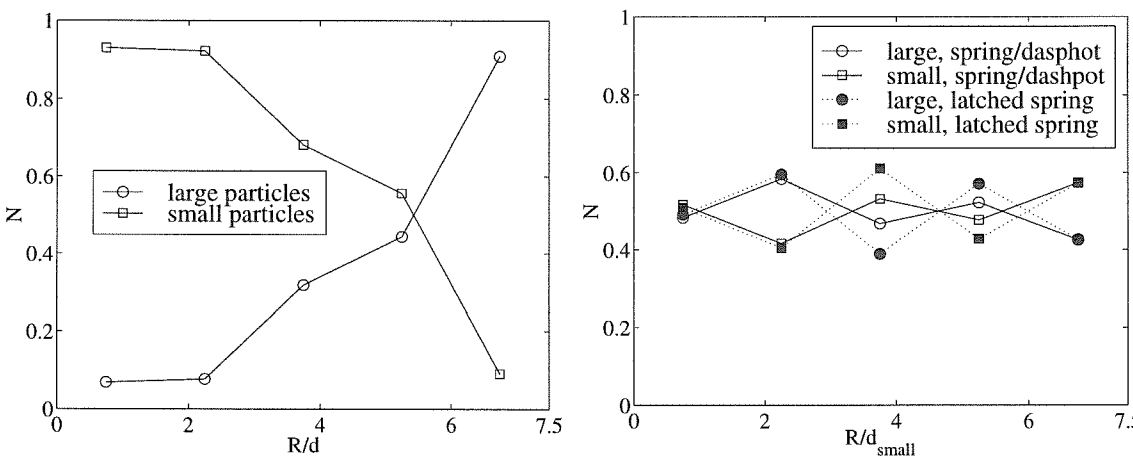


(a) Experiment (b) Simulation

**Figure 5.31** Results for $h/d_{small} = 7.5$ at the right side of the circle.

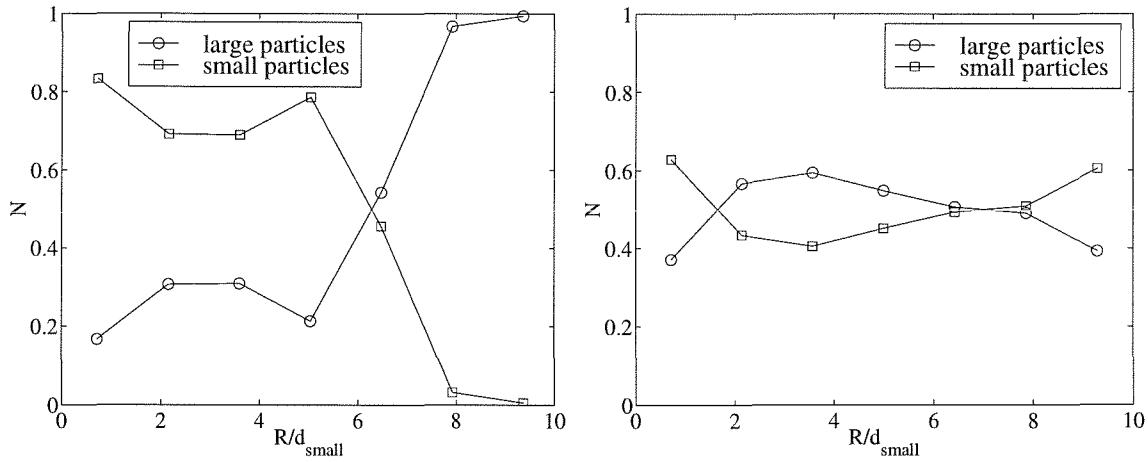


(a) Experiment (b) Simulation

**Figure 5.32** Results for $h/d_{small} = 10$ at the left of the circle.

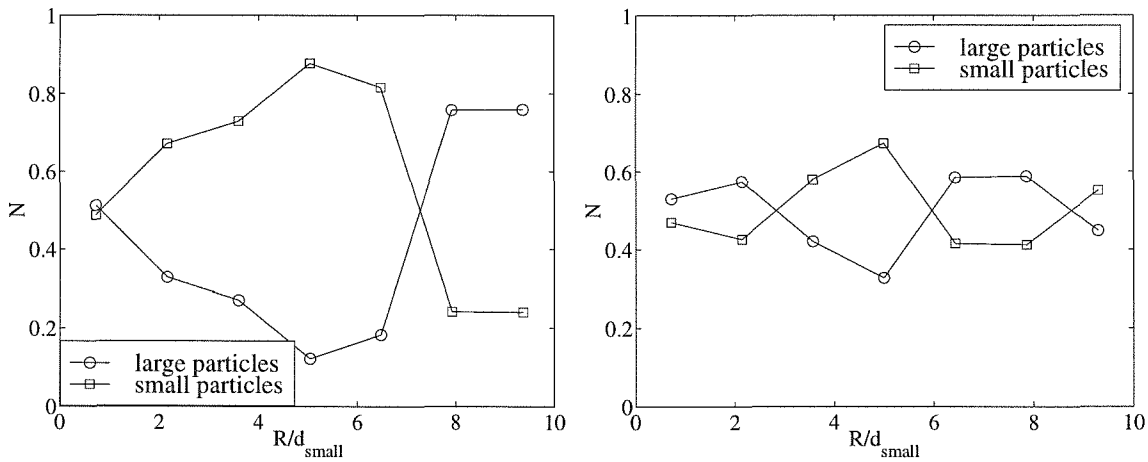


(a) Experiment (b) Simulation

**Figure 5.33** Results for $h/d_{small} = 10$ at the bottom of the circle.

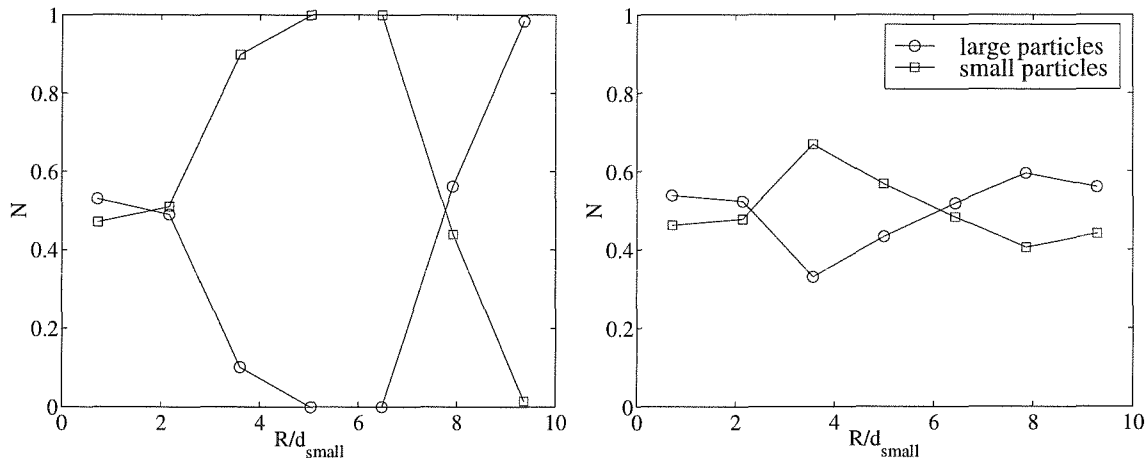


(a) Experiment (b) Simulation

**Figure 5.34** Results for $h/d_{small} = 10$ at the right of the circle.

model and the latched spring model are shown for comparison in 5.29(b), 5.30(b), and 5.31(b), but neither contact model captures the degree of radial segregation seen in the experiments. Figures 5.32, 5.33, and 5.34 show the same results for the middle inner cylinder ($h/d_{small} = 10$). Experimental results on the left side of each figure show that there is a radial segregation pattern that changes with location around the circle. Large particles still tend to concentrate near the outer wall, while small particles concentrate in the center region. Nearest the inner wall, for the bottom and the left parts of the circle, there is a more even mixture of sizes. Like the results for the smaller gap width, the simulations do not show a significant amount of radial segregation.

### Angular dependence of number density

To quantify the angular dependence of the number density, measurements of the mass of the large and small particles at eight different angular locations were made. In the experiment, eight aluminum separators were inserted into the granular material after

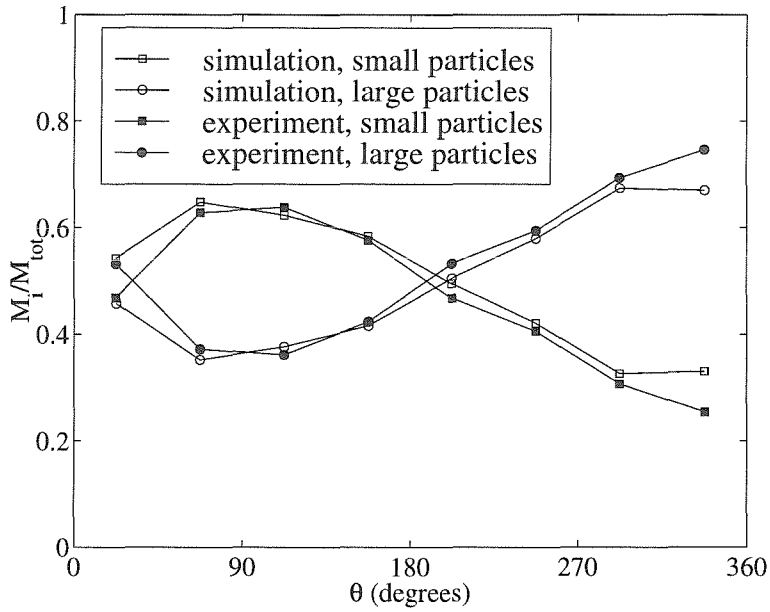


**Figure 5.35** The fraction of each kind of particle as a function of angular location for both simulations and experiments with $h/d_{small} = 7.5$. The angle $\theta$ is measured clockwise from the top, so that $\theta = 0$ corresponds to the top and $\theta = 90$ is on the right. Results are for simulation run with a spring/dashpot contact model.

the experiment had run for at least ten minutes and the amount of beads of each size in each sector were weighed (see section 4.2.3 for measurement method details). The same measurements were made in the computer simulations and experiments for the two different gap widths, $h/d_{small} = 7.5$ and 10. These measurements are made for the bulk material in the system, not just at the glass window.

Figures 5.35, 5.36, and 5.37 show the mass fraction of small particles and large particles at each of eight angular locations in the flow. The figures show that the fraction of large particles is highest in the upper left of the circle. This result can be also be observed in figure 5.22, where the larger shaded particles are clustered on the left side of the free surface. The large particles segregate in the agitated free surface region, rising to the top. This gravitationally induced segregation is

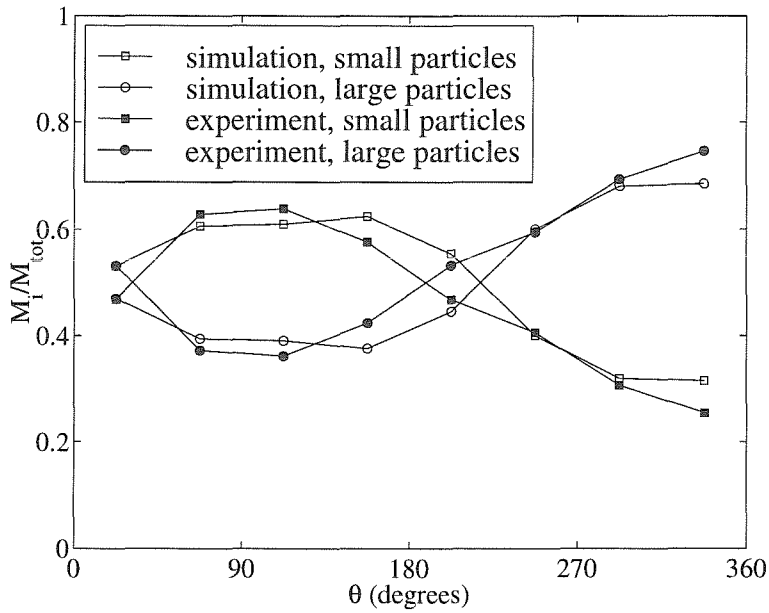


**Figure 5.36** The fraction of each kind of particle as a function of angular location for both simulations and experiments with $h/d_{small} = 7.5$. This simulation was run with the latched spring contact model.

similar to that observed previously in chute flows [Savage and Lun, 1988; Hirshfeld and Rapaport, 1997] and vertically vibrating flows [Gallas *et al.*, 1996]. In the more agitated region near the top of the circle, smaller particles have a higher probability of falling through an opening between other particles. Thus, there is a net flux of small particles downward toward the inner cylinder, while the larger particles are pushed up to the surface. A more complete discussion of this process can be found in the work of Savage and Lun [1988] in chute flows. In the case of the horizontal Couette experiment, however, the mean motion to the left pushes the large particles to the left side of the free surface region, introducing an asymmetry in the general flow. This asymmetry can be seen in figures 5.35 – 5.37; if the flow were symmetric then the mass fraction graph would also be symmetric about the 180° mark.

In the simulations (results are shown in the open symbols), the mass fraction

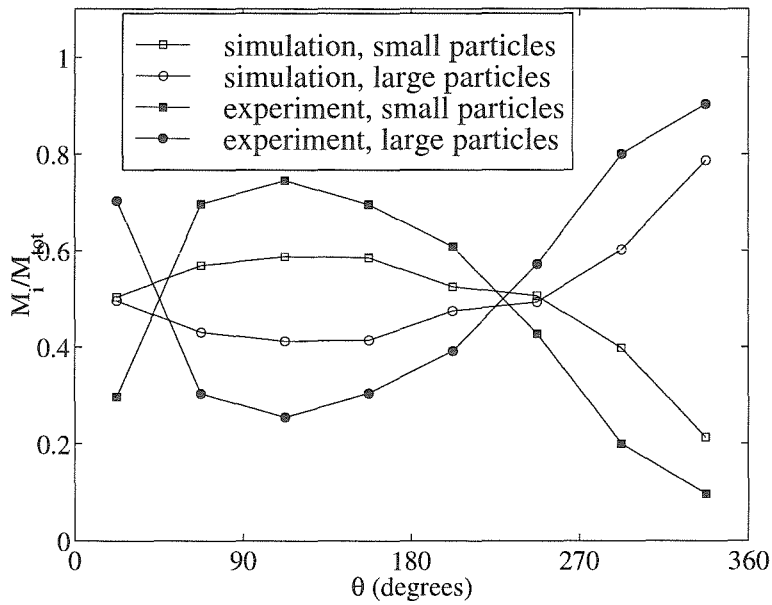


**Figure 5.37** The fraction of each kind of particle as a function of angular location for both simulations and experiments with $h/d_{small} = 10.0$.

measurements were made at the last sample taken of the simulation run. Simulations show the same qualitative behavior as experiments, and the results for $h/d_{small} = 7.5$ agree quantitatively as well (figures 5.35 and 5.36). As with the previous results, the choice of contact model does not seem to influence the results. In the simulations with $h/d_{small} = 10$, however, segregation in the simulations is significantly less than that in the experiment.

### 5.2.4 Discussion

In this horizontally oriented Couette flow, particle segregation originates at the free surface of the flow, in the top area of the circle. In this area a high degree of particle agitation causes larger particles to migrate to the top of the free surface, just as has been observed by previous researchers in chute flows [Savage and Lun, 1988; Hirshfeld

and Rapaport, 1997] and vertically vibrating flows [Gallas *et al.*, 1996]. The upper portion of the cylinder, near the free surface, behaves very much like an inclined chute flow described and explained by Savage and Lun [1988]. Once the large particles are at the top, they stay close to the outer cylinder as they move left around the circle with the bulk flow. This radial segregation can be seen in the experimental results of figures 5.29–5.34(a). As the large particles travel around the circle to the bottom, some migrate to the faster-moving region closer to the inner cylinder and quickly travel around back to the top. Others remain near the outer boundary, traveling around at a slower pace. Thus, the number of layers of large particles adjacent to the outer surface changes with angular position.

The current study also illustrates the degree of effectiveness of computer simulations when studying segregating flows. The simulations in this study capture the qualitative aspects of the segregation but not the extent to which the flow segregates. Radial number density profiles show much less segregation in the simulated flow than the experiment. Angular measurements of mass fraction also illustrate that the flow in computer simulations with $h/d = 10$ does not segregate as much as the experimental flow, although in simulations with a smaller gap width the simulations predict the angular segregation very well. In a recent investigation, Cleary et al. [1998] conclude that computer simulations capture the qualitative aspects of mixing and segregation but that quantitative measurements, such as the mixing rate, show a large sensitivity to parameters such as the particle coefficient of restitution and coefficient of friction. Similarly, the disagreement between the current simulations and experiments is probably due to a sensitivity of segregation to the particle and wall surface properties. In addition, although the implementation of a more physically accurate normal contact model did not alter results, perhaps the use of a more accurate tangential model would show better agreement with experiments.

# Chapter 6

# Wall Stresses in Cylindrical Couette Flow

One important goal of the research involving experimental Couette flows of granular materials is the measurement of the shear stress at the boundary. The measurement of shear stresses is valuable in discovering the work and energy input necessary to drive a particle mixer or shearing apparatus. Previous studies [Miller *et al.*, 1996; Hanes and Inman, 1985; Savage and Sayed, 1984; Tardos *et al.*, 1998] have made experimental measurements of the stresses on the walls of sheared granular material in various geometries. Savage and Sayed [1984], Hanes and Inman [1985], and Miller et al. [1996] all made experimental measurements of the shear stress in a conventional annular shear cell apparatus. Miller et al. [1996] studied the fluctuations of the normal stress measured by a pressure transducer flush-mounted on the floor of a shear cell with an upper rotating disk and stationary sides and bottom disk. Savage and Sayed [1984] and Hanes and Inman [1985] both studied the dependence of wall shear stress on the rate of strain in the material at a constant solid fraction. Tardos et al. [1998] performed experiments in a vertically-oriented cylindrical Couette apparatus similar to that of the current study. The material used in that study consisted of fluidized or partially fluidized small ($\leq$ 530 $\mu$m) particles.

In the current work, the shear stress on the outer stationary cylinder wall of the experiment was measured (see Chapter 4 for method and instrumentation). Shear stresses were measured in both the vertical and horizontal experimental orientations,

and as functions of strain rate, fill level, and gap width.

## 6.1 Vertical orientation

This section describes shear stress measurements for the apparatus in its vertical orientation, with the central axis of the cylinders oriented parallel to the direction of gravity and perpendicular to the floor. The experiment was placed on a 122 cm×122 cm wooden platform 40 cm off the floor for all of the vertical runs. For each experimental run, a known weight of particles was placed in the apparatus. In these experiments, glass beads with diameters of 3 mm, 4 mm, 6 mm, and 8 mm were used, along with all three sizes of inner cylinders. The beads were weighed prior to being poured in with an accuracy of ± 0.1 lbs = ± 0.44 Newtons. The height of the material in the apparatus was measured to calculate the surface area covered by the beads; this is the area on which the shear force was acting. The height of the beads was measured with an accuracy of ± 0.5 cm.

### 6.1.1 Shear stress as a function of time

Figure 6.1 shows the reading of the load cell for a typical vertical run, illustrating the large fluctuations of the signal with time. This data was taken with 35.6 N (8 lbs) of 6 mm glass beads in the apparatus, with the largest inner cylinder (14 cm diameter, resulting in a 3 cm gap) rotating at 45.4 RPM. Data was taken for 32 seconds at 500 Hz to capture the high-frequency fluctuations observed. Figure 6.2 shows the same data over a period of only 0.3 seconds. The circles are the actual sampled points, confirming that the high-frequency fluctuations are resolved adequately by the data acquisition system. Large fluctuations over a similar frequency range were also observed by Miller et al. [1996] in measurements of the normal stress in an annular shear cell, different in geometry from that of the current study. In the current study, the standard deviation of the time fluctuations increases both with strain rate and

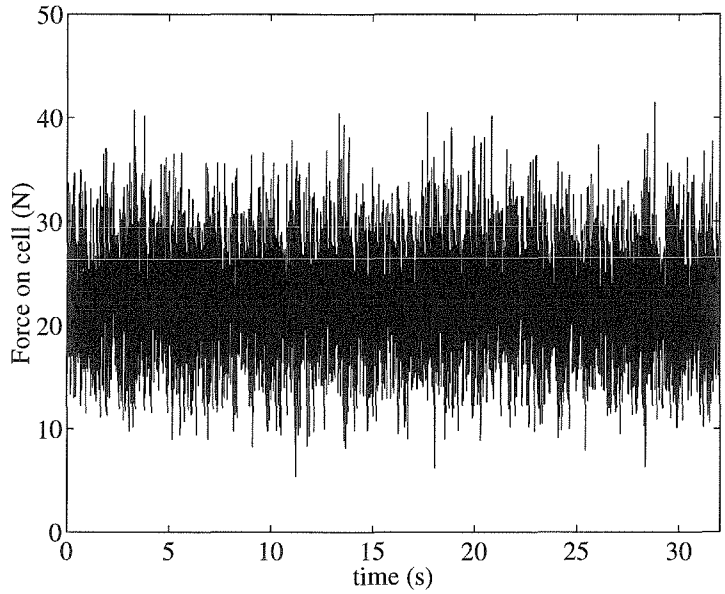


**Figure 6.1** Force on the load cell as a function of time for an experiment with 8 lbs of 6 mm beads over a period of 32 seconds. Sampling rate is 500 Hz.

with the magnitude of the stress.

The power spectrum of the same data shown in figure 6.1 is presented in figure 6.3, indicating several distinct peaks. The wooden platform on which the experiment rests vibrates while the experiment is running, probably contributing to the force fluctuations. There are distinct peaks at 120 Hz and 240 Hz, which are most likely harmonics of electrical noise at 60 Hz. The other frequencies are not distinct enough to attribute to specific causes. The spectrum does not visibly change with a change in the rotation rate of the inner cylinder.

### 6.1.2 Shear stress as a function of strain rate

The force signal is averaged over the 32-second acquisition period and the average value of the shear stress is calculated using the surface area of the outer cylinder

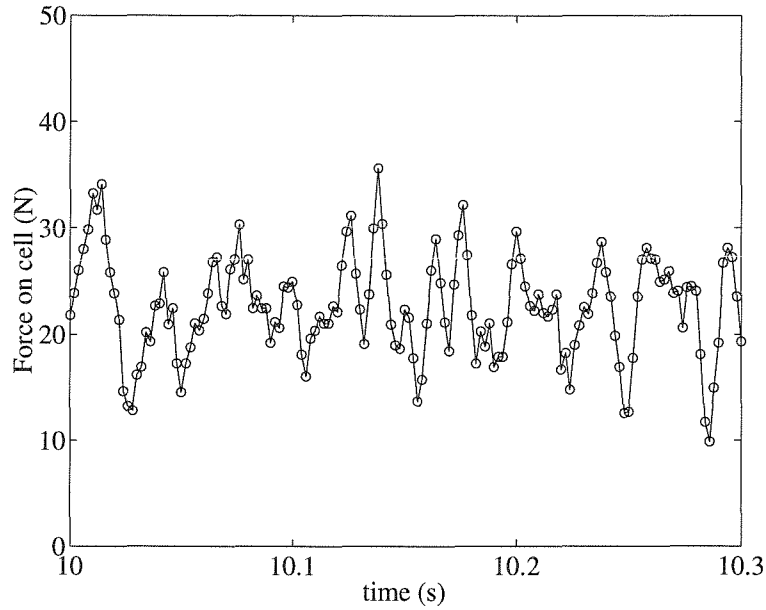


**Figure 6.2** Force on the load cell as a function of time; this is the same data as in figure 6.1 but only showing 0.3 seconds of data. The circles indicate sample points, the line simply connects these points.

covered by beads, as explained in section 4.2.1. It is assumed that the shear stress on the base of the cylinder is negligible. The shear stress is plotted as a function of rotation rate for each experiment. For each experimental run, data is taken at increasing rotation rates until the maximum is reached. The experiment is stopped and data is then taken at decreasing rotation rates from the maximum down to zero. Thus, at each rotation rate there are two averages taken. Figures 6.4, 6.5, and 6.6 show the results of the time-averaged stresses as a function of the strain rate for experimental vertical runs with the largest inner cylinder (diameter = 14 cm; $h/R_{inner} = 0.43$) and bead diameters of 3 mm, 4 mm, and 6 mm respectively. Stress measurements were also made with bead diameters from 3 to 8 mm for the other two inner cylinders (diameters of 12 cm and 8 cm, respectively), and are shown as functions of strain rate in figures 6.7–6.14.

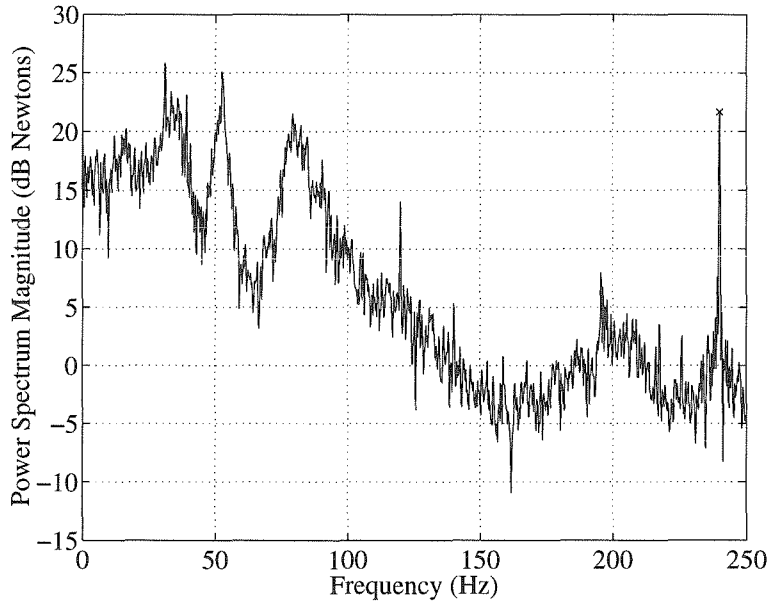


**Figure 6.3** Power density spectrum of the force on the load cell during a vertical experiment.

The strain rate is defined as the wall velocity divided by the gap width, $h$:

$$Strain\ rate = \frac{v_{wall}}{h} = \frac{\Omega R_{inner}}{R_{outer} - R_{inner}}, \tag{6.1}$$

where $\Omega$ is the rotational velocity of the inner cylinder. Because the maximum rotational velocity of the motor is a constant, the maximum possible strain rate achieved in the apparatus depends on the radius of the inner cylinder. The maximum strain rate for the smallest cylinder is just 3.1 $s^{-1}$, while for the largest cylinder it is 11 $s^{-1}$. Velocity profiles of these flows (see Chapter 5) confirm that the velocity of the beads is linearly proportional to the wall velocity, so that the strain rate defined above is proportional to the actual rate of strain in the material. The shear stress measurements at various strain rates show that the stress is independent of the strain rate in the material. At very low rotation rates the shear stress decreases slightly with

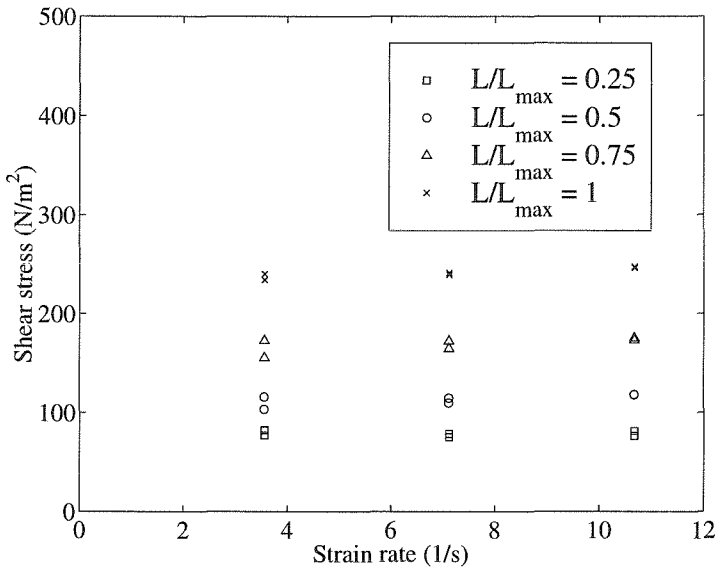


**Figure 6.4** Shear stress (averaged over time) as a function of strain rate for 3 mm glass beads in a 3 cm gap between cylinders ($h/d = 10$).

rotation rate, but for most it shows no dependence.

The explanation for the independence of shear stress on strain rate lies in two key factors: the classification of the flow regime and the dilation of the material undergoing shear. Dry granular shear flows have been classified into three basic regimes [Campbell, 1990; Savage, 1984]. A quasi-static regime occurs when the grains in the material are in frictional contact for a long time. At the other extreme, a rapid granular flow occurs when the energy in the flow is high, the strain rate is high, and collisions are almost instantaneous. The third, transitional regime, consists of flows between the two extremes. Quasi-static flows exhibit stresses that are rate-independent, such as those observed in the current research. Rapid flows exhibit stresses that vary with the square of the strain rate. Transitional flows have both rate-dependent and rate-independent components. The flow in the current experimental Couette apparatus is visually observed as exhibiting enduring, frictional contacts

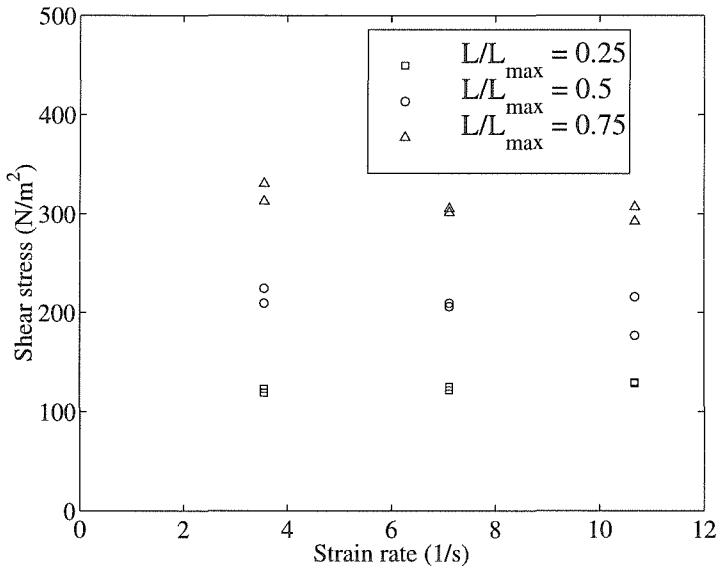


**Figure 6.5** Shear stress (averaged over time) as a function of strain rate for 4 mm glass beads in a 3 cm gap between cylinders ($h/d = 7.5$).

between particles, and is clearly either a quasi-static or transitional flow.

However, even a rapid flow does not show a rate-dependent stress component if it is unconfined. According to Savage [1984], in dry flows, the shear stress is always proportional to the normal stress confining the material. If this normal stress is constant as the strain rate is varied, then the shear stress is also constant. For example, Bridgwater's experiments in an annular shear cell showed only a slight strain rate dependence of the shear stress even at high strain rates [Bridgwater, 1972]. Savage attributes this behavior to the fact that the shear cell had a constant normal force applied to the top disk, so that the material could expand vertically, decreasing the solid fraction within the apparatus. This explanation also applies to the experiments by Tardos et al. [1998], in which no strain rate dependence was observed in the vertical Couette cylinder when no normal force was applied and the material could expand.

Both Bagnold's experiments of Couette flows of suspensions [Bagnold, 1954] and

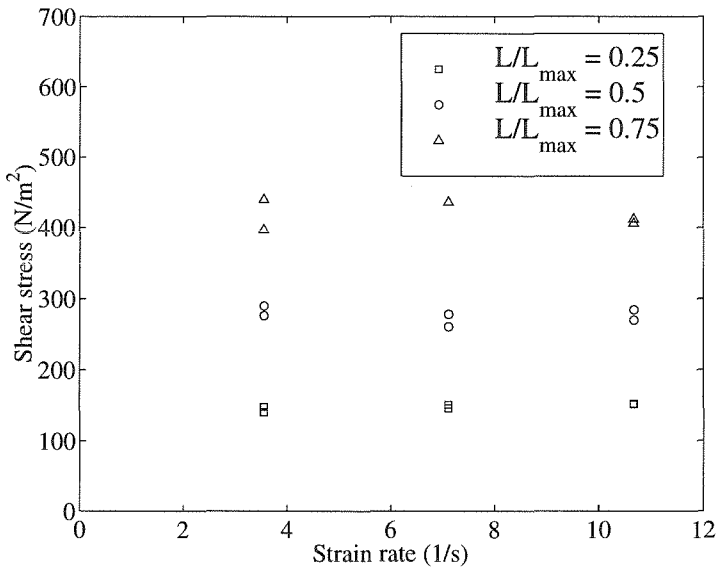


**Figure 6.6** Shear stress (averaged over time) as a function of strain rate for 6 mm glass beads in a 3 cm gap between cylinders ($h/d = 5$).

similar later experiments on suspensions by Savage and McKeown [1983] showed a quadratic dependence of shear stress on the rate of strain when the suspensions were in the rapid, or grain inertia, regime. Later experiments of dry granular materials in annular shear cells in which the solid fraction was maintained constant [Savage and Sayed, 1984; Hanes and Inman, 1985] showed a quadratic dependence of the shear stress on the rate of strain as well. In the current experiments of this study, the material in the Couette cell is unconfined from above and allowed to dilate, similarly to the material in the study by Tardos et al. [1998]. Thus, the dilation of the material, if it can take place, most likely accounts for the independence of the shear stress on the strain rate. In addition, the material is not in the rapid regime. From visual observation of the current experiment, it is determined that particles experience enduring contacts with other particles and walls, indicating that the shear flow is actually in the quasi-static regime described by Savage [1984]. Therefore, even

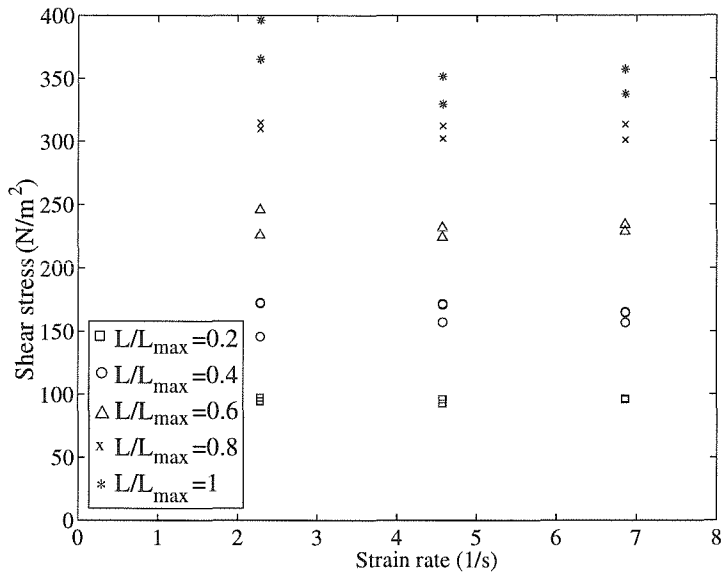


**Figure 6.7** Shear stress (averaged over time) as a function of strain rate for 3 mm glass beads in a 4 cm gap between cylinders ($h/d = 13.3$).

if the material is confined from above and the solid fraction kept constant, the stresses may not depend on the strain rate as they do for rapid flows.

### 6.1.3 Shear stress as a function of height

The level of fill ($L$) of each experimental run was calculated based on the weight of the material inside the apparatus. The actual height of the material was difficult to measure because it changed during the course of the experimental runs. In addition, the free surface of the beads was not level, but slightly sloping due to centrifugal force effects: the height was lower near the inner cylinder and higher near the outer cylinder. The difference in the height at the two cylinders did not exceed 2 centimeters at the highest rotation rate, so its effect on the pressure distribution within has been neglected. The height of the beads at the highest fill level used for each bead size was measured with a ruler at the end of a run, and the heights for the lower fill

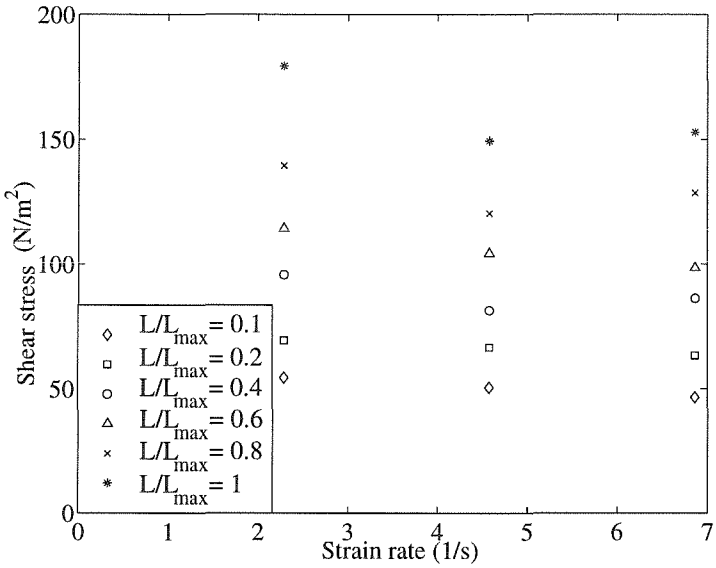


**Figure 6.8** Shear stress (averaged over time) as a function of strain rate for 4 mm glass beads in a 4 cm gap between cylinders ($h/d = 10$).

levels were calculated based on this total fill level and the known weight of the beads used in each. That is, the data for $L/L_{max} = 0.25$ was for 17.8 N (4 lbs) of beads, and the height was assumed to be one quarter of the height measured for 71.2 N (16 lbs) of beads. Therefore, the assumption was made that the packing did not change, possibly introducing some error into the measurements. The error in this measurement is estimated to be on the order of $\pm$ 0.5 cm.

The Janssen equation [Shamlou, 1988; Nedderman, 1992] predicts the normal stress in the $z$ direction (see figure 6.15) of a stationary granular material that has been poured into a container:

$$\tau_{zz}(z) = \frac{\rho g h}{\mu K}\left[1 - \exp\left(-\frac{2K\mu z}{h}\right)\right] \tag{6.2}$$

where

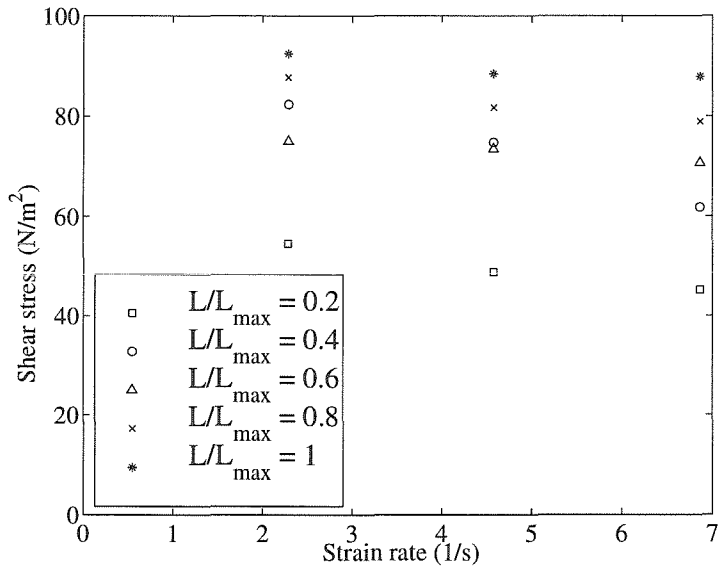


**Figure 6.9** Shear stress (averaged over time) as a function of strain rate for 6 mm glass beads in a 4 cm gap between cylinders ($h/d = 6.67$).

$\rho = \nu\rho_p$ is the bulk density of the material

$g$ is the acceleration due to gravity

$h$ is the distance between the two cylinders, or gap width, in the current experimental geometry

$\mu = \tau_{r\theta}/\tau_{rr}$ is the friction coefficient

$K = \tau_{rr}/\tau_{zz}$, also referred to as the Janssen constant [Shamlou, 1988]

$z$ is the vertical distance measured from the free surface (see figure 6.15).

As $z$ increases, the exponential term approaches zero and the stress becomes constant. In this analysis, the normal stress on the outer cylinder wall, $\tau_{rr}$, is proportional to $\tau_{zz}$ by the Janssen constant $K$. The shear stress, $\tau_{r\theta}$, is then proportional to $\tau_{rr}$ by the friction coefficient $\mu$, so that it too becomes constant at large depths of fill.

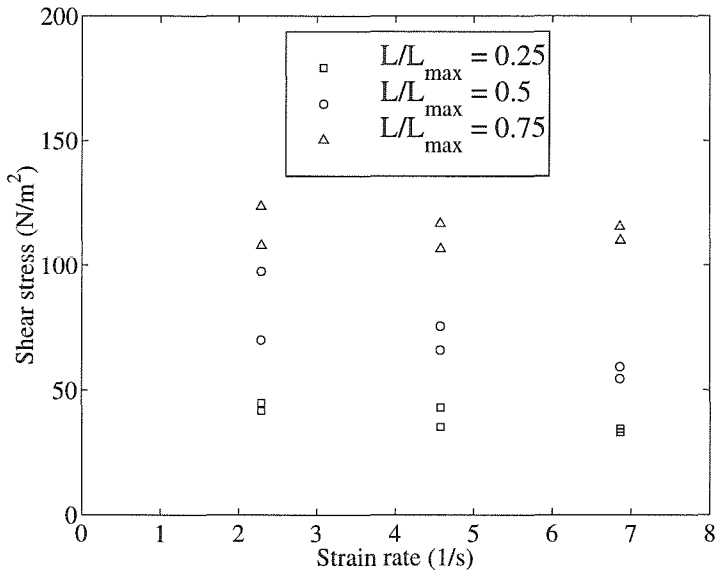


**Figure 6.10** Shear stress as a function of strain rate for 8 mm glass beads in a 4 cm gap between cylinders ($h/d = 5$).

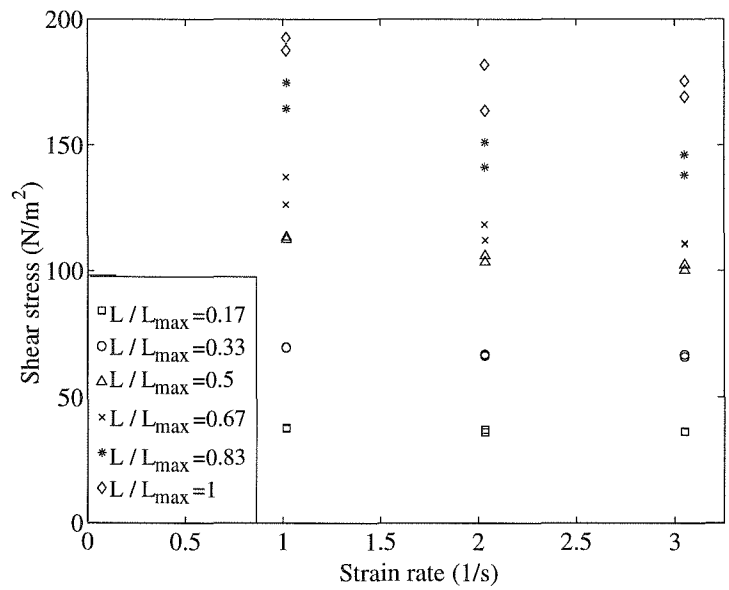


**Figure 6.11** Shear stress as a function of strain rate for 3 mm glass beads in a 6 cm gap between cylinders ($h/d = 20$).

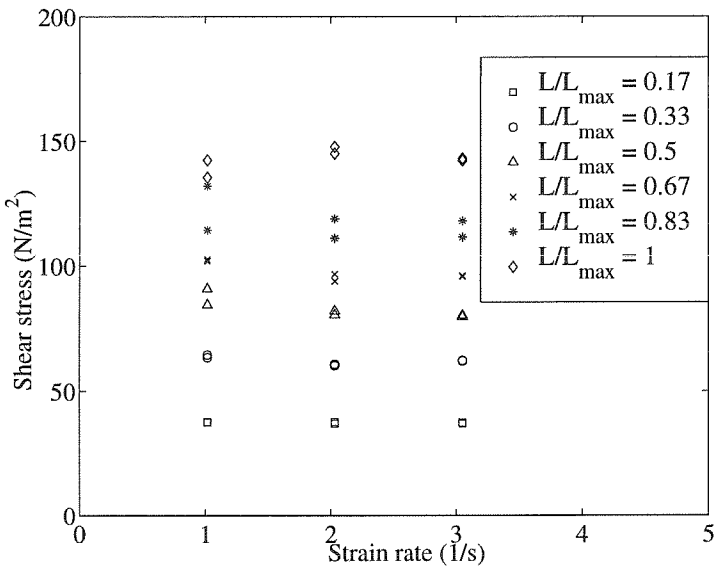


**Figure 6.12** Shear stress as a function of strain rate for 4 mm glass beads in a 6 cm gap between cylinders ($h/d = 15$).

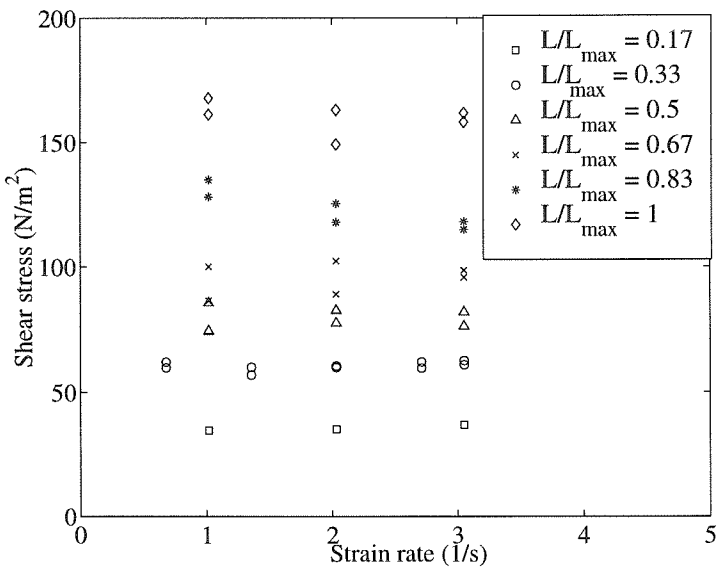


**Figure 6.13** Shear stress as a function of strain rate for 6 mm glass beads in a 6 cm gap between cylinders ($h/d = 10$).

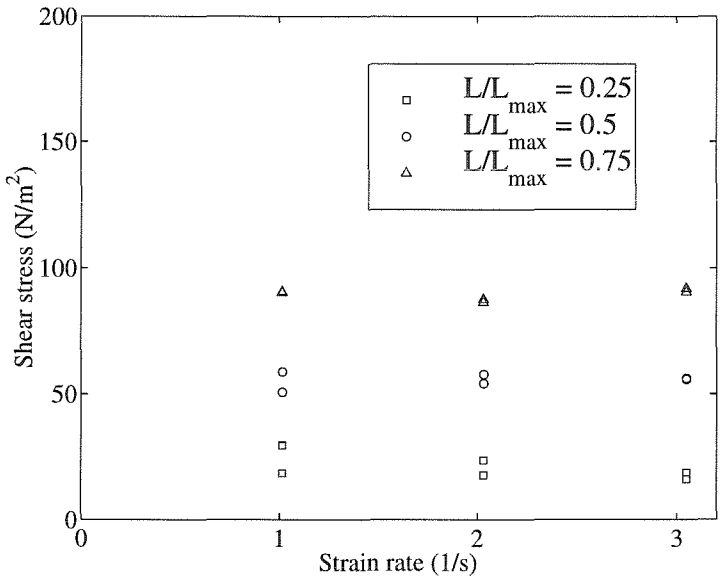


**Figure 6.14** Shear stress as a function of strain rate for 8 mm glass beads in a 6 cm gap between cylinders ($h/d = 7.5$).

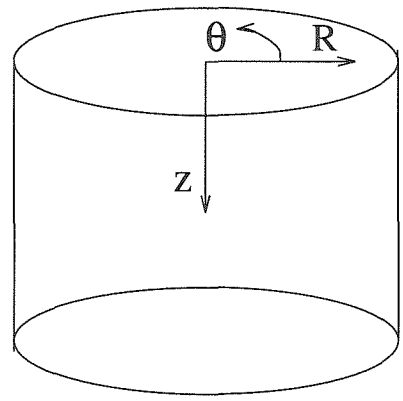


**Figure 6.15** Coordinate frame of cylinder.

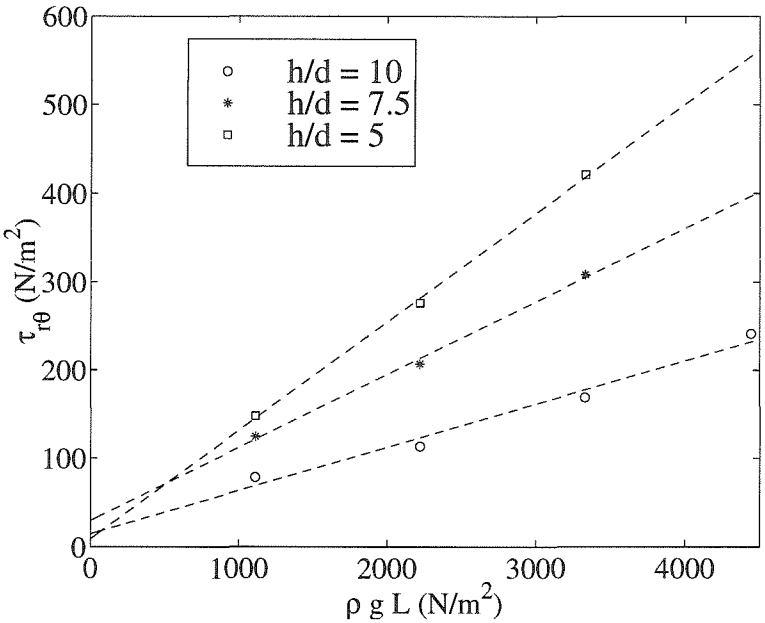


**Figure 6.16** Average shear stress as a function of the material fill level $L$ for the largest inner cylinder, with $h = 3$ cm.

In a stationary poured material the normal stress approaches a constant value because the shear stress on the walls, $\tau_{rz}$, supports some of the weight of the material. Arching in the granular material transfers force from the center to the side walls, leading to a non-hydrostatic stress distribution. In a sheared material, however, arches are broken and the sides do not support the load as they do in a stationary material. Therefore, in a flowing granular material, all of the weight of the material is supported by the material below it, not the side walls. The results of the current stress measurements confirm that the stresses show a hydrostatic dependence on the fill level.

In figures 6.16, 6.17, and 6.18, the average of the shear stress on the outer cylinder over all rotation rates has been plotted as a function of $\rho g L$ for each of the three inner cylinders, showing a linear dependence on the fill level. The dashed lines are linear fits to the data. Some of the linear fits do not pass through the origin, however. This

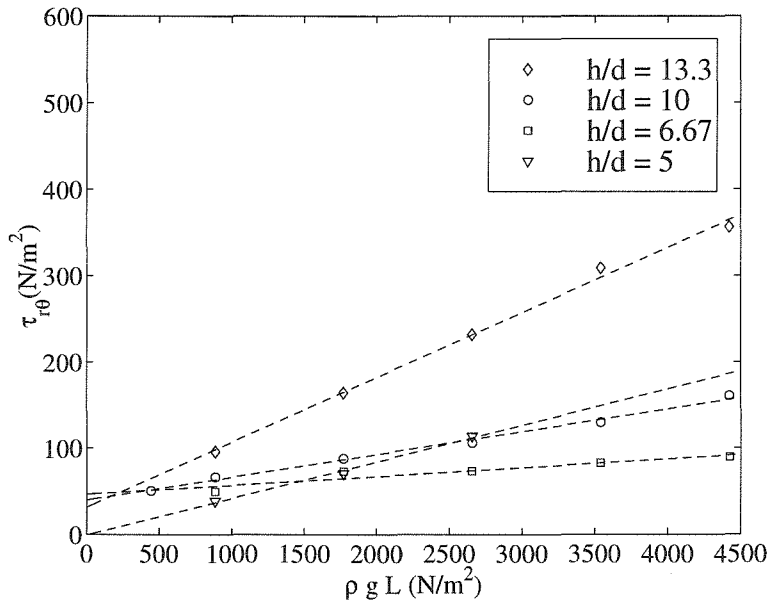


**Figure 6.17** Average shear stress as a function of the material fill level $L$ for the middle inner cylinder, with $h = 4$ cm.

is probably due to experimental error associated with the stress on the cylinder base, centrifugal forces, and error in fill height measurements, especially at lower heights. Tardos et al. [1998] measured the shear stress at two different fill levels and also found a hydrostatic dependence.

If centrifugal forces are ignored, that is, if $v_\theta^2/R << g$ (which is shown to be a good assumption in the following section), the normal stresses $\tau_{zz}$ and $\tau_{rr}$ have no dependence on the radial coordinate, $R$. If the material below supports all of the weight of the material above it, then the normal stresses $\tau_{zz}$ and $\tau_{rr}$ are hydrostatic:

$$\tau_{zz} = \rho g z \tag{6.3}$$

$$\tau_{rr} = K\tau_{zz} = K\rho g z, \tag{6.4}$$

where $K$ is a constant, $\rho = \nu\rho_p$ is the bulk density, and $g$ is the gravitational accel-

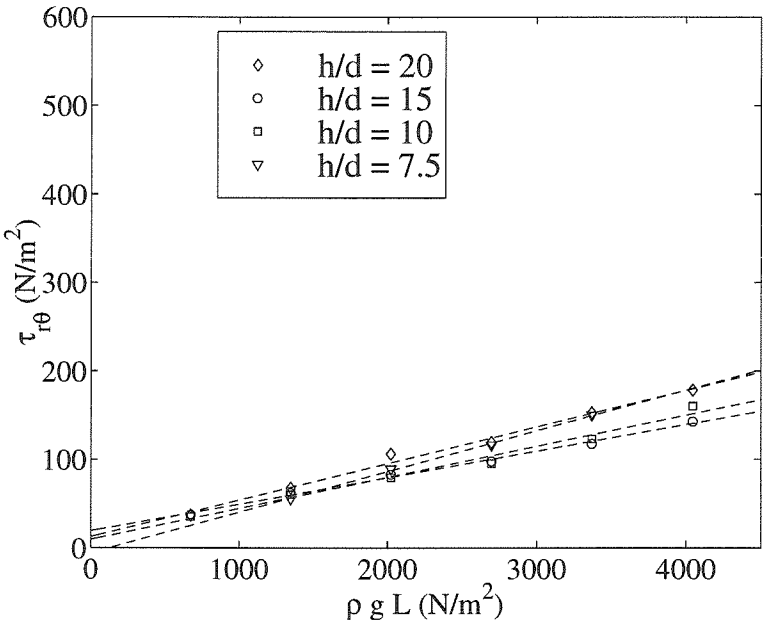


**Figure 6.18** Average shear stress as a function of the material fill level $L$ for the smallest inner cylinder, with $h = 6$ cm.

eration. The average normal stress at a fill height $L$ is:

$$\overline{\tau}_{rr}(L) = \frac{1}{L}\int_0^L K\rho g z dz = \frac{1}{2}K\rho g L. \tag{6.5}$$

The total torque exerted by the motor on the system, $M$, is not a function of $R$. The torque is related to the shear stress at any radius $R$ and fill height $L$ as follows:

$$M = 2\pi R^2 L \tau_{r\theta}, \tag{6.6}$$

where $2\pi RL$ is the area over which the stress acts. The condition that the torque is not a function of $R$ requires that the shear stress, $\tau_{r\theta}$, must be a function of $R$ so that $\tau_{r\theta} \sim 1/R^2$. Because the shear stress in a granular material is also proportional

to the normal stress, it must have the form

$$\tau_{r\theta} = \frac{1}{2}\mu K \rho g L \left(\frac{C^2}{R^2}\right), \tag{6.7}$$

where $\mu$ is the tangent of the wall friction angle and $C$ is an unknown constant with units of length. Thus, the ratio of the shear stress to the normal stress is necessarily a function of the radial position:

$$\frac{\tau_{r\theta}}{\tau_{rr}} = \frac{\mu C^2}{R^2}. \tag{6.8}$$

If it is determined that the stress ratio at the outer cylinder is equal to $\mu$, then the constant can be evaluated as $C = R_{outer}$. In this section, all the shear stresses plotted are evaluated at the outer cylinder. The slope calculated for the best-fit line to the graphs of $\tau_{r\theta}$ vs. $\rho g L$ is equal to $(1/2)\mu K(C^2/R^2_{outer})$.

In their similar study of shear stresses in a concentric cylinder Couette device, Tardos et al. [1998] made the assumption that the curvature of the apparatus is negligible and treated the shear stress as a constant, not a function of $R$. They evaluated it at the inner cylinder radius, and determined that the stress ratio is equal to $\sin\phi$, where $\phi$ is the internal angle of friction. The accuracy of this assumption lies in the ratio of the squares of the inner and outer radii of the device, $(R_{outer}/R_{inner})^2$. In the experiments by Tardos et al., this value is 1.2. In the current experiments, however, the value ranges from 1.4 to 2.5, so that the assumption of a planar flow would be far from accurate. In the analysis of Tardos et al., the two normal stresses are assumed to be equal as well, so that $K = 1$.

### 6.1.4 Shear stress as a function of the gap width to diameter ratio

The different data in figures 6.16–6.18 represent experiments with different values of the ratio of the gap width to the particle diameter, $h/d$. The slope of each line is different, illustrating that the stresses have a large dependence on this ratio. Savage and Sayed [1984] also found a dependence of stresses on $h/d$ at small $h$ in their experiments in an annular shear cell. At values of $h/d$ ranging from 6.85 to 7.84, and for a constant solid fraction of material, the stresses varied in some instances by almost one order of magnitude. This inconsistency in stress measurements was attributed to finite-particle-size effects. That is, even for very small changes in the gap width, $h$, the stress changed due to the different layering and packing of the material in the gap. If the gap spacing is such that the particles are allowed to form layers that can easily move relative to each other, the shear stresses are lower than if the particles lock together and there is a jamming effect. The dependence of the shear stresses measured in the current experiments on the ratio $h/d$ is also probably caused by differences in particle packing at different $h/d$.

Figure 6.19 is a plot of the slope of the linear fit to each set of data as a function of the ratio $h/d$. The different symbols correspond to the three different sizes of inner cylinder used. The error bars correspond to the maximum percentage error calculated based on the measurement errors in the length, the gap width, the weight of the material, and the error due to the resolution of the data acquisition system. This total error is estimated to be approximately 11%. It does not account for the error due to a variation in bead roughness and sandpaper roughness, which can be significant. This source of error is discussed further in this section.

Figure 6.19 illustrates that the shear stresses not only depend on the gap width to particle size ratio, $h/d$, but also on the radius of the inner cylinder used. Figure 6.19 shows a complex dependence of the stresses on $h/d$ at low values of this parameter. At the largest gap widths, the stresses become independent of $h/d$, showing similar values

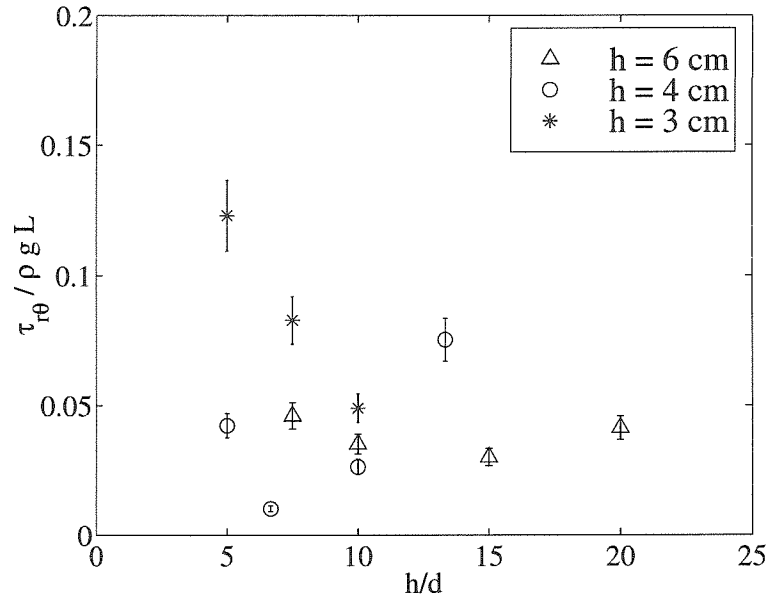


**Figure 6.19** Experimental results for $\tau_{r\theta}/\rho g L$ as a function of gap width to bead diameter ratio, $h/d$.

at $h/d = 15$ and 20. The results shown in the figure suggest that there is no clear functional relationship between the stress and $h/d$, but rather that the magnitude depends on the specific layering of the particles, as was suggested by Savage and Sayed [1984]. Several other factors can contribute to the lack of a clear functional relationship between $h/d$ and the shear stresses. The first is the ratio of the gap width to the inner cylinder radius, $h/R_{inner}$. In an ideal Couette flow, this parameter is as small as possible, but in the current experimental apparatus it ranges from 0.43 to 1.5 for the three inner cylinders. Shear stresses may have an additional dependence on this parameter as well as on $h/d$. Another factor that may result in different measurements for different bead diameters is the roughness of the sandpaper when compared with the size of the beads. Even at the same ratio of $h/d$, the sandpaper is not as effectively rough when shearing 8 mm beads as compared with 3 mm beads. During the course of the experiments, very large slip was observed between the inner

cylinder and the 8 mm beads when compared to smaller beads.

Two possible sources of error in the above results warrant discussion. The first is the possible contribution of centrifugal forces to the stress on the outer wall. At the low velocities used in the experiment, this contribution is negligible. The largest rotational velocity of the motor is 4.8 radians/second. The radius of the largest cylinder is 7 cm, so the largest velocity of the inner wall is 33.4 cm/s. From the vertical orientation velocity profiles shown in section 5.1.1, it is clear that the fastest particles in the system, adjacent to the moving surface, travel at less than half the wall velocity, or about 16 cm/s at most. Their centripetal acceleration is:

$$a_c = \frac{v_\theta^2}{R} = \frac{(16)^2 \mathrm{cm}^2/\mathrm{s}^2}{7\mathrm{cm}} = 37\mathrm{cm}/\mathrm{s}^2, \tag{6.9}$$

or about 4% of the gravitational acceleration. This is the largest contribution of centripetal effects possible in the current experimental apparatus. The contribution increases with the strain rate, but the figures of shear stress against strain rate (6.6–6.13) do not indicate any increase in the shear stress at the higher strain rates, further illustrating that the centripetal effects are not large enough to affect the results.

The second possible source of error is much more likely to have affected the current results. While the experiment is running, the roughness of the particles themselves increases, while the roughness of the sandpaper coating the solid surfaces probably decreases. It was not possible to perform all experiments with particles that were equally rough. Figure 6.20 shows the large discrepancy between shear stress results for used rough particles versus new smooth particles in the identical configuration. The data shown in figure 6.19 was gathered from experiments in which the particles were relatively smooth and new. Even in experiments using new particles, however, the particles became rougher during the course of the experimental runs; glass dust was usually observed at the end of an experiment, indicating that the particles were being ground. When the fill level was increased and new particles were added, the new ones were usually smoother than the particles below that had already undergone

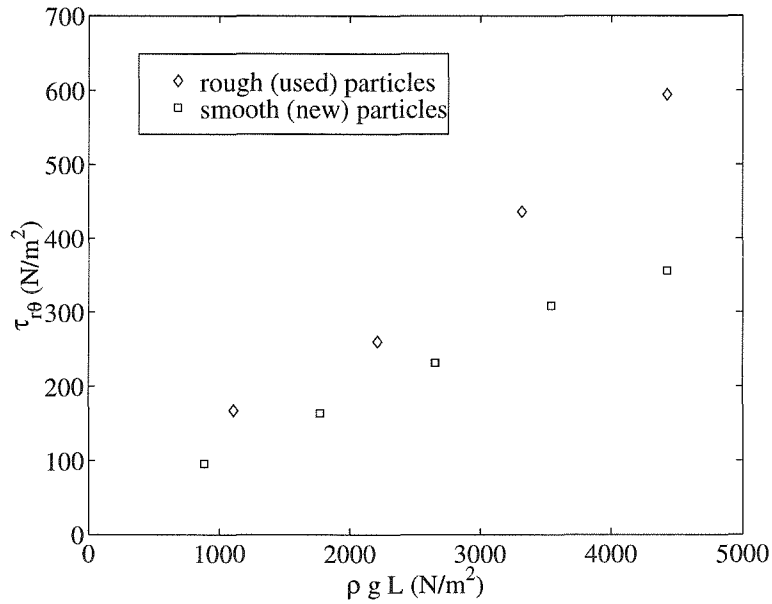


**Figure 6.20** Comparison of shear stress as a function of fill level for $h/d = 13.3$ for rough and smooth particles.

one set of experiments. Estimating the amount of error that the roughness of the particles and walls introduces to the results is difficult. The rough beads used in the results shown in figure 6.20 were more rough than any used in actual experiments; therefore, figure 6.20 represents the largest error possible in these experiments due to particle roughness effects. The slope $\tau_{r\theta}/\rho g L$ measured with smooth particles can be significantly lower than that measured with rough particles, as figure 6.20 illustrates. Rougher particles have an increased friction angle $\phi$, leading to a higher shear stress at a given normal stress level.

## 6.2 Horizontal orientation

Results for the horizontally oriented experiment are similar to those for the vertical orientation. There are similarly large time fluctuations of the measured stress, and

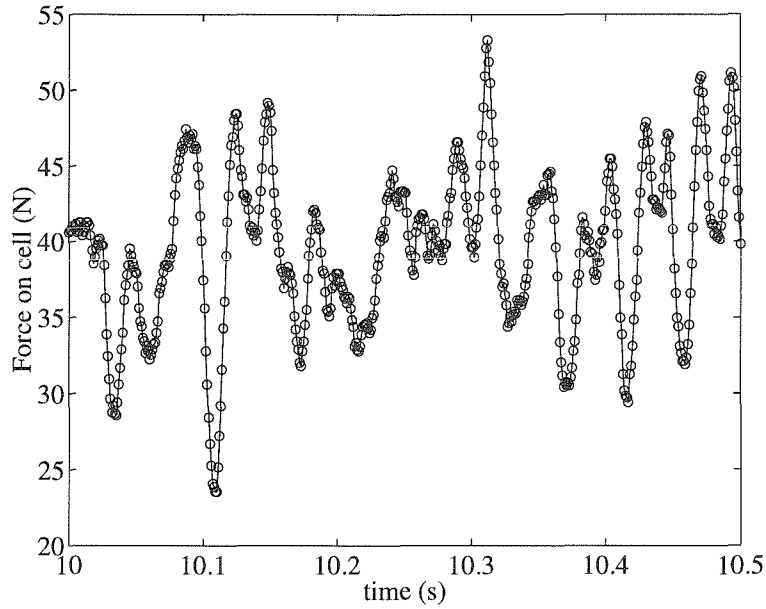


**Figure 6.21** Force on the load cell as a function of time. This data is for a horizontally oriented experimental run with the largest inner cylinder and 15 pounds of 6 mm glass beads.

there is no dependence of shear stress on strain rate. Again, this can be attributed to the free surface existing at the top of the flow, allowing for the dilation of the granular material. Experiments in the horizontal orientation were only conducted when the apparatus was almost full, so there was no study of the dependence of shear stress on fill level.

Figure 6.21 shows data for a horizontal experimental run with 67 N (15 lbs) of 6 mm glass beads and a gap width of 3 cm between cylinders. The sample rate is 1000 Hz, and the rotation rate is 43.7 RPM. All of the horizontal runs were performed off the platform, on the floor of the laboratory on top of carpeting, to reduce the noise in the signal.

Figure 6.22 represents the power density spectrum of the horizontal run. As in the vertical run of figure 6.3, there are distinct electrical noise frequencies at 120 Hz,

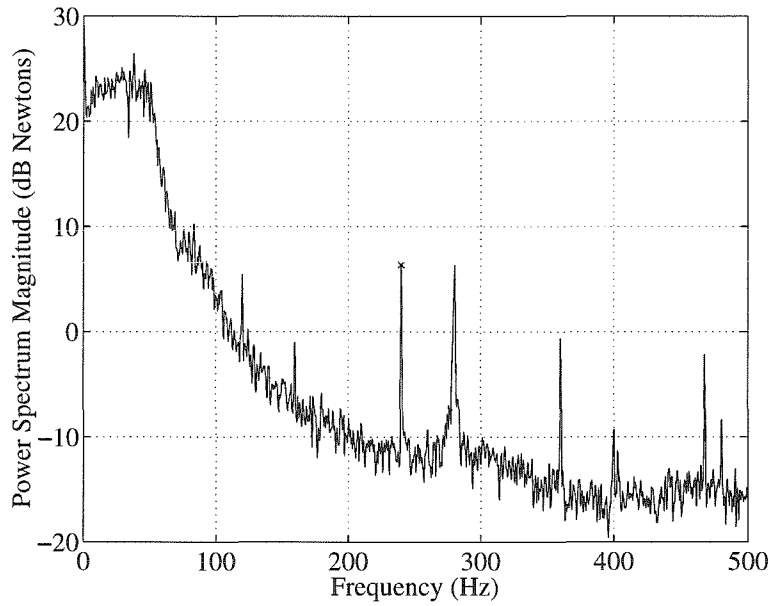


**Figure 6.22** Power density spectrum of the force on the load cell during a horizontal experiment without using the wooden platform.

240 Hz and 360 Hz. There is significantly less noise than the spectrum for the vertical run, which was performed on the wooden platform, especially in the lower frequencies. The higher sampling rate also reveals other peaks at higher frequencies; it is not clear to what cause they should be attributed. Figure 6.23 represents a typical result for a horizontally oriented experimental run. The shear stress has been measured for various rotation rates, first sweeping up to the fastest rate and then decreasing the rate back to zero. The example shown in figure 6.23 is an experiment run with the largest inner cylinder ($R_{inner}$=7 cm, $h$=3 cm), and 71 N (16 lbs) of 6 mm glass beads. As in the vertically-oriented experimental runs, the shear stress is not a function of the strain rate, for the same reasons. The flow is not rapid, and, in addition, the material is allowed to dilate due to the free surface at the top of the experiment.

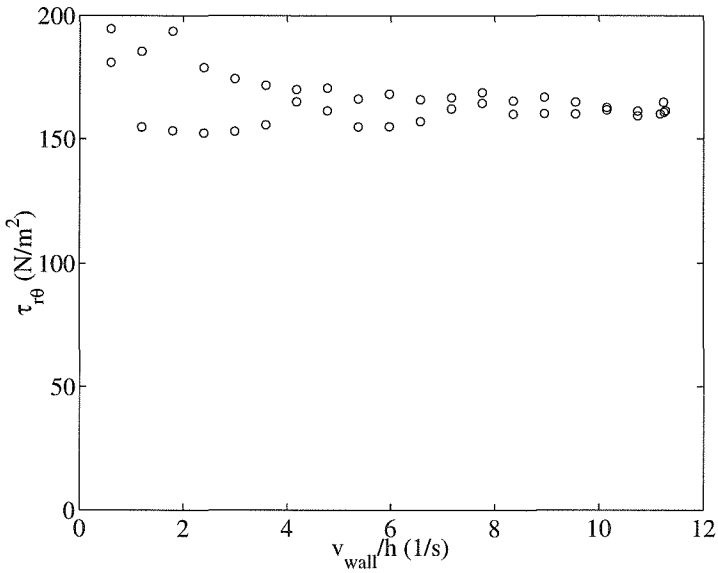


**Figure 6.23** Shear stress on outer cylinder as a function of the strain rate measured during an experiment in the horizontal orientation. The largest inner cylinder was used ($h/R_{inner} = 0.43$) with 4 mm beads so that $h/d = 7.5$.

# Chapter 7

# Conclusions

This chapter summarizes the conclusions of this research on Couette flows of granular materials. A summary of the current results is followed by a general summation of some of the unifying findings and a discussion of possible future investigations in this area.

## 7.1 Summary of results

### 7.1.1 Planar Couette flows

Simulations of particles between two infinite solid walls moving in opposite directions show that the flow exhibits two distinct regions with different properties. The region closest to the moving walls has a low particle concentration, high velocity gradient, and high granular temperature, corresponding to a large amount of fluctuation energy. The width of this region does not depend on the size of the gap between the walls, and is approximately three particle diameters wide in all flows. The width of the second region, in the center of the channel, does depend on the gap width, and the flow in this region has a high solid fraction, lower velocity gradient, and lower granular temperature. The walls in this planar Couette flow act as temperature sources, providing all the energy to the flow. As particles collide with the moving walls, the fluctuating

component of their velocity increases, resulting in a high granular temperature near the wall. As subsequent collisions occur between the high-energy particles nearest the walls and the slower particles away from the walls, fluctuation energy is conducted into the channel. Because collisions are inelastic, however, the fluctuation energy continually decreases as one moves away from the wall region, reaching a minimum in the center of the channel. Mixtures of two particle sizes have not previously been studied in a planar Couette geometry. In this research it was found that larger particles favor the central, low-temperature region. The arrangement of large particles in the gap also depends on the number of large particles: when there are many large particles, they become spaced out and often form distinct layers.

In flows of identical particles, average properties through the gap show a strong dependence on the overall solid fraction. The granular temperature, strain rate, and wall stresses increase with overall solid fraction, but also show a dependence on the ratio of the gap width to the particle diameter, $h/d$. This dependence of average properties on the width of the gap has not been studied previously in this type of flow, and is found to be significant. A sharp change in properties occurs at a threshold solid fraction that depends on $h/d$. This threshold appears to occur when the solid fraction at the wall reaches approximately 0.25. The average (overall) solid fraction at which the wall solid fraction reaches the critical value depends on $h/d$, because the particles are densely packed in the center of the flow; the wider the center region is, the higher the overall solid fraction must be to reach the critical wall solid fraction.

In mixtures, stresses are close to the level for the corresponding flow of same-size particles when the mixture size ratio is low and the number of large particles is small. Stresses increase with both size ratio (due to the mass dependence of the stress) and with decreasing solid fraction ratio of small to large particles.

Granular shear flows are highly dissipative, a property that often leads to unwanted heating during processing. The current research represents the first study of energy dissipation in a granular flow as a function of various flow parameters. Com-

puter simulations were used to measure the amount of energy dissipated in a granular flow in both same-size flows and mixtures. Results show that the highest dissipation rates occur in the regions of high granular temperature nearest the walls, due to the large collision rate in those areas. In same-size particle flows, the dissipation rate and corresponding thermodynamic temperature increases with overall solid fraction, again, due to the increase in the collision rate. In mixtures, heat dissipation increases with the solid fraction of large particles as well as with the diameter ratio.

The current simulation work in planar Couette flows has been compared to past theoretical results derived from kinetic theory, with generally good qualitative agreement. Such comparisons provide a basis for validation of the theory under various conditions as well as a demonstration of the weaknesses of some kinetic theory assumptions. Computer simulations are a valuable tool that can aid the development of theoretical constitutive models for granular flow.

### 7.1.2 Cylindrical Couette flows

A concentric cylinder Couette apparatus has been used to investigate shear stresses experimentally. In a rapid granular shear flow with a constant solid fraction, the shear stress is expected to increase quadratically with the rate of strain. The current experiments show no dependence of the shear stress on the strain rate at all, however. Both vertically and horizontally oriented experiments show that the shear stress is independent of strain rate because the existence of an unconfined free surface allows the material to dilate under shear. In addition, the flow exhibits enduring, frictional contacts, indicating that it is not in the rapid granular flow regime, but rather in either a quasi-static or transitional regime.

Vertically-oriented experimental stress measurements yielded interesting and novel results concerning the dependence of shear stress on the material height and on the gap width. First, the stress in the material varies linearly with height. In this shear flow, the side walls are unable to support any portion of the weight of the granular

material, as they would in a stationary material. Thus, all of the weight of the particles is supported by the particles beneath them, resulting in a linear dependence of the stress on the height of material.

Second, the shear stress also varies with the ratio of gap width to particle diameter ($h/d$), a dependence that had not been previously investigated in this geometry. This dependence is not a clear functional relationship due to the many other variables affecting the results, such as the ratio of sandpaper roughnesses to the bead diameter and the ratio of the gap width to the inner cylinder diameter ($h/R_{inner}$). Other errors could also have been introduced, due to differences in the bead roughness and the sandpaper roughness between experimental runs. The roughness of the beads and the sandpaper can have a large impact of the friction coefficient, and therefore on the ratio of shear to normal stresses.

With the experimental apparatus horizontally oriented, both flows of one particle size and of mixtures were investigated. Velocity profiles from computer simulations and experiments indicate large velocity gradients near the rotating inner cylinder, with velocities near zero at the outer cylinder wall. Significant slip occurs at the inner wall for all cases; slip velocities range from 50 to 70% of the wall velocity. Fluctuation velocities are highest near the inner cylinder, where the flow is faster and more agitated. Fluctuations in the flow direction are larger than in the transverse direction. This anisotropy in fluctuation velocities has also been observed by previous researchers in granular flow experiments [Elliot *et al.*, 1998; Natarajan *et al.*, 1995]. Computer simulations show good agreement with experimental velocity profiles, but fluctuation velocities measured in the computer simulations are significantly higher than those of experiments. Two different normal contact models were used in the simulations, with no difference in the results.

The segregation pattern of a mixture of particles of two different sizes was also investigated in the horizontal Couette apparatus. Segregation begins at the free surface with the larger particles rising to the top. These large particles are then

pushed counter-clockwise with the remainder of the flow and remain concentrated in the upper left region. The resulting angular concentration profile is thus asymmetric, with more large particles on the left than on the right. This angular segregation pattern occurs very similarly in computer simulations. In experiments, large particles remain near the outer cylinder as they flow, and radial segregation occurs as well. The number density of small particles is high near the inner cylinder, while large particles remain near the outer cylinder. The present computer simulations do not capture this effect accurately, however.

## 7.2 General issues

The research presented in this thesis is the first to investigate several aspects of granular Couette flows. The effect of the ratio of the gap width to the particle diameter, $h/d$, has not previously been studied in either the planar or the cylindrical flow geometry. In addition, although segregation is a common area of research, binary mixtures have not been investigated before in planar Couette flows. Two previous studies have investigated vertically-oriented cylindrical Couette flows [Khosropour *et al.*, 1997; Tardos *et al.*, 1998], but the horizontal orientation, which shows a geometric resemblance to industrially used screw mixers, has not been previously investigated at all. Lastly, although energy dissipation in granular material often leads to unwanted heating in industrial processes, this is the first study to quantify the heat produced during a typical flow.

This work on Couette flows of particles has revealed two related and important aspects of granular flow that both influence the dynamics of such flow significantly. First, flow geometry plays a dominant role in all the flows studied. In planar Couette flows, the width of the gap between the shearing walls has a large influence on the stresses and energy dissipation of the flows. In mixtures, geometry dictates the position of the larger particles. When there are few large particles, they concentrate in

the center region, but when there are many they become more evenly spaced out and form distinct layers. The cylindrical Couette flows studied are also heavily influenced by geometry. Shear stresses vary greatly depending on the gap width between the concentric cylinders. Segregation in the horizontal experiment, although induced by a percolation mechanism near the free surface, is perpetuated in the rest of the flow through mechanisms dependent on geometry.

Second, the boundary conditions, which are a specific aspect of the geometry, have a large impact on flow as well. In planar flows, the solid fraction at the boundary dictates the amount of slip velocity, shear stress, strain rate, granular temperature, and energy dissipation. In experiments on cylindrical flows, the difficulty in controlling the friction between the particles and the boundaries results in very different shear stress measurements under similar conditions.

Because both boundary conditions and geometry are found to have significant effects in granular flows, experimental results are often limited to one particular application or geometry. The difficulty in controlling particle and boundary properties during the course of an experiment also leads to inconsistent results. These problems have led to an increased dependence on computer simulations for the investigation of particulate flows. This research has used both computer simulations and experiments to study cylindrical Couette flows and to make valuable quantitative comparisons between the two.

The current results have shed light on certain features of granular Couette flows and have revealed other issues that merit further investigation. Experimental results show that the shear stress in a cylindrical Couette flow depends on the gap width, but the exact relationship between the two is as yet unknown. In addition, computer simulations agree quantitatively with experiments in some instances, but not in others. Quantitative comparisons between simulations and experiments in the future may shed light on whether computer simulations can indeed be used to predict realistic granular flows accurately.

# Bibliography

P. Arteaga and U. Tüzün. Flow of binary mixtures of equal-density granules in hoppers – size segregation, flowing density and discharge rates. *Chem. Eng. Sci.*, 45(1):205–223, 1990.

R. A. Bagnold. Experiments on a gravity-free dispersion of large solid spheres in a Newtonian fluid under shear. *Proc. R. Soc. London, Ser. A*, 225:49–63, 1954.

J. Bridgwater. Stress-velocity relationships for particulate solids. *Am. Soc. Eng. Pap.*, 72-MH-21, 1972.

H. Buggisch and G. Löffelmann. Theoretical and experimental investigations into local granulate mixing mechanisms. *Chem. Eng. Process.*, 26:193–200, 1989.

C. S. Campbell. *Shear Flows of Granular Materials.* PhD thesis, California Institute of Technology, Pasadena, California, 1982.

C. S. Campbell. The effect of microstructure development on the collisional stress tensor in a granular flow. *Acta Mech.*, 63:61–72, 1986.

C. S. Campbell. The stress tensor for simple shear flows of a granular material. *J. Fluid Mech.*, 203:449–473, 1989.

C. S. Campbell. Rapid granular flows. *Annu. Rev. Fluid Mech.*, 22:57–92, 1990.

C. S. Campbell. Boundary interactions for two-dimensional granular flows. Part 1.

Flat boundaries, asymmetric stresses and couple stresses. *J. Fluid Mech.*, 247:111–136, 1993.

C. S. Campbell and C. E. Brennen. Computer simulation of granular shear flows. *J. Fluid Mech.*, 151:167–188, 1985.

P. W. Cleary, G. Metcalfe, and K. Liffman. How well do discrete element granular flow models capture the essentials of the mixing processes? *App. Math. Modeling*, 22:995–1008, 1998.

K. Craig, R. H. Buckholz, and G. Domoto. An experimental study of the rapid flow of dry cohesionless metal powders. *J. Appl. Mech.*, 53:935–942, 1986.

P. A. Cundall and O. D. L. Strack. A discrete numerical model for granular assemblies. *Géotechnique*, 29:47–65, 1979.

T. G. Drake. Granular flow: physical experiments and their implications for microstructural theories. *J. Fluid Mech.*, 225:121–152, 1991.

T. G. Drake and O. R. Walton. Comparison of experimental and simulated grain flows. *J. Appl. Mech.*, 62:131–135, 1995.

E. A. Eklund, W. H. Wayman, L. J. Brillson, and D. A. Hays. Toner adhesion physics: Measurements of toner/substrate contact area. In *IS&T's Tenth International Congress on Advances in Non-Impact Printing Technologies*, 1994.

K. E. Elliot, G. Ahmadi, and W. Kvasnak. Couette flows of a granular monolayer – an experimental study. *J. Non-Newtonian Fluid Mech.*, 74:89–111, 1998.

M. Farrell, C. K. K. Lun, and S. B. Savage. A simple kinetic theory for granular flow of binary mixtures of smooth, inelastic, spherical particles. *Acta Mech.*, 63:45–60, 1986.

J. A. C. Gallas, H. J. Herrmann, T. Poschel, and S. Sokolowski. Molecular dynamics simulation of size segregation in three dimensions. *J. Stat. Phys.*, 82(1/2):443–450, 1996.

N. I. Gelperin and V. G. Einstein. Heat transfer in fluidized beds. In J. F. Davidson and D. Harrison, editors, *Fluidization*, pages 471–568. Academic Press, London and New York, 1971.

D. M. Hanes and D. L. Inman. Observations of rapidly flowing granular-fluid materials. *J. Fluid Mech.*, 150:357–380, 1985.

D. M. Hanes, J. T. Jenkins, and M. W. Richman. The thickness of steady plane shear flows of circular disks driven by identical boundaries. *J. Appl. Mech.*, 55:969–974, 1988.

D. Henderson. A simple equation of state for hard discs. *Molec. Phys.*, 30(3):971–972, 1975.

D. Hirshfeld and D. C. Rapaport. Molecular dynamics studies of grain segregation in sheared flow. *Phys. Rev. E*, 56(2):2012–2018, 1997.

S. S. Hsiau and M. L. Hunt. Kinetic theory analysis of flow-induced particle diffusion and thermal conduction in granular material flows. *ASME J. Heat Transfer*, 115:541–548, 1993.

S. S. Hsiau and M. L. Hunt. Granular thermal diffusion in flows of binary-sized mixtures. *Acta Mech.*, 114:121–137, 1996.

M. L. Hunt. Comparison of convective heat transfer in packed beds and granular flows. In C. L. Tien, editor, *Annual Review of Heat Transfer*, volume III, pages 163–193. Hemisphere Publishing Corporation, 1990.

M. L. Hunt. Discrete element simulations for granular material flows: effective thermal conductivity and self-diffusivity. *Int. J. Heat Mass Transfer*, 40:3059–3068, 1997.

J. T. Jenkins. Boundary conditions for rapid granular flow: Flat, frictional walls. *J. Appl. Mech.*, 59:120–127, 1992.

J. T. Jenkins and M. Y. Louge. On the flux of fluctuation energy in a collisional grain flow at a flat, frictional wall. *Phys. Fluids*, 9(10):2835–2840, 1997.

J. T. Jenkins and F. Mancini. Balance laws and constitutive relations for plane flows of a dense, binary mixture of smooth, nearly elastic, circular disks. *J. Appl. Mech.*, 54:27–34, 1987.

J. T. Jenkins and F. Mancini. Kinetic theory for binary mixtures of smooth, nearly elastic spheres. *Phys. Fluids*, 12:2050–2057, 1989.

J. T. Jenkins and R. Richman. Kinetic theory for plane flows of a dense gas of identical, rough, inelastic, circular disks. *Phys. Fluids*, 28:3485–3494, 1985.

J. T. Jenkins and R. Richman. Boundary conditions for plane flows of smooth nearly elastic, circular disks. *J. Fluid Mech.*, 171:53–69, 1986.

J. T. Jenkins and S. B. Savage. A theory for the rapid flow of identical, smooth, nearly elastic, spherical particles. *J. Fluid Mech.*, 130:187–202, 1983.

R. Khosropour, J. Zirinsky, H. K. Pak, and R. P. Behringer. Convection and size segregation in a Couette flow of granular material. *Phys. Rev. E*, 56(4):4467–4473, 1997.

S. R. Kim. A simulational study of granular boundary flows in two dimension. *Comp. Mat. Sci.*, 4:125–132, 1995.

C. K. K. Lun. Kinetic theory for granular flow of dense, slightly inelastic, slightly rough spheres. *J. Fluid Mech.*, 233:539–559, 1991.

C. K. K. Lun. Granular dynamics of inelastic spheres in Couette flow. *Phys. Fluids*, 8(11):2868–2883, 1996.

C. K. K. Lun and A. A. Bent. Numerical simulation of inelastic frictional spheres in simple shear flow. *J. Fluid Mech.*, 258:335–353, 1994.

C. K. K. Lun and S. B. Savage. A simple kinetic theory for granular flow of rough, inelastic, spherical particles. *J. Appl. Mech.*, 54:47–53, 1987.

C. K. K. Lun, S. B. Savage, D. J. Jeffrey, and N. Chepurniy. Kinetic theories for granular flow: inelastic particles in Couette flow and slightly inelastic particles in a general flowfield. *J. Fluid Mech.*, 140:223–256, 1984.

B. Miller, C. O'Hern, and R. P. Behringer. Stress fluctuations for continuously sheared granular materials. *Phys. Rev. Lett.*, 77(15):3110–3113, 1996.

M. Nakagawa. Axial segregation of granular flows in a horizontal rotating cylinder. *Chem. Eng. Sci.*, 49(15):2540–2544, 1994.

V. V. R. Natarajan and M. L. Hunt. Kinetic theory analysis of heat transfer in granular flows. *Int. J. Heat Mass Transfer*, 41:1929–1944, 1998.

V. V. R. Natarajan, M. L. Hunt, and E. D. Taylor. Local measurements of velocity fluctuations and diffusion coefficients for a granular material flow. *J. Fluid Mech.*, 304:1–25, 1995.

R. M. Nedderman. *Statics and Kinematics of Granular Materials.* Cambridge University Press, 1992.

S. Ogawa. Multi-temperature theory of granular materials. In *U.S.-Japan Seminar on Continuum-Mechanical and Statistical Approaches in the Mechanics of Granular Materials*, pages 208–217, 1978.

O. Reynolds. On the dilatancy of media composed of rigid particles in contact. *Phil. Mag.*, 20, 1885.

M. W. Richman. Boundary conditions based upon a modified Maxwellian velocity distribution for flows of identical, smooth, nearly elastic spheres. *Acta Mech.*, 75:227–240, 1988.

M. W. Richman and C. S. Chou. Boundary effects on granular shear flows of smooth disks. *J. Appl. Math. and Phys.*, 39:885–901, 1988.

A. D. Rosato and H. Kim. Particle dynamics calculations of wall stresses and slip velocities for Couette flow of smooth inelastic spheres. *Continuum Mech. Thermodyn.*, 6:1–20, 1994.

S. B. Savage. The mechanics of rapid granular flows. *Advances in Applied Mechanics*, 24:289–366, 1984.

S. B. Savage and R. Dai. Studies of granular shear flows: Wall slip velocities, 'layering' and self-diffusion. *Mech. Mat.*, 16:225–238, 1993.

S. B. Savage and C. K. K. Lun. Particle size segregation in inclined chute flow of dry cohesionless granular solids. *J. Fluid Mech.*, 189:311–335, 1988.

S. B. Savage and S. McKeown. Shear stresses developed during rapid shear of concentrated suspensions of large spherical particles between concentric cylinders. *J. Fluid Mech.*, 127:453–472, 1983.

S. B. Savage and M. Sayed. Stresses developed by dry cohesionless granular materials sheared in an annular shear cell. *J. Fluid Mech.*, 142:391–430, 1984.

P. A. Shamlou. *Handling of Bulk Solids.* Butterworth & Co., 1988.

G. I. Tardos, M. I. Khan, and D. G. Schaeffer. Forces on a slowly rotating, rough cylinder in a Couette device containing a dry, frictional powder. *Phys. Fluids*, 10(2):335–341, 1998.

C. T. Veje, D. W. Howell, and R. P. Behringer. Kinematics of a two-dimensional granular Couette experiment at the transition to shearing. *Phys. Rev. E*, 59(1):739–745, 1999.

O. R. Walton and R. L. Braun. Stress calculations for assemblies of inelastic spheres in uniform shear. *Acta Mech.*, 63:73–86, 1986.

O. R. Walton and R. L. Braun. Viscosity, granular-temperature, and stress calculations for shearing assemblies of inelastic, frictional disks. *J. Rheol.*, 30:949–980, 1986.

D. G. Wang, S. S. Sadhal, and C. S. Campbell. Particle rotation as a heat transfer mechanism. *Int. J. Heat Mass Transfer*, 32:1413–1423, 1989.

C. R. Wassgren. *Vibration of Granular Materials.* PhD thesis, California Institute of Technology, Pasadena, California, 1997.